Università degli Studi di Cagliari

DOTTORATO DI RICERCA

Fisica della Materia

Ciclo XXIII°

Research on non-conventional crystal oxides for photonic applications

Presentata da: Alberto Casu

Coordinatore Dottorato Prof. Giovanni Bongiovanni

Relatori Prof. Alberto Anedda, Dr. Pier Carlo Ricci

Esame finale anno accademico 2009 - 2010

INDEX

General introduction

1 Overview

Crystal oxide materials constitute a very wide family of compounds that find applications in the most diverse areas according to their specific characteristics, i.e. the crystal structure and the chemical components. In the last decades many important results were achieved in photonics, starting from early achievements such as solid state laser development, whose interest was initially limited to specialistic audiences, and moving up to wide impact ones such as the current novelties in the fields of telecommunications or meteorology [1-5].

Two particular applications of crystal oxides can be cited as examples of this shift, namely active medium for solid state lasers and scintillators. Despite their short history, these fields of research acted as a starting ground for the development of materials with an ever-growing range of applications.
In the 1960s crystal oxides were proposed and used as active media for different solid state lasers (Ruby laser[6], Nd:YAG laser[7]). From then on the race for active materials with new structures and/or dopants has never stopped, leading to lasers with an ever increasing number of operation energies that met many scientific and industrial requirements.

In parallel, the discovery and development of materials for scintillation goes back to the beginning of the 20th century but progresses in this field of research can be already divided in three phases when candidate materials are considered. While the first two phases spanned the most part of the century following the technological evolution in detection techniques of scintillation processes (from visible/direct to photomultiplier-measured), the third one established an important variation in the

research driving points. This latter phase took place in the last three decades and is characterized by two factors: the introduction of new materials for scintillation and a rethinking of the fields of application, be it as the introduction of new fields of research (high energy physics) or as the improvement of already known fields (medical imaging).

Indeed, a “backwards” research work devoted to offer a theoretical and structural basis is a mandatory task in order to consciously direct industrial efforts towards new efficient applications, given the always increasing number of materials that are being presented and swapped for different purposes, along with the general lack of complete fundamental studies covering their structural characteristics.

On the other hand, the imbalance between applicative and fundamental studies on RE (Rare Earth) oxides determines different approaches depending on the points of interest of each compound. In fact, two main points should be considered in order to comprehend the general interest of these materials and to better grasp the wide range of approaches involved in their study : 1) the definition of RE crystal oxides denotes a class of materials with different crystal structures and with similar physical characteristics given by rare earths, which leads to common fields of application. 2) due to their limited availability or novelty, the industrial performances were empirically developed rather than obtained starting from a theoretical basis. However, the importance of a strong structural background was remarked as an actual requirement for further developments of these materials in the lights of a recently proposed procedure called “compositional tuning” i.e. the possibility of tailoring the material properties for different applications according to their structural characteristics, which was first suggested for Nd-doped yttrium aluminum garnet.

Nowadays different crystal oxides in the garnet, perovskite and oxyorthosilicate families are being proposed, tailoring their physical and chemical characteristics according to each required application, the most significant example being the yttrium aluminum garnet, whose characteristics can be tailored

for diverse applications, such as active laser medium (when doped with neodymium, erbium or chromium[7-9]), as scintillator (when doped with cerium[10]), as optical data storage medium or as sensitizer (when doped with thulium or iron[11, 12]).

Some of the most promising results of this branch of research are given by rare earth mixed crystal perovskites and oxyorthosilicates, Ce-doped $Lu_xY_{1-x}AlO_3$ and $Lu_{2x}Y_{2(1-x)}SiO_5$, whose characteristics of fast scintillation, high light yield and high stopping power hint to various applications. However, generally speaking, some major problems still need to be solved such as the possible mismatch between theoretical and actual tunability to specific requests, which is not easily controllable and, sometimes, attainable.

A good example is given by tailoring the decay time of a given compound for scintillation devices, which is strongly affected by competitive decay processes in respect to luminescence, that decrease the scintillator performances of both the light yield and the decay time and, consequently, should be avoided.

Different parameters play a key role in the device performance and are worth the investigation, starting from a detailed analysis of the matrix crystal structure, which often undergoes modifications because of different growth conditions, to the role of luminescent ions as a function of their concentration and crystallographic site. Moreover, the presence of intrinsic point defects (vacancies of anions and/or cations and interstitial atoms), extrinsic (unwanted impurities) or extended defects (dislocations) might also play a crucial role in the performance of the materials if energy levels acting as trapping or recombination centers are introduced within the matrix energy gap. Optimization processes, aimed at increasing the material efficiency, are therefore needed to decrease or deactivate these centers. This goal can be accomplished after the growth by purification processes, such as thermal annealing treatments, by optimizing the growth processes and the stoichiometric and thermodynamic parameters or, in the case of intrinsic defects, with an intentional co-doping aimed at eliminating (or at least

reducing) undesired trapping and energy transfer processes. Among these possibilities, the first is the one less relying on a detailed theoretical knowledge of the specific materials, but still its effectiveness is dependent to a certain degree of structural and theoretical informations. Thus, a full comprehension of the specific structural variations caused by different factors such as doping or growth conditions becomes a strict and practical requirement, just like the capability of obtaining the needed insight with different experimental techniques. This exigency is far more true for rare earth-doped mixed crystals such as RE perovskites and oxyorthosilicates, whose diffusion is limited, despite their interesting characteristics, by difficult growing processes and control of the materials.

The main goal of this work is to move forward in the direction of a more organic insight on this class of oxides, starting from structural characterization, moving on to the role and the analysis of dopants and ending with a more applicative analysis of grown compounds, devoted to find and exploit their structural characteristics for new applications.

2 **Experimental techniques**

Many spectroscopic techniques can be successfully used to gather useful informations when looking for the structural characterization of a material but none of them alone can offer the complete outlook that is one of the main goals of this work. Thus the experimental techniques should have two main characteristics: the capability of giving complementary and cross-checkable results and the non-destructive nature of the measurement process. While the first requirement is easily understandable, the second one must be better clarified: destruction of the samples apart, the requirement implies the necessity that the measurements do not undesirably modify the sample characteristics, whether structural (rearranging) or compositional (trapping of “light” chemical elements or creation of defects). Bearing these requests in mind, different techniques were used according to their specific capabilities.

2.1 Raman spectroscopy

The analysis of Raman spectra can be performed, at first, as a fingerprinting method to assess the formation of a particular material with a specific crystal structure: the analytical procedure, however, can study specific vibrational and rotational modes in depth in order to identify unknown materials. Obviously these two approaches imply a quite different level of theoretical background and extensiveness of analysis. In the first case the key factor for a successful result lays only in the collection of experimental data, while in the latter case further theoretical and analytical factors are needed.

Thinking to Raman effect as a change in the ellipsoid of polarization or, analogously, in the polarizability tensor α, the optical Raman activity is generally anisotropic and, therefore, its collection is dependent on the experimental setup. A different intensity distribution between two Raman-active vibrations taken with different polarization geometries of excitation and collection points out the anisotropy of polarizability α. Experimentally, measurements of the intensities of two polarized spectra, one parallel and one perpendicular to the polarization of the incident radiation, permits to define the depolarization ratio,

$$\rho = \frac{I_{perpendicular}}{I_{parallel}}$$

which gives direct information on the shape of the polarization ellipsoid. A symmetric ellipsoid will determine a unitary value of depolarization ratio (non-polarized spectra), being unaffected from the geometrical setup of the light excitation and collection geometry, while an asymmetric ellipsoid will result in different intensities depending on the geometry of collection (polarized spectra). As a consequence, the informations obtained by the collection of polarized Raman spectra offer an precise analytical tool of structural identification and analysis of new compounds.

2.2 Extended X-Ray Absorption Fine Structure spectroscopy (EXAFS)

Extended X-Ray Absorption Fine Structure spectroscopy allows a "local" structural analysis of a given sample by exciting core electrons of a chemical element of choice and measuring the effects of electronic interactions with atoms in the nearest shells around the chosen absorber species. This technique permits the effective verification over the formation of a given structure and its variations from a theoretical model used as a starting point for the analysis.

While the physical basis and practical aspects of absorption spectroscopy have been known from 1930s, the actual accomplishment of a measurement is still a tricky question: on the practical side, the necessity of a focused, monochromatic high energy excitation beam narrows the list of possible sources to a number of beamlines in the synchrotron facilities available to external use, while problems concerning the measurement of beam intensity upstream and downstream of the experimental sample are a known but resolvable matter; on the analytical side however lies the most troublesome factor, given by the interpretation of experimental data. The extraction of photoelectron interference patterns (between the absorber atom and its neighbors) from raw data is a non-trivial but fundamental procedure, as the superposition of obtained scattering patterns is the touchstone upon which the model is fitted. The results of this procedure permit the tailoring of the proposed structure: from the fitting of experimental scattering paths versus calculated scattering paths it is possible to obtain structural parameters such as degeneracy, distance or disorder of neighbor atoms. By giving local informations on shells of neighbor atoms, EXAFS measurements permit to asses the formation of a given structure and its scale factors, thus giving a deeper knowledge on the crystal characteristics and on the possible role of doping species. Convenient variations in the wavelength of the incident radiation lead to excitation of different elements (e.g. the bulk element and the dopant): the comparison of analogous structural patterns from different chemical elements in the same crystalline site can offer an insight on the local changes caused by doping over the bulk structure.

2.3 Luminescence

Photoluminescence (PL) and thermoluminescence (TL) are useful techniques for energetic studies, whose results can be used in accordance with appropriate models to gain informations on specific aspects of the structural characteristics of measured materials.

Despite the differences between the two techniques, both give results that can be used with different degrees of insight depending on the goal of the analysis. The most immediate use of photoluminescence and thermoluminescence techniques is as a fingerprint for specific radiative emissions of interest, but on a more general note they can be used to characterize crystal structures by taking into account the occupation of the crystalline sites, the presence of defects or their recombination.

In this framework, theoretical models offer additional tools to analyze experimental results: the fitting of experimental data according to suitable models permits to gain a deeper insight of the physical systems underlying their occurrence.

3 **Outline**

Section 1 shows the experimental results obtained by Raman, EXAFS and PL spectroscopy on different perovskite materials ($LuAlO_3$, $YAlO_3$, $Lu_{0.7}Y_{0.3}AlO_3$,$YbAlO_3$). In particular, polarized Raman spectra of $LuAlO_3$, $Lu_{0.7}Y_{0.3}AlO_3$ and $YbAlO_3$ point out the effective formation of perovskite phase and the presence of a distorted structure. EXAFS spectra of $LuAlO_3$ allow the analysis of the local structural characteristics of an uncommon perovskite structure, while PL spectra of $YbAlO_3$ permitted a more performance-oriented analysis of a new material.

The analysis and crosschecking of these results led to a new insight in classification of these new materials whose structural knowledge was, up to now, sketchy.

Section 2 revolves around two studies on the role and behavior of different chemical elements acting as doping species in a RE crystal oxide matrix: a heavily Y-doped $LuAlO_3$ matrix was studied by EXAFS spectroscopy, while a very low Fe-doped $Y_3Al_5O_{12}$ sample was investigated by PL spectra and analyzed in the framework of zero phonon line coupling theory.

Different techniques were chosen accordingly to their capability of discerning the presence of dopants. As a consequence, the heaviness of doping was the leading factor in the selection of each technique. EXAFS spectroscopy was used to study the effective formation and local characteristics of perovskite structure around the heavy doping yttrium, while analysis on extremely low iron-doping in a $Y_3Al_5O_{12}$ matrix through Zero Phonon Line theory permitted to point at an elected crystalline site for doping from an energetic point of view.

In brief, these results show how different approaches can be used to obtain informations on the doping element depending on its percentage presence.

Section 3 is focused towards analyzing different crystal oxides (lutetium/yttrium aluminum perovskites, lutetium/yttrium aluminum oxyorthosilicates and titanium dioxide) by drawing attention to specific characteristics of actually grown materials and studying their possible exploitation. The compounds are studied in respect to their already known counterparts by spectroscopic techniques such as thermoluminescence, photoluminescence and Raman spectroscopy. In this common framework, different experimental evidences were pointed while the results were analyzed and interpreted in order to remark new possible applications.

In particular thermoluminescence permitted to measure the presence and abundance of oxygen vacancies in $Lu_{0.7}Y_{0.3}AlO_3$ crystals according to different growing atmospheres, while photoluminescence highlighted the differences caused by different growth techniques in stoichiometrically identical $Lu_{0.2}Y_{1.8}SiO_5$ samples.

Moreover, it was shown that experimental conditions during optical characterization might be as crucial as the ones during growing processes. These evidences were highlighted by Raman and photoluminescence spectroscopy, that showed crystal structure amorphization (anatase to amorphous phase) depending on the atmosphere of the experimental chamber.

At the end, covering the main points, this work should be regarded not only as a comprehensive tentative of structural analysis oriented, eventually, to improve or find new industrial applications of oxide materials doped with RE, but also as a promotion of the spectroscopic techniques and their capability to fulfill many diverse analytical expectations.

REFERENCES

1. Y.Zhao, B. Qi, X. Ma, H.-K. Lo and L. Qian – Phys. Rev. Lett., 96 **2006**, 070502.
2. Z. L. Yuan, A. W. Sharpe and A. J. Shields – Appl. Phys. Lett. 90 **2007**, 011118.
3. R.T. Collis – Appl Opt 9- 8 **1970**, 1782-8.
4. A.Anedda, C.M. Carbonaro, D. Chiriu et al. – IEEE J Quantum Electron 42 5-6 **2006**, 563-569.
5. V. Švedas, V. Vaicikauskas and M. Kaucikas – Lithuanian J Phys 50-.3 **2010**, 351–362.
6. T.H. Maiman – Nature 187 **1960**, 493.
7. J.E. Geusic, H.M. Marcos and L.G. Van Uitert – Appl. Phys. Lett. 4-10 **1964**, 182-184.
8. B.J. Dinerman, P.F. Moulton and D. M. Rines – OSA Proceeding on advanced solid state lasers 14 (OSA, Whashington) **1993**.
9. K.R. Hoffman, U. Hömmerich, S.M. Jacobsen and W.M. Yen – J Lumin 52 5-6 **1992**, 277-279.
10. G. Blasse and A. Bril – Appl. Phys. Lett. 11 **1967**, 53-54.
11. N. Ohlsson, M. Nilsson, S. Krll and R.K. Mohan – Opt Lett 28-6 **2003**, 450-452.
12. V. Lupei, G. Boulon et al. – Proceedings Vol. 1864 Solid State Lasers IV **1993**

Section 1

This section presents the structural characterization of different perovskite crystals of the *x*-AlO_3 class by means of diverse spectroscopic techniques ranging from Raman to Photoluminescence (PL) and Extended X-Ray Absorption Fine Structure (EXAFS) spectroscopy. The results obtained by Raman spectroscopy offer a first evidence on the formation of perovskites, due to their possible use as a structural fingerprint, while further analysis by EXAFS or PL spectroscopy remark different characteristics of each compound, depending on the goal of the analysis. All in all, the results shown in this section can also be intended as possible first steps in a general process of a full characterization procedure, starting from a structural analysis of the matrix and moving to the role of dopants and means of growth.

1.1 Raman spectroscopy of perovskite crystals

The development and study of materials with high efficiency output, fast response and high density for scintillation purposes generated a great interest in recent years. However, the difficulty in finding out a compound that fits all the mentioned characteristics has often lead to choose materials suitable for just a partial set of different applications. Among the possible fields of research, the fast scintillation light emission of cerium-doped scintillators has attracted a broad interest on scintillation materials containing Lutetium such as Lu_2SiO_5 (LSO), $Lu_{2-x}Y_{2x}SiO_5$ (LYSO), $LuAlO_3$ (LuAP), $Lu_{1-x}Y_xAlO_3$ (LuYAP) crystals despite the sketchy knowledge on their structural characteristics. A typical example of the motives at the base of the lack of structural informations for these materials can be given by the case of Cerium-doped lutetium Aluminum perovskite. Ce:$LuAlO_3$ has been widely known for a number of years as a good candidate for scintillator applications due to its characteristics of high light yield, good energy resolution and short decay time[1]. However, its diffusion was slowed down by two orders

of difficulties: in the first place the practical ones that are commonly encountered in the growth process of single crystals, such as the necessity of high temperatures for the melt and the choice of parameters during the pulling process; on top of this, economic problems caused by the high cost of the starting materials should also be taken into account. The coupling of these two different problems, each of whom could have been overcome by itself, prevented a wide diffusion of LuAP up to recent times. As a consequence, although the material cannot be labeled as completely new [2], it has been put aside for a long time and even in recent times the majority of literature works was devoted towards studies with an immediate applicative effect [3-6], while a full structural characterization is still missing.

On the other hand a possible way of development for new compounds was given by Yb-based scintillators, which show a faster time response than cerium-based ones (a lifetime smaller than 10 ns, versus 30 ns of Ce:LSO), despite their lower optical response. In this regards, the charge transfer luminescence of Yb^{3+} is an attractive subject for the development of new scintillator materials for neutrino detection in high energy physics experiments. In particular, recent results on Yb doped $YAlO_3$ revealed a maximum light output of 3000 eh/MeV at 105 K and a light yield of 7.5% (in respect to the one of BGO ($Bi_4Ge_3O_{12}$)), which suggest that Yb:YAP can be an attractive scintillator also for nuclear imaging applications (PET (Positron Emission Tomography)). However, the maximum known limit in the substitution of ytterbium over yttrium in a YAP-like stable structure was given by a 45% Yb- 55% Y ratio. The achievement of the total substitution of Yttrium with Ytterbium ions allowed to grow for the first time a pure Ytterbium Aluminum Perovskite crystal (YbAP).

A structural characterization of perovskite compounds of both families can be rightfully commenced from Raman spectroscopy, where a comparative approach with results from $YAlO_3$ (which is a fairly known compound) can be exploited in the analysis of new materials. Variations in the occupation of the same crystalline site by different chemical elements is expected to cause changes in the Raman peaks in respect to the $YAlO_3$ case, while always keeping in accordance with the general characteristics of this

class of materials, which can be obtained by symmetry group theory.

Yttrium aluminum perovskite (YAP), lutetium/yttrium aluminum perovskite (LuYAP), lutetium aluminum perovskite (LuAP) and ytterbium aluminum perovskite (YbAP) are orthorhombic perovskites of the D_{2h}^{16} space group, featuring a 20 atoms unit cell. The general structure of perovskite crystals can be expressed as ABX_3, where elements A and B occupy, respectively, the vertexes and the central site of the body centred cube, while X anions, situated on the six faces of the cube, form an octahedron around the central site B.

In particular, B cations are coordinated by six X anions (forming an octahedron), while A cations are coordinated by 12 anions (forming a cuboctahedron). The X anions have coordination number 2 and are generally represented by oxygens, being coordinated by two B cations, since the distance A-O is about 4 timeș larger than the B-O bond distance. Actually, "A" and "B" are two cations of very different size and in general the larger A atom is the main cause of the overall size of the AO_3 (fcc) structure. In particular, pbnm perovskites feature A cations and four oxygen atoms (denoted by O_I) in (4c) positions, B cations in (4b) positions, while the rest of the oxygen atoms (denoted by O_{II}) are situated in the general (8d) positions.

Figure 1.1.1 shows the unit cell of a orthorhombic **A**-AlO_3 perovskite with Pbnm structure: it features a network of cornersharing AlO_6 octahedra and belongs to the family of rotationally distorted perovskites with Glazer's notation ($a^-b^+a^-$). A and B sites of the cell are occupied respectively by lutetium and aluminum: the former occupies the corners of the orthorhombic structure, while the latter occupies the centre of the body-centred orthorhombic structure.

The formation of an orthorhombic structure over the theoretical cubic one can be expected from purely chemical considerations. A perfect perovskite structure ABX_3 respects the relation

$$a = \sqrt{2}(R_A + R_X) = 2(R_B + R_X) \qquad (1.1.1)$$

, where *a* indicates the cubic cell parameter and R_A, R_B and R_X indicate the ionic radii of the compound. Variations in the constructing elements, and consequently in ionic radii, don't imply the impossibility of perovskite formation despite the non validity of the above mentioned relation.

A tolerance factor *t* was first proposed by Goldschmidt and defined as

$$t = \frac{R_A + R_X}{\sqrt{2}(R_B + R_X)}. \qquad (1.1.2)$$

A cubic perovskite, whose radii respect relation 1.1.1, has a tolerance factor value of 1, while generic variations in ionic radii of atoms in A or B sites will result in values of the *t* parameter above or below the unit value. The presence of elements with increased or decreased ionic radius in respect to the cubic condition leads to t values larger or smaller than 1. From a structural point of view variations in *t* factor hint at the formation of different structures: while *t* values larger than 1 correspond to the formation of $BaNiO_3$-type structures with face-sharing octahedra, *t* values comprised between 0.80 and 1 correspond to the formation of perovskite structures. Obviously perovskites with *t* factors in the range 0.80 – 1.00 have different structural characteristics, as the decrease in size of the A ion corresponds to a variation in cell dimensions and a tilt of BX_6 octahedra in order to fill space, thus lowering the symmetry of the crystal: in particular ABX_3 crystals with *t* factors going from 1 to 0.89 still keep a cubic structure [7,8], while compounds with lower *t* factors (down to 0.80) present perovskite structures with an increased octahedra tilting and a inhomogeneous variation of cell parameters that results in the passage from cubic to orthorhombic crystals. In light of these facts, *t* factors can be calculated for the compounds under analysis, with values comprised between $t = 0.836$ ($LuAlO_3$) and $t = 0.851$ (YAP): the crystals can be expected to be slightly distorted orthorhombic perovskites.

Aside from these considerations based on experimental data, the aforementioned structure, common to all the considered compounds, can be obtained from the simple perovskite structure by two consequent rotations of AlO_6 octahedra, namely, 1) Around the [010] direction of cubic perovskite (y axis in

Pnma); 2) around the [101] direction of cubic perovskite (x axis in Pnma) [9]. The irreducible point representations of this symmetry group allows 24 Raman active vibrational modes (on a total of 60) [10]:

$$\Gamma = 7A_{1g} + 7B_{1g} + 5B_{2g} + 5B_{3g} + 8A_{1u} + 8B_{1u} + 10B_{2u} + 10B_{3u} \qquad (1.1.3)$$

among them the Raman active modes are: 7 A_{1g} modes, 7 B_{1g} modes, 5 B_{2g} modes and 5 B_{3g} modes. Each of these vibrational modes can be assigned to different atomic motions, although not everyone of them was shown by our measurements.

The unpolarized Raman spectra of powder samples recorded at ambient pressure and temperature conditions, such as the one illustrated in Figure 1.1.2, show several bands in the 100–600 cm^{-1} spectral range, some of which are not resolved and/or overlapped and did not allow a clear identification of the different vibrational modes. This problem led to the choice of acquiring differently-polarized Raman spectra along the three main axes of the crystal in order to show the Raman active modes.

For crystals in the D_{2h}^{16} space group, it is possible to discriminate between all the permitted vibrational modes by choosing different Raman polarization configurations along single crystal samples. Defining a tern of orthogonal axes x, y and z with z along the highest symmetry axis, the Ag vibrational modes should be observed when the components of the polar tensor xx, yy, zz are non-null, while contribution to the B_{1g}, B_{2g} and B_{3g} modes should be given, respectively, from xy, yz and xz components. Operatively, the condition is achieved by adequately choosing the geometrical and the polarization configurations during the acquisition of Raman spectra. A_{1g} modes were measured in backscattering configuration by arranging the polarizer in parallel with the incident radiation, polarized along one of the three main axis, while B_{1g}, B_{2g} and B_{3g} modes were obtained in backscattering configuration by switching the incident crystal face while arranging the polarizer in order to allow the transmission only of the non-parallel radiation. The independent exact scattering configurations obtained with the

Figure 1.1.1 Sketch of the unit cell of a PBNM $\boldsymbol{A}AlO_3$ crystal: blue spheres indicate generic ***A*** atoms, purple spheres indicate aluminums and red spheres indicate oxygens.

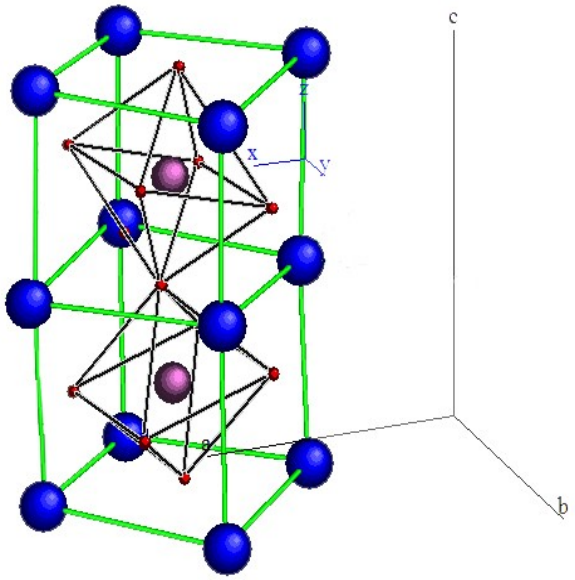

Figure 1.1.2 Unpolarized (black) vs. polarized (red and blue) Raman spectra of $LuAlO_3$ perovskite.

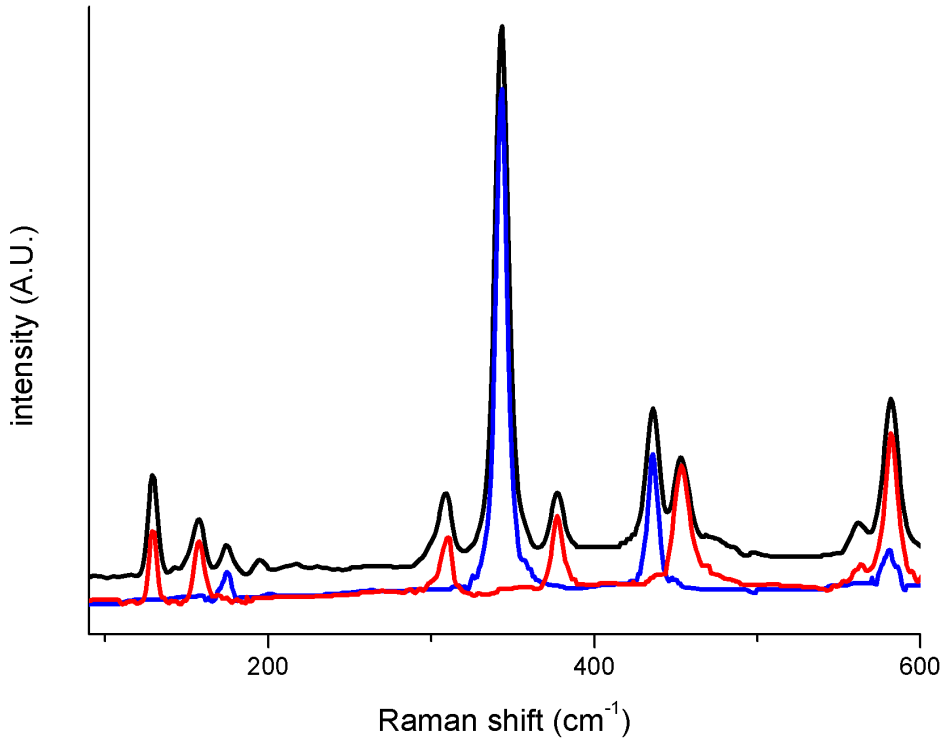

polarization of incident and scattered light along the principal crystal directions and the allowed phonon mode symmetries in each configuration can thus be obtained. The results relative to all the compounds are shown in Table 1.1.1 and Figure 1.1.3 A-C.

The analysis of the measured spectra showed the presence of A_{1g}, B_{1g}, B_{2g} and B_{3g} vibrational modes for all the samples. In particular, LuAP samples show the presence of seven A_{1g} modes, two B_{1g} modes, four B_{2g} modes and three B_{3g} modes; LuYAP samples feature seven A_{1g} modes, three B_{1g} modes, four B_{2g} modes and three B_{3g} modes; finally, for YbAP samples it is possible to assign six A_{1g} modes, three B_{1g} modes, four B_{2g} modes and three B_{3g} modes. The exact value of each Raman active vibrational mode and the corresponding attribution is shown for all the three compounds in Table 1.1.1 .
The A_{1g}, B_{1g}, B_{2g} and B_{3g} vibrational modes of LuAP, LuYAP and YbAP were assigned by comparison with their vibrational correspondents in similar perovskites, particularly YAP, as shown in Table 1.1.1 [11,12]. The occurrence of a varied population on one of the crystal sites allows to point out different shift effects caused by the presence of RE (lutetium and ytterbium in the present case) on A_{1g} ,$B_{1g,}$ B_{2g}, B_{3g} vibrational modes.

A-site vibrations are not the only modes subject to changes, but variations can be registered also for modes corresponding to vibrations of the AlO_6 octahedra, such as the case of the first B_{1g} vibrational mode. This mode, corresponding to an out-of-phase rotation of the AlO_6 octahedra, presents a strong variation in position from its value relative to YAP samples both in the case of a total substitution of yttrium by ytterbium and in the cases of substitution by lutetium: in particular, it can be observed that in the latter case the variation proportionally to the increasing presence of lutetium in the A site of the cell causes a blue-shift of approximately 40 cm^{-1} between YAP and LuAP crystal (from 258 to 299 cm^{-1}).

Figure 1.1.3 LuAP, LuYAP, YbAP Raman modes revealed through different geometries. Porto's notation has been used to describe the scattering geometry. The spectra were taken at room temperature on single crystal samples.

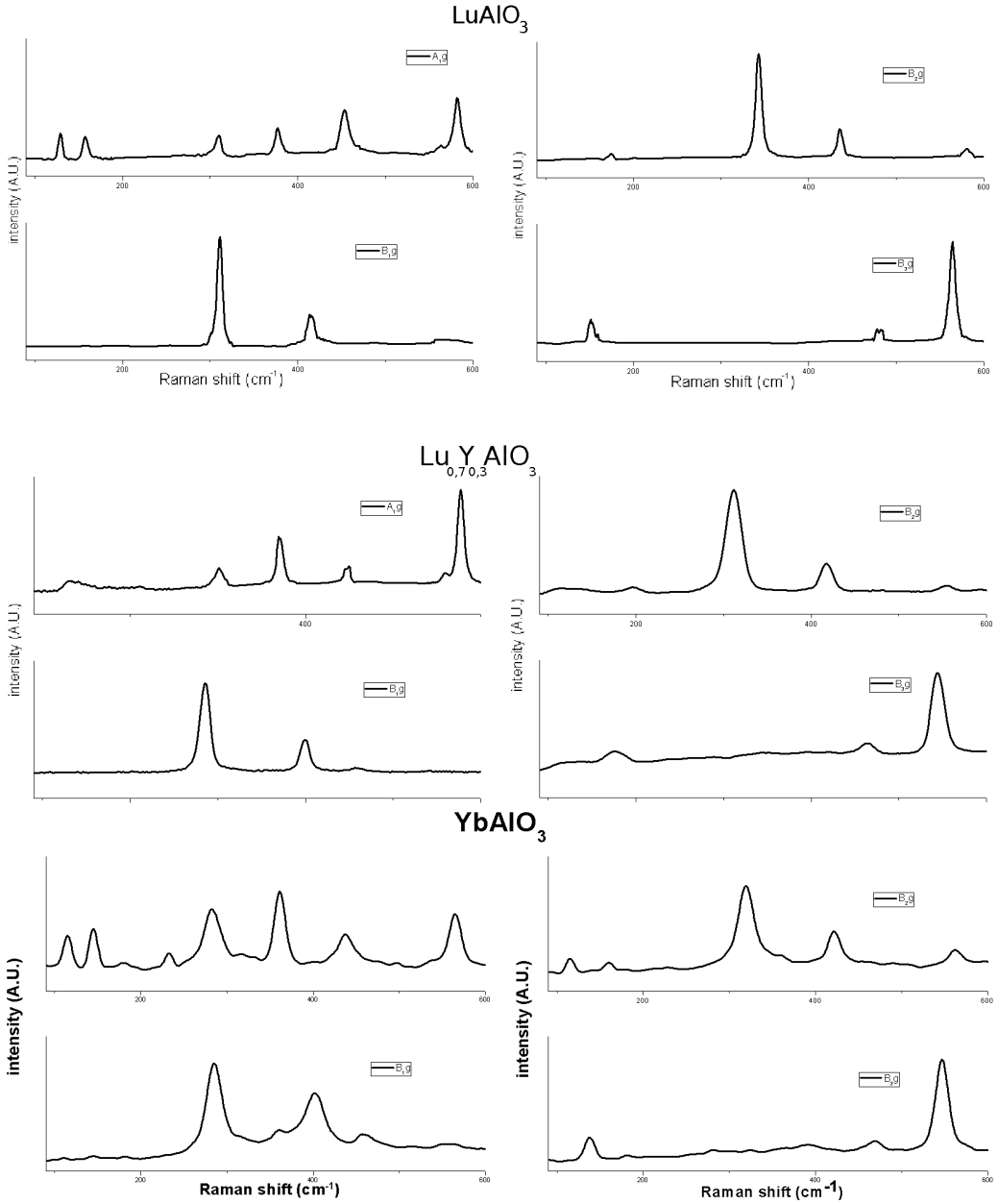

Table 1.1.1 Raman peaks, vibrational modes and assignment of YAP LuYAP, LuAP and YbAP crystals.

YAP (cm^{-1})	LuYAP (cm^{-1})	LuAP (cm^{-1})	YbAP (cm^{-1})	Vibrational modes	Assignment
144	123	117	114	A_1g	R(x)
187	177	136	138	B_3g	R(z)
190	190	145	144	A_1g	R(y)
217	196	164	160	B_2g	R(x)
258	280	299	283	B_1g	Out-of-phase rotations of AlO_6 around y
265	287	295	285	A_1g	In-phase rotations of AlO_6 octahedra around y
280	311	330	319	B_2g	O1(z)
336	357	364	361	A_1g	O1(x)
398	400	401	403	B_1g	In-phase rotations of AlO_6 octahedra around x
408	416	424	422	B_2g	Out-of-phase bending of AlO_6 octahedra
403	430	440	463	A_1g	Out-of-phase rotations of AlO_6 around x
462	458	-	464	B_1g	Out-of-phase stretching of AlO_6 in xz-planes
-	466	465	469	B_3g	Out-of-phase bending of AlO_6 octahedra
533	540	550	-	A_1g	Out-of-phase bending of AlO_6 octahedra
540	545	550	548	B_3g	Out-of-phase stretching of AlO_6 octahedra
544	555	569	561	B_2g	In-phase bending of AlO_6 octahedra
550	563	571	564	A_1g	In-phase stretching of AlO_6 in xz-plane

In fact, a general analysis of the polarized spectra of LuAP, LuYAP and YbAP in comparison with similar perovskites can help in stressing the differences and thus the role of the varying chemical elements in the general **A**-AlO_3 structure. The total substitution of yttrium with ytterbium determines various shifting in Raman modes of YbAP samples in respect to YAP ones, while a strong similarity can be observed with vibrational modes of LuAP samples: the latter comes as no surprise, given the small difference in radius between lutetium and ytterbium, whereas the differences with YAP can be observed more extensively by comparing analogous vibrational modes from LuAP, LuYAP and YAP. These compounds allow the identification of different trends with the increasing substitution of lutetium over yttrium, resulting in both red-shifts and blue-shifts of the Raman modes. In the low-energy region, where the peaks are caused by vibrations of rare earth in the A site (the region up to 295 cm^{-1} in the spectra of LuAP), the presence of Lu over Y causes an unambiguous red-shift of the modes. On the other hand, two distinct classes of vibrations can be distinguished in the high energy region: Raman peaks due to rotations and bendings of the AlO_6 octahedra and vibration of oxygen atoms are present and overlapped in energy terms. These high-energy modes generally present a blue-shift proportionally to the presence of lutetium, although a couple of different trends will be pointed out.

In order to comprehend both the red- and blue-shifts, it's worth trying to comprehend the effects of the Lu/Y occupation of the A site from a structural point of view. The chemical element occupying the A site of the crystal structure directly influences the dimension of the body centered cuboctahedron: the substitution of Lu or Yb (having a smaller radius than Y) over Y determines a shrinking effect. However the decrease in energy of the RE vibrational modes seems to be just mildly influenced by it, while it is heavily dependent on the mass of the A-site ion: in the light of this fact the idea of the vibrational frequency being strongly dependent on the square root of mass of the A-site ions ($m_R^{-1/2}$) is a sound assumption if paired with the varying occupation by lutetium over yttrium. The shrinking of A-sites-polyhedra plays a far more important role in the variations of both types of higher energy

vibrational modes, because its effect on oxygen and AlO_6 octahedra (formed around the central site of the lutetium polyhedra) vibrations can be considered analogous to external stress, whose expected effect is a shift towards higher wavenumbers of the Raman peaks. On the other hand, the faint red-shift observed for a B_{1g} and one B_{3g} modes relative to AlO_6 octahedra vibrations should be ascribed to a particular matching effect of two distinct contributions: the inhomogeneity observed in the shrink of the RE polyhedra is hinted by a inhomogeneous decrease of the b cell parameter, while on the other hand it is paired with a decrease in radius of the RE at the center of the AlO_6 octahedra. These factors can concur to reduced energies in vibrational modes.

The analysis of Raman spectra collected in the range 20÷290 K was performed in order to see the dependence on temperature of the vibrational modes identified at room temperature, thus allowing to understand the degree of distortion of the perovskite.

Figure 1.1.4 reports, as an example, the B_{2g} LuAP Raman modes collected at 20 K and at 290 K in the above mentioned scattered geometry. The first highlight coming from this analysis is the rigid blue-shift of the peaks in the spectra recorded at 20 K: the shift of the Raman peaks with decreasing temperature confirms that the shrinking of the crystal causes a decrease in cell dimensions that is in good accordance with a shift of the peaks towards high wavenumbers [13]. In second instance, Raman peaks collected at 20 K show a reduced spectral width, hinting to the fact that mean phononic lifetime is mainly influenced by variations in temperature, as opposed to scattering due to reticular imperfections: this fact lead us to hypothesize a weak distortion of the perovskite crystal [14].

To sum up, $LuAlO_3$, $Lu_{0.7}Y_{0.3}AlO_3$ and $YbAlO_3$ crystals were analyzed by means of Raman spectroscopy. In particular, polarized Raman spectroscopy was used to achieve a complete analysis of the vibrational modes of the crystals in the temperature range of 20÷290 K. The characterization of the crystal structure was obtained by giving an assignment to every vibrational mode and analyzing the experimental results by comparison with experimental results of YAP crystals.

Figure 1.1.4 Polarized Raman spectra of B_{2g} Raman modes of LuAP collected at 20 K (red) and at 290 K (black).

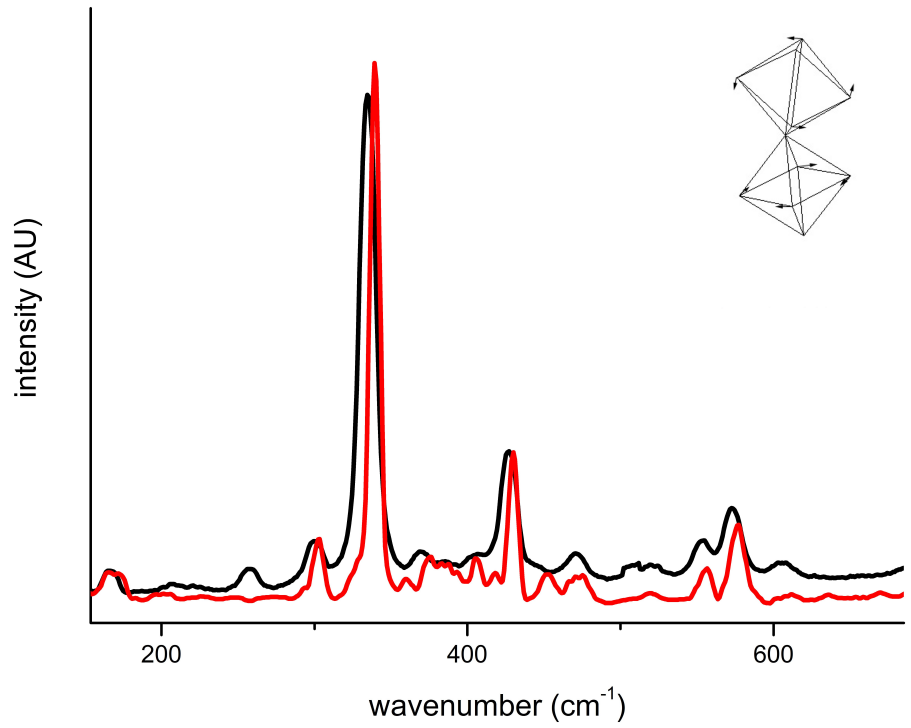

Moreover, a comparative analysis of vibrational modes of all the measured compounds allowed the identification of two spectral zones, each relative to vibrations of different crystal sites, and the comprehension of the trends in Raman spectra due to the variations of chemical elements forming the crystal: a low wavenumbers zone, homogeneously affected by variations in mass of the chemical elements, and a high wavenumbers zone, whose dependency on the radius of chemical elements is less straightforward. EXAFS spectroscopy, performed in transmission in the temperature range of 80÷290 K on $LuAlO_3$, can be used to obtain structural data and to achieve a direct measurement of the local structural characteristics and parameters and on their variations with temperature for this compound, whose structural informations, as previously stated, are still sketchy despite its relative oldness. Moreover, structural informations obtained by EXAFS analysis can be well compared with results obtained by Raman spectroscopy, thus giving an overall agreement over the characteristics of $LuAlO_3$.

1.2 EXAFS measurements of lutetium aluminum perovskite crystals

LuAP was investigated by means of EXAFS spectroscopy in transmission mode at the L_3 absorption edge of lutetium (relative energy resolution being $2*10^{-4}$) at the XAFS beamline of the Elettra synchrotron facility in Trieste (Italy), with an average beam current of 120 mA (multibunch) and a working energy of 2.4 GeV. The spectra were collected at room temperature and at low temperature (80 K) in order to assess the formation of an orthorhombic perovskite and measure thermal variations in its structure (see Table 1.2.1 for the main fitting parameters and results). All the ionization chambers were kept at a total pressure of 2 bars by filling them with appropriate gas mixtures of He, Ne_2, Ar and Kr for the absorption edge of choice (the L_3 edge of lutetium (9244 eV)). The experimental chamber was kept in high vacuum conditions by a rotative/turbomolecular pump system in order to perform the measurements in a low temperature regime of 80 K to enhance the quality of the signal by minimizing its damping due to thermal effects. The presented data are averaged over 3 cycles of collection and are

relative to pellets composed by a mixture of crystalline nanopowders and polivinilpirrolidone (PVP), used to improve their stability. The resulting data were weighted by k^2, in order to enhance the signal arising from the compound in the fitting ranges of choice, and fitted in R space in the range 1.1 – 3.9 Å (k-range being 2.0 – 11.6 $Å^{-1}$) using the IFEFFIT suite of programs [15].

The fitting procedures were carried out using the IFFEFFIT package, whose analysis of EXFAS data starts from a user-defined theoretical model of the crystal structure (in our case a perovskite structure with sound $LuAlO_3$ cell parameters [16]). This approach allows to check the validity of such model and, on the other hand, obtain comparable informations on the temperature-related shrinking calculated by such procedures, given the common starting model and set of fitting parameters. Fitting of EXAFS data was achieved using the first fifteen scattering paths calculated by IFEFFIT, them being single scattering paths between the central atom and all the atoms of the unit cell plus the ones relative to the next-nearest lanthanide ions. Among these paths three different shells can be distinguished: a first shell of oxygens, a second one featuring both oxygen and aluminum atoms, and a final shell featuring the first six lanthanide neighbors (radially divided in three pairs: one along the Z axis and two in the horizontal plane). The fitting parameters were consequently chosen in order to take into account the presence of different chemical elements in different shells. Figure 1.2.1 reports a sketch of radial distribution of the different shells in respect to the central absorption site.

The goodness of the fitting results was given by a parameter measuring the absolute misfit between theory and data, called R-factor. It can be expressed by the formula

$$R=\sum_i \frac{[\Im m(\chi_{dat}(R_i)-\chi_{th}(R_i))]^2+[\Re e(\chi_{dat}(R_i)-\chi_{th}(R_i))]^2}{[\Im m(\chi_{dat}(R_i))]^2+[\Re e(\chi_{dat}(R_i))]^2}. \qquad (1.2.1)$$

where $\chi(R)$ indicates the sum of oscillatory signals arising from scattering processes involving photoelectrons ejected from the X-ray absorbing atom, scattering from its neighbors of different shells

Figure 1.2.1 Sketch of the shells used during the fitting of EXAFS data of xAlO$_3$ crystals (different colours are used for different shells, not for different chemical elements). The first shell (blue) features oxygen atoms, the second shell (green) features aluminum and oxygen atoms and the third shell (red) features next-nearest lutetium atoms.

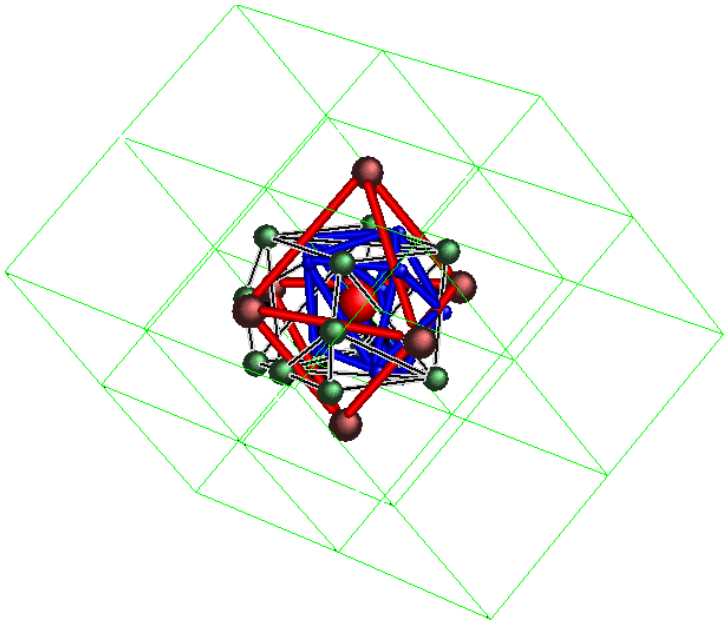

TABLE 1.2.1 Fitting ranges and main results from the best fitting curves of EXAFS data of LuAP, collected at room temperature and at low temperature. R factor indicates misfit between theory and data, while S^2_0 indicates the amplitude reduction term.

	Room Temperature	Low Temperature (80 K)
k range (Å $^{-1}$)	2.0- 11.6	
R range (Å)	1.1 – 3.9	
R factor	0.02703	0.02759
S20	1.02655	0.98301

and returning back to its origin.

The main goal of the analysis was to calculate the structural characteristics of the region centered around the lutetium atom up to its nearest Lu neighbors. A set of fitting parameters was consequently chosen, trying to minimize its number for sake of goodness of calculations among the shells previously indicated. Parameters of bonding distance were used depending on the element involved and on the distance from the scattering origin, while σ^2 parameters were chosen so that contributions were given according to distance from the absorbing center rather than chemical elements involved in the scattering paths. The results of fitting procedures are shown in Figure 1.2.2 and in Table 1.2.2.

The first results from the analysis of fitted room temperature spectra is the good agreement between theoretical model and experimental data, as a theoretical model with incorrect atomic or cell parameters would have caused major variations in the fitted scattering distances in respect to the modeled ones in order to adhere to experimental data. A comparison between the results obtained with spectra measured at room temperature and spectra measured at low temperature offers a further confirmation, since a small decrease in bond lengths as a function of temperature can be observed, while keeping the overall trend on the characteristics of scattering paths. In particular, thermal shrinking affects slightly the nearest paths (with an overall decrease on the second decimal integer), while Lu-Lu scattering paths show a decrease in the order of the first decimal integer. These results hint at the possibility that the volume of low temperature LuAP orthorhombic cell is slightly smaller and non-uniformly distorted in respect to the one measured at room temperature. A comparison between theoretical and room temperature data with the fitting results of low temperature spectra show the expected thermal shrinking albeit with some differences among chemical elements in different crystal sites.

Figure 1.2.2 R-space EXAFS data (in black for magnitude and in blue for imaginary component) and best fitting curves (in red for magnitude and in green for imaginary component) of LuAP collected at low temperature (above) and room temperature (below) at the L_3 absorption edge of lutetium (9244 eV). K-space data are shown in the insets.

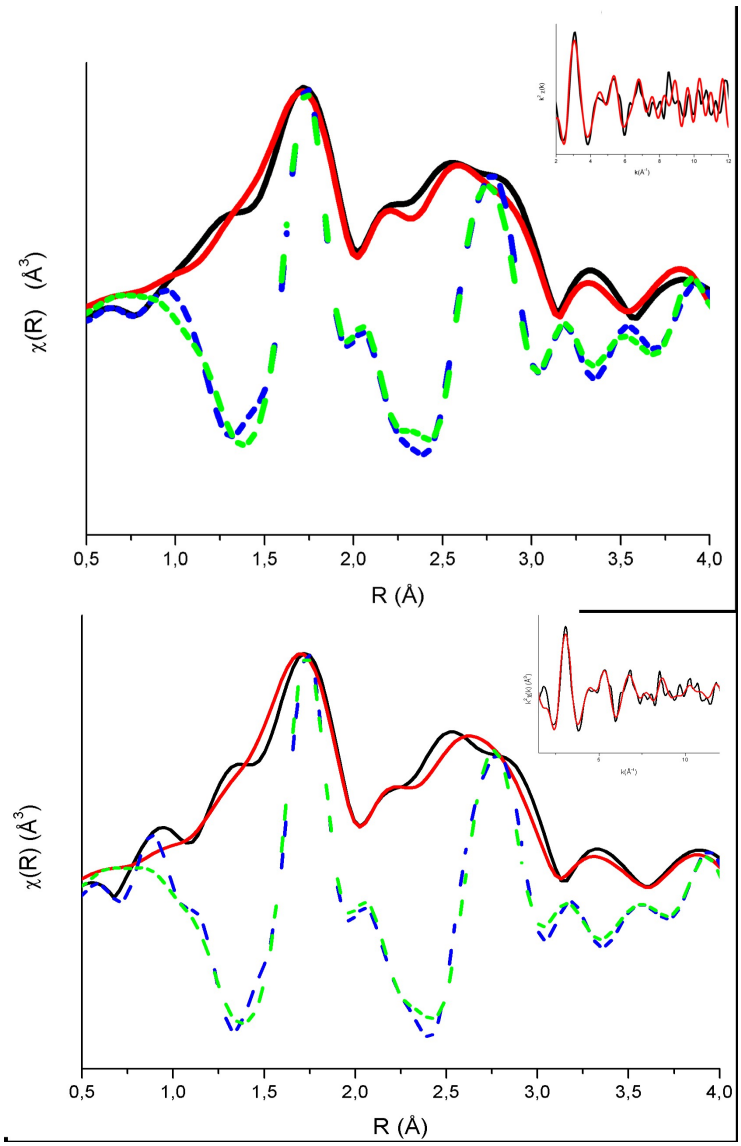

TABLE 1.2.2 Distances of single scattering paths obtained from the best fitting curves of LuAP EXAFS data collected at room temperature and at low temperature.

Single scattering paths	Model data	Room Temperature data			Low temperature data	
	R eff (Å)	dR (Å)	R (Å)		dR (Å)	R (Å)
Path 1: [O1_1]	2.223	0.000	2.223		0.008	2.231
Path 2: [O2_1]	2.286	-0.100	2.186		-0.102	2.183
Path 3: [O1_2]	2.313	0.000	2.313		0.008	2.321
Path 4: [O2_2]	2.448	0.000	2.448		0.009	2.456
Path 5: [O2_3]	2.545	0.000	2.545		0.009	2.554
Path 6: [O1_3]	2.943	0.000	2.943		0.010	2.953
Path 7: [Al_1]	3.004	0.034	3.038		0.042	3.046
Path 8: [Al_2]	3.100	0.035	3.135		0.043	3.144
Path 9: [O1_4]	3.108	0.000	3.108		0.011	3.119
Path 10: [Al_3]	3.198	0.036	3.234		0.045	3.242
Path 11: [O2_4]	3.216	-0.141	3.076		-0.144	3.072
Path 12: [Al_4]	3.467	0.039	3.506		0.048	3.515
Path 13: [Lu1_1]	3.607	-0.132	3.475		-0.034	3.573
Path 14: [Lu1_2]	3.695	-0.074	3.621		-0.018	3.677
Path 15: [Lu1_3]	3.774	-0.075	3.699		0.028	3.802

TABLE 1.2.3 Comparison between cell dimensions reported by literature and obtained by the best fitting curves of LuAP EXAFS data collected at room temperature.

	a (Å)	*b* (Å)	*c* (Å)
Literature data (Ref.2)	5.1012	5.3320	7.3000
XAFS fit	5.0980	5.2802	7.2653

A general decrease in scattering distances for all the considered paths can be expected, a non uniform variation can be found in Lu-O scattering paths: while minor systematic variations occur in O_I sites, O_{II} sites don't seem to be homogeneously affected by thermal shrinking. A lack of homogeneity can also be observed in Lu-Lu scattering paths, whose thermal shrinking is anisotropic and features a smaller decrease in the distances of scattering paths along the z axis of the crystal. In any case, scattering paths between lutetium atoms are still the ones undergoing the heaviest thermal effects and are therefore the main candidates in order to obtain information on the actual shrinking. In fact the six lutetium neighbors are divided along three radially different scattering paths as three symmetric pairs of lutetium atoms centered in the absorbing site (two pairs in the horizontal plane and a third one on the z axis).

By looking at the Pbnm structure it's possible to see that atoms in (4c) positions are the ones mainly subject to thermal effects, thus confirming the initial assumption that cell dimensions are heavily related to A sites behaviour (in our case Lu). Given these characteristics, variations of cell parameters can be directly measured from the distances between the absorbing lutetium center and its first lutetium neighbors with some basic geometrical calculations coming from the positions of lutetium atoms according to the structure. The results of these calculations show that cell parameters at room temperature can be calculated as a = 5.09802 Å, b= 5.28023 Å, c= 7.26527 Å (195,571 $Å^3$), while a general downsizing of the cell dimensions is found from the analysis of data collected at 80 K, whose cell parameters are esteemed as a = 4.95924 Å, b= 5.13606 Å, c= 7.15460 Å (182,235 $Å^3$). A comparison between fitted cell dimensions and data from literature shows a slight downsizing of the first in respect to the latter (TABLE 1.2.3).

The importance of structural studies of lutetium aluminum perovskites is not only restricted to its role in Cerium-doped mixed lutetium/yttrium aluminum perovskites. In fact, although Ce-activated lutetium

oxyorthosilicate (LSO, Lu_2SiO_5:Ce) has been clearly established as a leading scintillator material in the area of medical imaging thanks to its superior scintillator characteristics, many researchers believe that it is possible to develop a material that would display even better scintillation properties. It is now fairly well established that scintillation light in LSO is produced at two different sites (Ce_1 and Ce_2) one of which (Ce_2) is strongly quenched at room temperature. The dominant Ce_1 site emission (unquenched at ambient temperatures) decays with the time constant of about 35 ns and any faster components in the scintillation time profiles of LSO are due to the quenched emission from the Ce_2 site. Clearly part of the energy deposited in the LSO host by ionizing radiation is lost to non-radiative processes introduced by inefficient Ce_2 sites.

The scintillation properties of Ce-activated LuAP, in a pure perovskite monocrystal phase were first studied and reported by Lempicki and coworkers at the 1994 IEEE Nuclear Science Symposium. It is worth to note that LuAP features only one Ce site and the radiative lifetime of the excited Ce^{3+} ion in this site. As a consequence, the decay time of the dominant scintillation component (at about 360 nm), is only about 17 ns, the shortest scintillation decay time in any known Ce-activated scintillator material.

1.3 Photoluminescence measurements of ytterbium aluminum perovskite crystals.

Ytterbium aluminum perovskite (YbAP) is a brand new compound, whose development can be set among Yb-based materials with possible application as an alternative to Ce-doped crystals in the field of scintillation [17-20]. A study involving its characteristics based on charge transfer luminescence is of great importance for two different reasons: in the first place for the possibility of immediate applications as scintillator and, on a more general note, for the opportunity to obtain fundamental insights in the optical properties of Yb ions that can be extended to other Yb-based crystals.

Charge transfer (CT) optical transition in a solid-state structure implies the transfer of the involved electron from ligand to central metal ion, with some of the absorption transitions possibly followed by

the radiative return of the system to its ground state. In some cases the radiative recombination is subsequent to non radiative processes to lower levels and only the final step features a luminescent process, as for Eu^{3+}:Y_2O_3 . This phosphor absorbs in the UV range with a transition to the charge transfer state of the Eu^{3+} ion and luminescence occurs from the ^5D_J states after non-radiative decay to the lower 4f levels.

The Yb^{3+} ion presents a very efficient charge transfer luminescence, since the only excited 4f state ($^2F_{5/2}$) is located 10000 cm^{-1} above the ground $^2F_{7/2}$ state and no other absorption band has been identified. Because of the large energy difference between the charge transfer state and the highest excited 4f state, non radiative channels such as OH vibrational levels are precluded in principle and charge transfer luminescence can be observed.

The excitation and emission spectra of the Yb^{3+} charge transfer luminescence band are shown in Figure 1.3.1. The edge of the excitation spectrum coincides with the edge of the charge transfer absorption transition observed in Yb-doped perovskites, suggesting that a partial overlap with the fundamental gap of the crystal could no be excluded [21]. The emission spectrum, excited at 250 nm, presents two bands, peaked at about 340 nm and 500 nm, assigned to the radiative recombination from the charge transfer level to the $^2F_{7/2}$ and to $^2F_{5/2,}$ respectively, in agreement with the predicted energetic separation of about 10000 cm^{-1}[22, 23], which could also be measured by near-IR absorption. No radiative emission from $^2F_{5/2}$ level to $^2F_{7/2}$ was observed in the IR spectral region. The fast RT decay time of YbAP sample is reported in the inset of Figure 1.3.1. It was previously reported that a 30%Yb-doped YAP crystal showed two time components at room temperature, with time constants of 0.87 ns and with 2.2 ns for the faster and slower components respectively [24, 25]. However, due to the laser pulse width of 8 ns (laser pulse time profile is also shown in the inset) we can just give an estimation of the time decay in ytterbium aluminum perovskites at room temperature. Actually, time measurements were performed also with synchrotron radiation at DESY with excitation wavelength at 250 nm. Though not

reported here, those measurements are in good agreement with the above shown time decay analysis: in particular the fast decay time component at room temperature was estimated in 1 ns, but it is worth noting again that the time response of the acquisition system (about 1 ns) does not permit a more accurate evaluation.

The time evolution of Yb radiative decay can be better observed in the 3D plot obtained at 10 K (Figure 1.3.2, temporal resolution of 1 ns). The plot shows that the same time kinetic is observed for the whole spectrum. The two bands of $Yb_{CTS} \rightarrow {}^2F_{7/2,}$ $Yb_{CTS} \rightarrow {}^2F_{5/2}$ recombinations present a very weak shift towards high energy and a reduced full width at half maximum with respect to room temperature measurements (peaks at 336 and 480 nm respectively). From the analysis of time decay curve (see inset in Figure 1.3.2) it is possible to observe at least two decay components. The red line in the inset of Figure 1.3.2 represents the curve fitting obtained with two exponentials with time decay of 6.1 ns and 34.2 ns respectively. The well pronounced non-single-exponential decay and the decrease of decay constant with increasing temperature indicate thermal activated luminescence quenching of Yb^{3+} ions.

The nature of these effects is attributed to the presence of Yb^{2+} from the growing process or to more probable thermally activated effects ($Yb^{3+} + e^- \rightarrow Yb^{2+}$) that generate non-radiative recombinations. [26] Another effect of the presence of Yb^{2+} ions is the distortion of lattice due to the discrepancy between the differently charged Yb ions: R_{Yb2+}=1.13 Å R_{Yb3+}= 0.98 Å. Emission characteristics of Yb^{3+} CT are strongly dependent on the local symmetry and are also influenced by the symmetry properties of the second coordination sphere. The thermal activated luminescence quenching is well evidenced in Figure 1.3.3, that reports the luminescence integrated intensity as a function of the sample temperature. A significant decrease of the PL signal is observed between 190 and 210 K. The inset clearly shows that the main shortening of the decay times is observed in the same 190-210 K range.

Figure 1.3.1 PL and PLE spectra at room temperature (288 K) of YbAP. The inset reports the decay time recorded for the 338 nm emission and the instrumental time response.

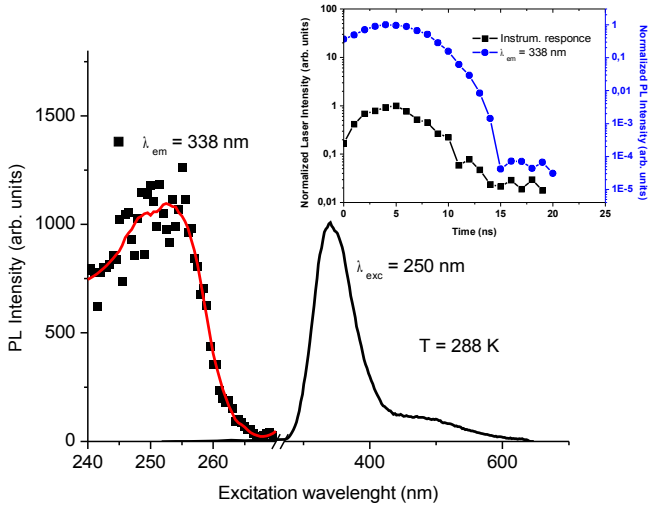

Figure 1.3.2 3D plot of the PL at different time delay from the excitation light at 10 K of YbAP. The inset shows the decay time of the emission at 338 nm.

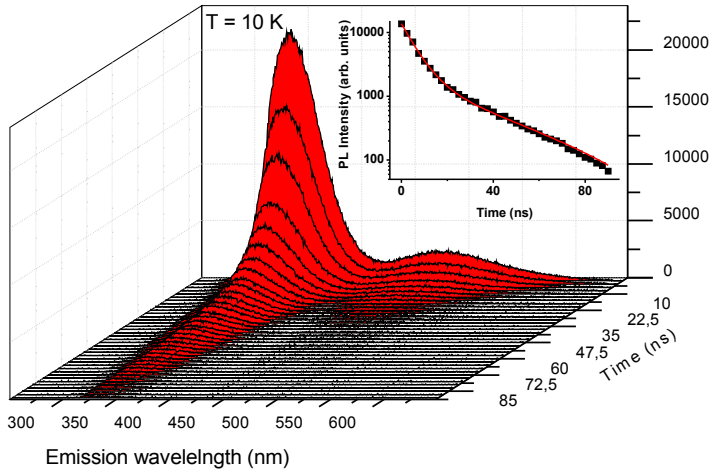

It is worth to note that in Yb:YAP the variation of the PL signal with temperature occurs in a wider temperature range (10-250 K).[27] Several authors observed pronounced quenching of ytterbium charge transfer luminescence with temperature in different matrices and it was previously assigned to non radiative energy transfer from the CT band to the 4f levels of ytterbium [28-31]. According to this attribution, we think that the shift to higher temperature of the CT quenching, which had been partially observed in previous works on Yb-doped perovskites at different concentrations, can be caused by the restricted relaxation of the charge transfer excited state due to decreasing volume of the elementary unit cell, which should increase the energy barrier for thermal quenching [25]. The elementary unit cell in pure YAP crystal is 210.85 $Å^3$ while in YbAP crystal, according to our calculations, should be 199.17 $Å^3$. The decrease in the volume of the unit cell is in agreement with the variations previously observed in the density of these perovskites, showing an increasing trend relative to the presence of Ytterbium over Yttrium, caused by the decreased ionic radius and increased atomic weight of the former over the latter (from 5.38 g/cm^3 (YAP) and going up to 6.64 g/cm^3 (Yb:YAP), to 8.2 g/cm^3 for YbAP) [26].

The optical properties of YbAP crystal could cause a growing interest for direct applications in the field of high energy physics if its scintillation efficiency resembles the characteristics previously observed in Yb:YAP. Nickl et al. reported that the total RL intensity of integrated emission spectra is monotonously increasing with the Yb concentration, reaching more than 11% of the BGO intensity for a 45%Yb-doped crystal at room temperature and rising up to 170% at 80 K [24]. Considering the higher efficiency and higher temperature quenching of the YbAP compound with respect to published data relative to Yb:YAP crystals, the results shown so far offer a a promising starting point for this new material, while a study focusing on the scintillation properties of YbAP crystal is still a mandatory task.

Figure 1.3.3 Integrated PL of YbAP at 338 nm *vs* temperature. The inset reports the decay time at different temperatures.

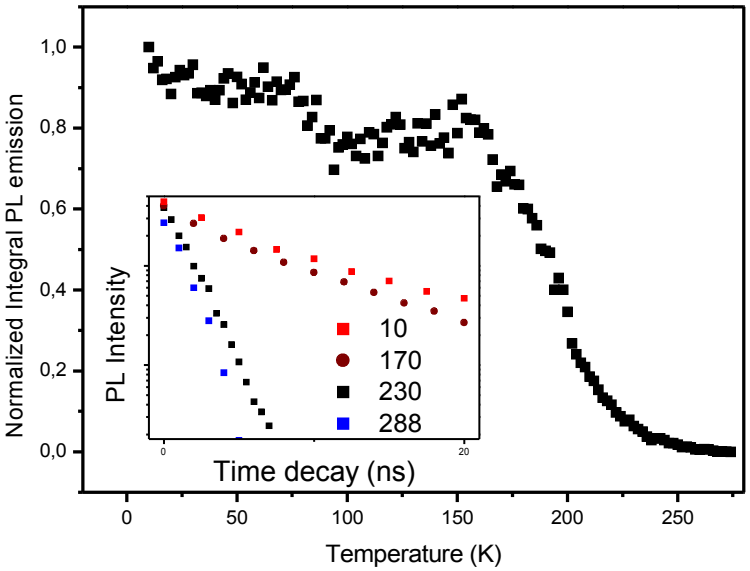

Conclusions

In this section different perovskite compounds featuring various chemical elements in the same crystalline site were analyzed from a structural point of view. The first step of the analysis for each compound was given by Raman spectroscopy, whose results permitted to point out the effective formation of perovskite structures and, on a more general note, to remark variations in the vibrational modes among the perovskite compounds in relation to the presence of different chemical elements.

Subsequent analyses were carried out along distinct paths depending on the results of interest for each material. In the case of LuAP, which hasn't been fully characterized from a structural point of view despite its relative oldness and its applications either by itself in various applications or as a basis for mixed compound such as LuYAP, the main scope was to obtain the missing structural characteristics. On the other hand, the case of YbAP was quite the opposite, as its absolute novelty meant the complete lack of data in literature. The main goal of the analysis was consequently moved towards finding the most interesting characteristics as scintillator, where Yb-based compounds are being proposed as an alternative to Ce-doped ones.

As a consequence, experimental techniques were chosen according to their capability of showing results of interest. In particular, EXAFS spectroscopy was used in order to obtain informations on the local structural characteristics of LuAP and on their variations with temperature, while photoluminescence measurements were performed on YbAP in order to obtain radiative time decays as a function of temperature. These results offer a first insight on this brand new material and permit to point it as a promising candidate for fast scintillation purposes.

REFERENCES

1. A. Lempicki, J. Glodo -- Nucl.Instr.andMeth.inPhys.Res.A416 **1998**, 333- 344.
2. P.D. Dernier – Mat. Res. Bull. Vol.6 **1971**, 430-440.
3. I.G. Valais – IEEE Trans. Nucl. Sci. **2008**, 55, 785.
4. J. H. Junga – Nucl. Instr. and Methods A 571 **2007**, 669.
5. W. Drozdowski – Nucl. Instr. and Methods A 562 **2006**, 254.
6. A. Wojtowicz – Phys. Condens. Matter 13 **2001**, 9599–961.
7. A.F. Wells – Structural Inorganic Chemsitry 5th edition **1984** (New York:Oxford Science).
8. U. Muller – Inorganic Structural Chemistry 2nd edition **2007** (New York:Wiley).
9. A. M. Glazer – Acta Cryst. B 28 **1972**, 3384.
10. R.W.G. Wychoff: *Crystal Structure;* (Krieger, Florida), **1986**.
11. J. Suda, O. Kamishima, K. Hamaoka, I. Matsubara, T.Hattori and T. Sato – J. Phys Soc. of Japan 72 **2003**, 1418.
12. A. Casu, P.C. Ricci, A. Anedda – J Raman Spectrosc 40/9 **2009**, 1224-1228.
13. B. A. Weinstein and R. Zallen in: Cardona, G. Gutherodta (Eds.), Light Scattering in Solids, vol. IV (Springer, Heidelberg) **1984**, 463-521.
14. M. N. Iliev, M. V. Abrashev, H.-G. Lee, V. N. Popov, Y. Y. Sun, C. Thomsen, R. L. Meng and C. W. Chu – Phys. Rev B 57 **1998**, 2872.
15. J. Mustre de Leon, J.J. Rehr, S.I. Zabinsky, R.C. Albers – Phys. Rev. B 44 **1991**, 4146.
16. P.D. Dernier – Mat. Res. Bull. Vol.6 **1971**, 430-440.
17. M. Kučera, K. Nitsch, M. Nikl, M. Hanuš and S. Daniš – J. Crystal Growth 312 **2010**, 1538.
18. C.M. Pepin, P. Berard, A.L. Perrot, C. Pepin, D.Houde, R. Lecomte, C.L.Melcher and H. Dautet – IEEE Trans. Nucl. Sci. 51 **2004**, 789.
19. P.Yang, P. Deng, Z. Yin – J. Luminescence 97 **2002**, 51.

20. S. Belogurov, G. Bressi, G. Carugno, M. Moszynski, W. Czarnacki, M. Kapusta, M. Szawlowski – Nucl. Instrum. Methods Phys. Res. A 496 **2003**, 385.
21. Y. Dong, G. Zhou, J. Xu, G. Zhao, F. Su, L. Su, G. Zhang, D. Zhang, H. Li, J. Si – J. Crystal Growth 289 **2006**, 676-680.
22. A. Denoyer, Y. Levesque, S. Jandl, Ph. Goldner, O. Guillot-Noel, B. Viana, F. Thibault, D. Pelenc – J. Luminescence 128 **2008**, 1389.
23. R. Lisiecki, W. Ryba-Romanowski, A. Speghini and M. Bettinelli – J. Luminescence 129 **2009**, 521.
24. M. Nikl, N. Solovieva, J. Pejchal, J. B. Shim, A. Yoshikawa, T. Fukuda, A. Vedda, M. Martini, and D. H. Yoon – Appl. Phys. Lett. 84 **2004**, 882.
25. J. Pejchal, M. Nikl, J. B. Shim, A. Yoshikawa, T. Fukuda, A. Voloshinovskii, V. Múčka, and D. H. Yoon – J. Appl. Phys 98 **2005**, 016104.
26. M. Nikl, A.Yoshikawa, T. Fukuda – Optical Materials 26 **2004**, 545–549.
27. M. Nikl, A. Yoshikawa, A. Vedda, T. Fukuda – J. Crystal Growth 292 **2006**, 416–421.
28. E. Nakazawa J.Lumin. 18/19 **1979**, 272–276.
29. L. Van PietersonL, M. Heeroma, E. deHeer and A. Meijerink – J.Lumin. 91 **2000**, 177.
30. I.A. Kamenskikh, N. Guerassimova, C. Dujardin, N. Garnier G. Ledoux, C. Pedrini, M. Kirm, A. Petrosyan, D. Spassky – Optical Materials 24 **2003**, 267.
31. I. Kamenskikh, C. Pedrini, A. Petrosyan, A. Vasil'ev – J. Lumin. 29 **2009**, 1509.

Section 2

This section revolves around two different structural studies on the effects of doping in a crystal matrix. In particular, a first part is pointed towards analyzing structural variations caused by heavy yttrium doping in a lutetium aluminum perovskite, while the second part deals with the analysis of an extremely low iron doping in a yttrium aluminum garnet matrix. Apart from the actual results obtained in each study, the choice of two extreme cases of doping in different materials for scintillation should be intended also on a more general note as a means to remark once again the importance of knowing the strong and weak points of the experimental techniques when looking for specific experimental results. In particular for the cases presented here this means looking for techniques with the capability of discerning the presence of very diverse percentages of dopant. Moreover, structural variations in the cell parameters should be expected in the case of heavy yttrium doping in a lutetium aluminum perovskite matrix, while such effects are expected to be negligible in the case of an extremely low iron doping of a yttrium aluminum garnet matrix. However, in the latter case the structure of the host matrix permits two different substitution sites for the dopant element, thus the technique of choice should be able to give informations on its actual behavior. In this framework the analysis of photoluminescence spectra through Zero Phonon Line theory allows a discernment from an energetic point of view of the possible occupancy of crystalline sites by the dopant, while EXAFS spectroscopy can be chosen as a way of measuring the structural characteristics of $Lu_{0,7}Y_{0,3}AlO_3$ crystals in comparison with pure yttrium and lutetium perovskites.

2.1 The role of yttrium doping in a lutetium aluminum perovskite matrix (LuYAP)

LuYAP is a promising compound in the family of Ce-doped materials thanks to its interesting

characteristics. Its peculiarity of being a mixed compound of two perovskite crystals permits to keep the strong points of the pure compounds, namely high density (which will be comprised between 5.38 $g/cm^{3\ of}$ $YAlO_3$ and 8.34 g/cm^3 of $LuAlO_3$) and fast decay time (comprised between 25 ns for $YAlO_3$ and 17 ns for $LuAlO_3$), while diminishing their drawbacks, such as the difficulties encountered in the growth procedures (the presence of yttrium causes an increase in the viscosity of the melt, along with a decrease of the fusion temperature). While these characteristics already allow to hint at its possible application as a fast scintillator, no attention was given towards comprehending more precisely the variations caused on the LuAP structure by the presence of yttrium. In this perspective a comparison between polarized Raman spectra of LuYAP and LuAP monocrystals can offer a hint on possible decreases in crystalline order of the mixed compound in respect to the pure crystal. The analysis points out a broadening and a decrease in intensity of the corresponding low-wavenumber vibrational peaks, such as the 119 cm^{-1} peak of the A_{1g} vibrational modes in LuAP and to its homologous in LuYAP (the broad peak centered around 123 cm^{-1}) which are highlighted in Figure **2.1.1**. According to literature these peaks are related to vibrations of the A site [1,2,3]: the first peak of the LuYAP spectrum was consequently fitted as a convolution of the corresponding low-wavenumber modes of LuAP (119 cm^{-1} and 157 cm^{-1}) and YAP (144 cm^{-1}), as shown in the inset of Figure **2.1.1**. The results of the fitting process hint at the presence of overlapped lutetium- and yttrium-related vibrational modes in the Raman spectrum, while the broadening of the peaks hints at a possible variation in the short range crystalline order of the mixed compound with respect to the pure ones, featuring a population of solely yttrium or lutetium in the A crystal site. As a consequence, it is possible to hypothesize that the presence of yttrium in the formation of the LuYAP single crystals lowers the local order of the structure.

In order to gain actual evidence on the role of yttrium in the formation of LuYAP crystals, EXAFS measurements were performed at the K absorption edge of yttrium (17038 eV) and at the L_3 edge of

lutetium (9244 eV) for YAP, LuAP and LuYAP crystals. The mixed occupation by lutetium and yttrium in the A site of the LuYAP crystal offers a useful means of comparison with both LuAP and YAP crystal structures from a local point of view. Fitting of the EXAFS spectra collected at both absorption edges allows to check the correspondence among the nearest and next-nearest neighbors for each absorbing center, thus showing how the presence of yttrium ions affects the formation of the crystal.

In order to achieve these results, the first step of each round of fitting was to analyze the spectra of undoped perovskite crystals (YAP e LuAP) in the region containing the unit cell. A good fit of these crystals points out the good agreement between theoretical models and the actual crystals, thus confirming the effective formation of the perovskite structure and, on the other hand, justifies their use as a reference for the fitting processes involving their mixed compound, LuYAP (Table 2.1.1).

Consequently, comparative fitting procedures were carried out in the mixed crystal oxides, where the contemporary presence of yttrium and lutetium was possible. Contributions due to the presence of yttrium were accounted for in different ways depending on the absorption edge of choice. With Lu as the absorption center, yttrium doping was introduced in the theoretical model as a possible neighbor against lutetium. In the case of absorption by Y, the possible results of yttrium doping were taken into account by considering two different Y-centered theoretical cells (YAP and LuAP), the second one being a perturbative contribution of sorts, introduced to clarify whether the doping led to the formation of YAP clusters or resulted in the sole substitution of the chemical element present in the lanthanide site of an overall rigid LuAP structure . In both cases amplitude reduction terms were associated to opposite structures related to the presence of lutetium over yttrium. The values obtained by the fitting processes were used as indicators of the presence of one chemical element and/or structure over the other: such “quantitative” calculations were always carried out so that the sum of amplitude reduction factors was in accordance with the general one relative to all the remaining scattering paths in each fitting process and with the results of pure crystals, as shown in Table 2.1.1.

Figure 2.1.1 Polarized Raman A_{1g} modes of LuAP and LuYAP. Yellow arrows show the corresponding broadened peaks. The deconvolution of the first LuYAP peak, showing contributions from lutetium and yttrium, is shown in the inset.

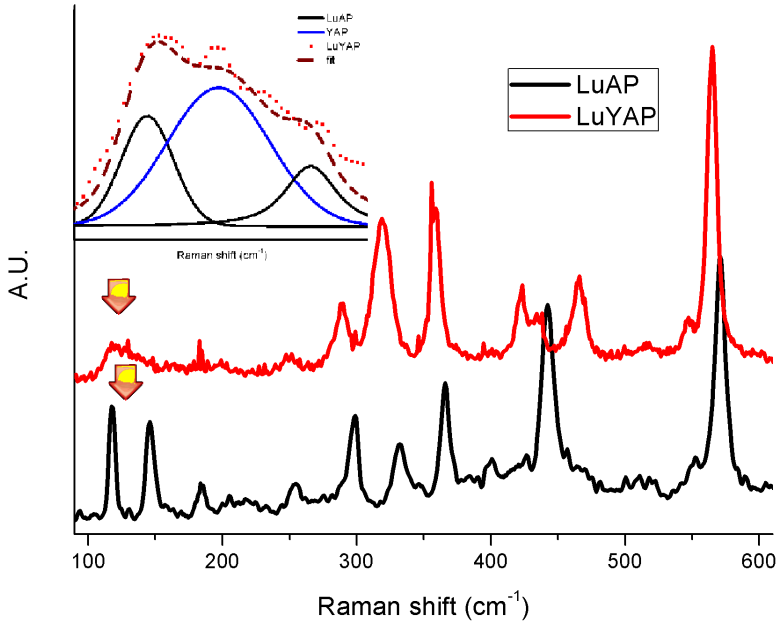

Table 2.1.1 Main results of the best fitting curves of the EXAFS data.(A) and (B) of S^2_0 column of the Y K-edge of LuYAP indicate the two possible cells of different size formed around yttrium atoms. R factor indicates misfit between theory and data, while S^2_0 indicates the amplitude reduction term.

	YAP (Y K edge)		**LuAP (Lu L_3 edge)**		**LuYAP (Lu L_3 edge)**		**LuYAP (Y K edge)**		
R factor	0.020 +/-0.005		0.013+/-0.003		0.016+/-0.005		0.019+/-0.006		
S^2_0	0.901+/-0.067		1.001+/-0.008		1.000+/-0.007		0.683 +/-0.050(A)		0.349 +/-0.045(B)
	R	σ^2	R	σ^2	R	σ^2	R (A)	R (B)	σ^2
Path 1:[O1_1]	2.286	0.003 (1)	2.220	0.005 (2)	2.224	0.005 (2)	2.232	2.198	0.003 (1)
Path 2:[O2_1]	2.252	0.003 (1)	2.186	0.005 (2)	2.193	0.005 (2)	2.260	2.260	0.003 (1)
Path 3:[O1_2]	2.350	0.003 (1)	2.313	0.005 (2)	2.313	0.005 (2)	2.295	2.287	0.003 (1)
Path 4:[O2_2]	2.440	0.007 (3)	2.450	0.014 (3)	2.450	0.014 (3)	2.450	2.420	0.006 (1)
Path 5:[O2_3]	2.542	0.007 (3)	2.545	0.014 (3)	2.546	0.014 (3)	2.549	2.516	0.006 (1)
Path 6:[O1_3]	3.034	0.007 (3)	2.943	0.014 (3)	2.942	0.014 (3)	2.964	2.909	0.003 (1)
Path 7:[Al1_1]	3.044	0.002 (1)	3.038	0.007 (2)	3.034	0.011 (3)	3.017	3.009	0.003 (1)
Path 8:[O1_4]	3.153	0.002 (1)	3.108	0.007 (2)	3.131	0.011 (3)	3.079	3.073	0.003 (1)
Path 9:[Al1_2]	3.175	0.002 (1)	3.135	0.007 (2)	3.108	0.011 (3)	3.147	3.106	0.004 (1)
Path 10:[Al1_3]	3.276	0.002 (1)	3.234	0.007 (2)	3.231	0.003 (2)	3.247	3.203	0.004 (1)
Path 11:[O2_4]	3.227	0.002 (1)	3.076	0.007 (2)	3.124	0.003 (2)	3.236	3.180	0.004 (1)
Path 12:[Al1_4]	3.513	0.002 (1)	3.506	0.007 (2)	3.502	0.003 (2)	3.483	3.473	0.004 (1)

Fitting of the absorption spectra collected at the L_3 absorption edge of lutetium for the LuYAP sample was carried out starting from the LuAP formula unit. The presence of yttrium doping was taken into account theoretically as equally possible in all the lanthanide sites considered in the fit. Obviously variations in cell dimensions are expected with respect to the LuAP model due to the variation in radius between yttrium and lutetium, thus they are likely to appear independently on the decrease of bonding distances due to thermal shrinking.

Actually, the results of the round of fitting performed on LuAP and LuYAP (Figure 2.1.2) show a strong similarity between the structural parameters of the respective best fits, with a slight increase in the scattering distances of LuYAP which leads to an expansion of the cell dimensions. These results prove the likeness of the structures from the local point of view of lutetium as absorbing center (Table 2.1.1). However, the fitting results offer a first important glimpse on the role of yttrium as a dopant by looking at the amplification factors of Lu-Y single-scattering paths of the best fitting curves. Bearing in mind the possibility of discerning between the four lanthanide sites in the horizontal plane and the two along the Z axis due to the different radial distances, it is possible to observe an anisotropy in the amplitude reduction terms. Yttrium single scattering paths give a minority contribution with respect to lutetium ones: this division is more evident looking at the amplitude reduction therms along the Z axis, whose value is lower than the ones of paths in the horizontal plane (Table2.1.2). This fact suggests an inhomogeneous distribution of dopants that could be put in relation with the inhomogeneity in unit cell dimensions.

The second round of fitting was performed on the absorption spectra of pure yttrium perovskite (YAP) and $Lu_{0.7}Y_{0.3}AlO_3$ (LuYAP) collected at the yttrium K edge (Figure 2.1.3). Once again the analysis of pure yttrium perovskite was used both as a starting point for the fitting procedure of the mixed perovskite and as a reference for the results of the latter fitting. Yttrium is now the absorbing element, so the best fitting curve should give structural informations on the LuYAP cell formed around the

Figure 2.1.2 R-space EXAFS data (in black for magnitude and in blue for imaginary component) and best fitting curves (in red for magnitude and in green for imaginary component) of LuAP (left) and LuYAP (right) at the L_3 absorption edge of lutetium (9244 eV). K-space data are shown in the insets.

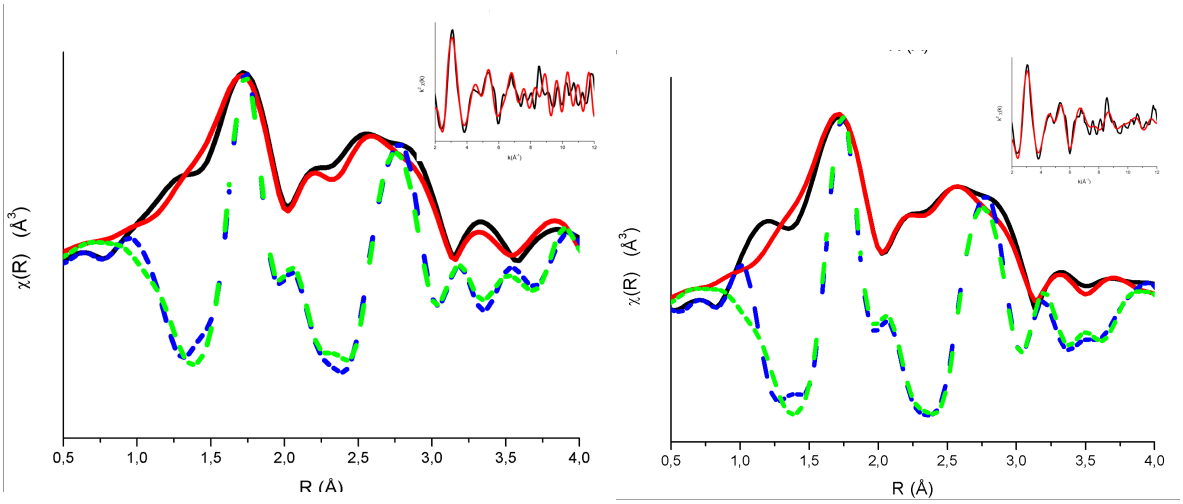

Figure 2.1.3 R-space EXAFS data (in black for magnitude and in blue for imaginary component) and best fitting curves (in red for magnitude and in green for imaginary component) of YAP (left) and LuYAP (below) at the K absorption edge of yttrium (17038 eV). K-space data are shown in the insets.

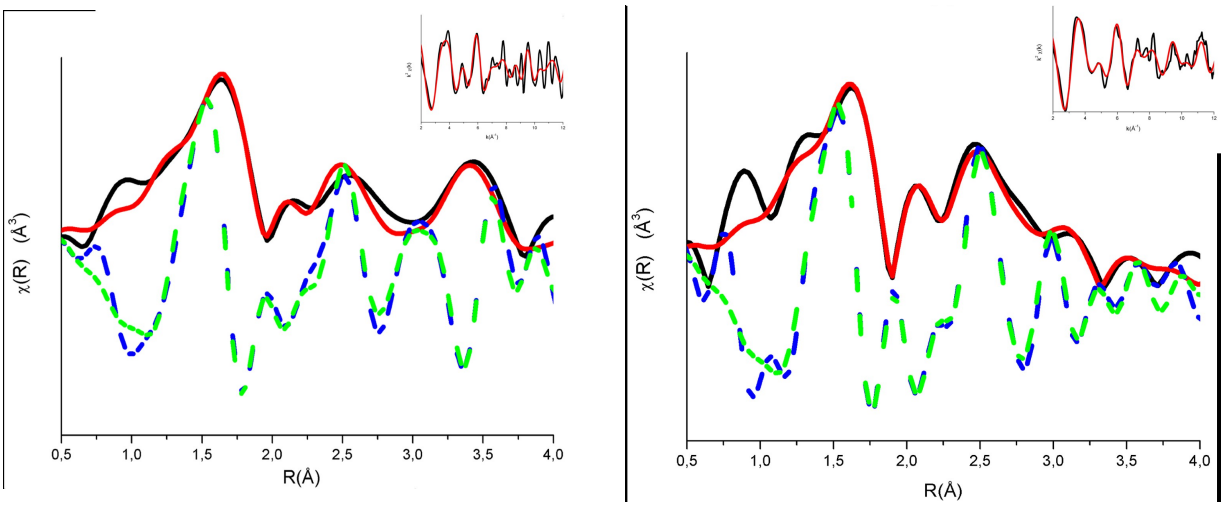

dopant. As previously stated, two possible theoretical models were used as a starting point for the fit of the cell (a bigger so-called “YAP-like” cell and smaller “LuAP-like” cells) in order to observe the actual structures formed around the absorbing yttrium , while the doping of lanthanide neighbors in the third shell was taken into account analogously to the previous round of fit. The results obtained by the fitting procedure show once again an interesting new insight, since neither of the two proposed cells was able to accomplish a good fit of the experimental data, while the best fitting curve features a combination of both. The distances between the absorption site and the other atoms of both the cells, obtained from single scattering paths, are in good agreement with each other and with the previous results. This first result shows that neither of the cells formed around the yttrium sites cant be appointed to any of the pure compounds but are comprised between those of pure LuAP and those of pure YAP. Given an overall value of 1 for the sum of all amplitude reduction terms as the totality of yttrium present in the sample, values of 0.68 for the YAP cell and 0.35 for the LuAP cell hint at the fact that cells formed around yttrium sites have intermediate characteristics between LuAP and YAP cells, but are also affected by local characteristics in a way that determines possible distortions in their structure (Table 2.1.1). Once again the presence of yttrium doping in the lanthanide sites of the third shell can be deduced from the values of amplitude reduction terms of Lu over Y in the best fitting curve. Lutetium still seems to be the most common neighbor against yttrium but, in opposition with the results obtained during the first round of measurements, the presence of yttrium in the two sites along the Z axis is lower but still consistent with the results obtained by the single-scattering paths along in the XY plane (Table 2.1.2).

A comparative analysis of the results obtained by best fitting curves for the two studied absorption edges of LuYAP seems to acknowledge that the yttrium doping is effectively dispersed among the whole extension of the crystal without the formation of YAP clusters (whose presence would require

zones where yttrium neighbors are locally prevalent over lutetium). Moreover, the similar values of Lu/Y presence as next-nearest neighbor along the XY plane along with the strong decrease in the presence of yttrium along the Z axis in the case of lutetium L_3-edge absorption allow to hypothesize the distribution of yttrium dopant in a series of non-consecutive horizontal planes with a dotted-stripe-like distributions along the Z axis of the crystal (Figure 2.1.4): this model fulfills both the condition of the inhomogeneous yttrium distribution as nearest neighbor of lutetium along the Z axis in respect to X and Y axes (as shown by the variations in the fitting results of the lanthanide ions along the Z axis in the lutetium L_3-edge data in respect to the yttrium K edge data) and the presence of yttrium as less common nearest neighbor of yttrium itself mainly along the horizontal axes of the crystal (as hinted by the overall presence of lutetium as main nearest-neighbors from the results of both fitting processes).

On a different note, the fitting results permit to calculate the volume of the cells from the distances between the absorbing centers and the neighbor atoms for the A crystal sites (lutetium and/or yttrium, respectively) with simple geometric calculations. Using YAP as a comparison and confronting the volume obtained by literature data for YAP (203,5 $Å^3$) with the one obtained by the results of the YAP fit (203,0 $Å^3$) it's possible to observe a perfect accordance between data. Looking at the data obtained by fitting results for all the previously mentioned perovskites, cell volumes can be also calculated for LuYAP (188,2 $Å^3$ (K edge of yttrium) and 185,8 $Å^3$ (L III edge of lutetium)) and LuAP (182,2 $Å^3$). It's possible to mark that cell volumes decrease with the presence of lutetium, as can be expected from the difference in radius between yttrium and lutetium. The variation in cell volumes of LuYAP depending on the the absorbing element hints at the decrease in short range crystalline order previously shown by Raman spectra. These results once again lead to hypothesize the goodness of the results obtained by the fitting procedures and hint at the crystal structures of different volume formed by the presence of lutetium and yttrium as the cause of the decreased crystalline order of LuYAP .

Figure 2.1.4 Sketch of the distribution of yttrium atoms (yellow spheres) in the crystal matrix. Lutetium atoms are indicated as blue spheres.

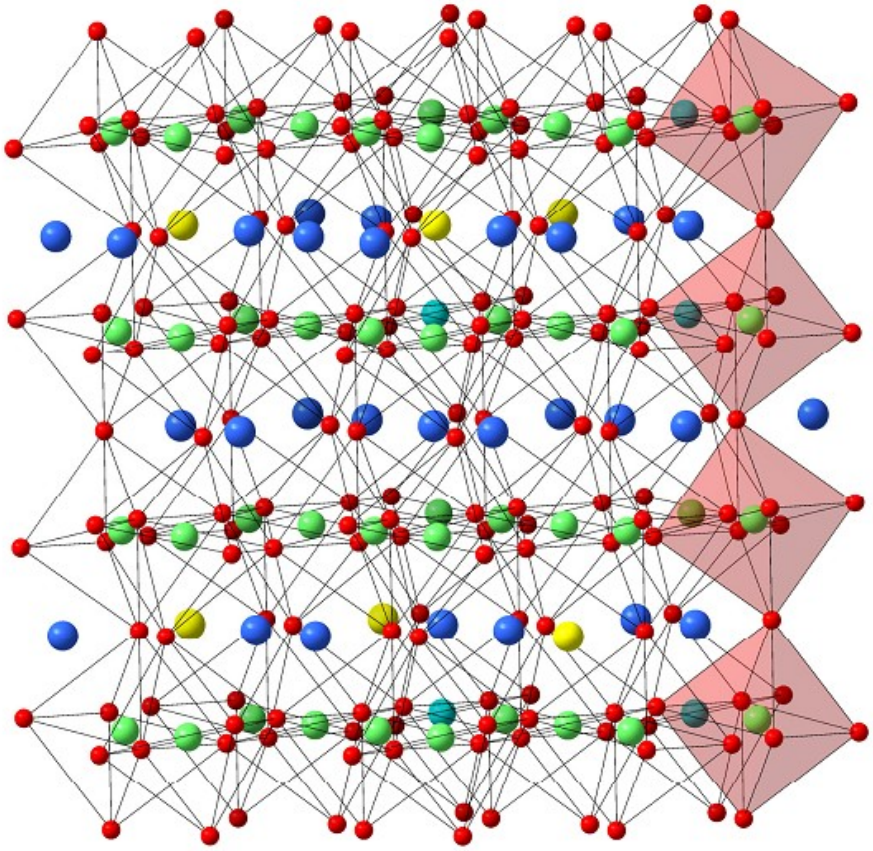

Table 2.1.2 Single scattering path distances from the best fitting curves of EXAFS data. The last line reports the volumes of cells calculated from fitting data.

	YAP (Y K edge)		LuAP (Lu L_3 edge)		**LuYAP (Lu L_3 edge)**		**LuYAP (Y K edge)**	
	S^2_0	R	S^2_0	R	S^2_0	R	S^2_0	R
x-Lu1_1	0.901+/-0.127	-	1.001+/-0.008	3.475	0.509+/-0.076	3.544	0.541+/-0.011	3.528
x-Y1_1	0.901+/-0.127	3.625	1.001+/-0.008	-	0.490+/-0.076	3.524	0.490+/-0.011	3.486
x-Lu1_2	0.901+/-0.127	-	1.001+/-0.008	3.621	0.917+/-0.076	3.630	0.604+/-0.12	3.614
x-Y1_2	0.901+/-0.127	3.735	1.001+/-0.008	-	0.080+/-0.076	3.620	0.437+/-0.12	3.571
x-Lu1_3	0.901+/-0.127	-	1.001+/-0.008	3.699	0.509+/-0.076	3.707	0.541+/-0.011	3.691
x-Y1_3	0.901+/-0.127	3.797	1.001+/-0.008	-	0.490+/-0.076	3.691	0.490+/-0.011	3.65

However, despite the results obtained thus far and the possibilities given by a local analysis centered on a chemical element of choice (i.e. the doping element), EXFAS spectroscopy cannot always be pointed out as the technique of choice for similar structural studies. A good example of this fact is given by the case of the low percentage iron doping in a yttrium aluminum garnet matrix, where the possible sites of doping by substitution for iron are two aluminum sites of different point symmetry.

2.2 The role of iron doping in a yttrium aluminum garnet matrix

Fe:YAG is a well known doped crystal and the contribution of the dopant to the performance of the host matrix has been an important field of research unto itself and in reference to YIG, where the Fe ion is part of the matrix instead of a dopant [4-6]. The studies on electron-phonon coupling (EPC) of Fe^{3+} ions in a YAG matrix have been an important field of research in past years in order to optimize the comprehension and the knowledge of various aspects such as the structure of energy levels and the role of optical centers in energy transfers for materials of interest in the fields of solid state lasers [5,7]. The YAG crystal ($Y_2Al_5O_{12}$) (space group Ia3d=O_h^{10}) features Al^{3+} ions coordinated to nearest-neighboring oxygens with octahedral and tetrahedral point symmetry. The iron acts as substitutional dopant for aluminum ions in the a and d sites with point symmetry G(a)=C_{3i} and G(d)=S_4, with octahedral and tetrahedral oxygen coordination, respectively. The larger radius of Fe^{3+} in comparison with that of Al^{3+} ion causes a variation in the local lattice structure and, consequently, an expansion/distortion effect [4,8]. The main goal of this study is to obtain a full and unequivocal attribution of the transitions related to Zero Phonon Line (ZPL) through the study of the ZPL itself and of the vibronic sideband of Fe^{3+} doped YAG crystal, since these results are still missing despite the amount of literature dedicated to the study and the analysis of the EPC.

Photoluminescence spectra of Fe:YAG crystals were recorded in two different rounds of measures, both collected with different temperatures and each one intended to enhance different aspects of the acquired data. The first round of measurements took place at the SUPERLUMI experimental station on the I beamline of the Hasylab synchrotron laboratories at DESY in Hamburg and allowed the collection of the whole luminescence spectra, thus taking into account the full vibronic sideband, although the observed ZPL didn't seem to be fully resolved. On the other hand the second round of measurements, operated with an Ar laser as excitation source, was devoted to obtaining high resolution ZPL curves.

The Fe:YAG samples are commercial crystals grown by Czochralski method, featuring a percentage of Fe doping of few ppm. The choice of such low quantity of dopant in the host matrix should be intended as a way of avoiding Fe-Fe interactions in favor of Fe-host interactions.

The spectra were recorded on the basis of two different physical processes: the first set of measurements featured direct excitation of the host matrix with energy close to the band gap energy (at 6.88 eV), while measurements during the second set were performed with selective excitation of the Fe ions (whose absorption maxima are 3.04, 2.98, 2.70 and 2.62 eV) [9].

Figure 2.2.1 shows a PL spectrum recorded at 10 K. While the ZP line can be observed around 13100 cm^{-1} (1.626 eV), the 12797.1 – 12766.1 cm^{-1} (1.588-1.584 eV) spectral range features the most complex structure of the spectrum, where the main system of the phonon repetition is reported: these bands derive from the transitions between the $^4T_1 \rightarrow {}^6A_1$ levels of Fe^{3+} ions[7, 9, 10]. No difference can be observed in the luminescence spectra from Fe ions dispersed in YAG crystals among the two set of excitation energy and for sake of clarity only the spectra at 10 K corresponding to an excitation of 6.88 eV and at 2.70 eV are reported in figure 2.2.1. The inset of Figure 2.2.1 shows a high resolution spectrum recorded at 10 K: the image highlights the result of resolving two ZP lines at 13099.2 cm^{-1} (1.626 eV) (ZPL1) and 13109.9 cm^{-1} (1.627 eV)(ZPL2), both featuring half-widths of less than 3 cm^{-1}, which improve the previous experimental results [7]. It is worth noting that ZPL1 features a quasi

Figure 2.2.1 Photoluminescence spectra of Fe^{3+} ions in YAG crystal recorded at 10 K with excitation energy of 6.88 eV and 2.70 eV. The inset reports the high resolution spectrum recorded at 10 K (excitation 2.70 eV) focused on the ZPL spectral region.

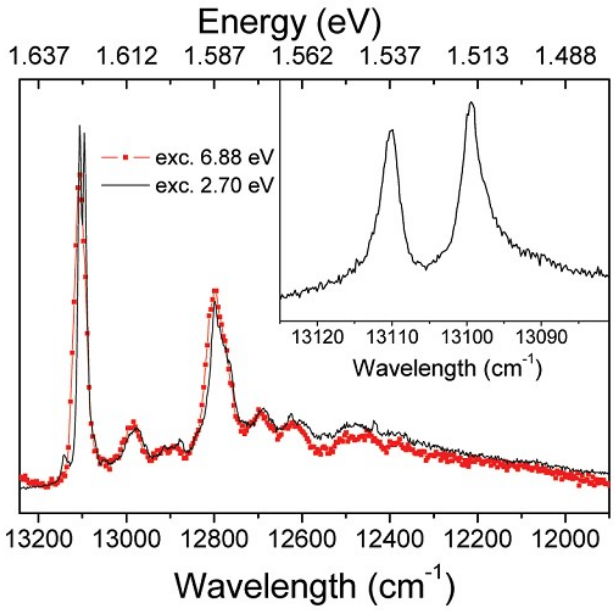

Figure 2.2.2 Photoluminescence spectra of Fe:YAG crystals as a function of sample temperatures. The inset reports the high resolution spectrum (excitation 2.70 eV) focused on the ZPL spectral region, showing four ZPLs.

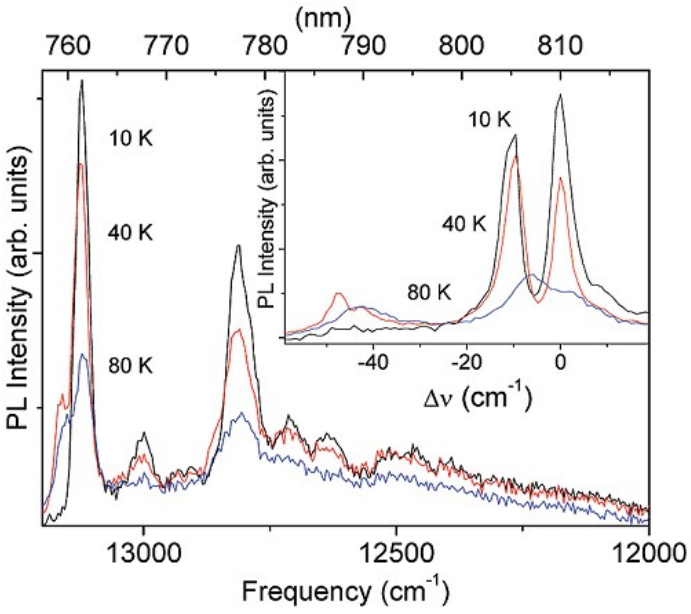

Lorentzian peak profile with a slight asymmetry in the low energy region, which could be ascribed to quadratic electron-phonon coupling [11].

Figure 2.2.2 shows the emission spectra in the range between 12000 and 13200 cm^{-1} detected at different temperatures of the sample. Once again, the main part of the figure is devoted to show the variations in the characteristics of the overall spectra with different temperatures as observed by high energy excitation of the host matrix, while the inset is focused on the variations observed in the ZP lines from high resolution spectra of selective Fe sites excitation. Here the 0 value in the X axis was chosen in order to clearly show the line shift. First of all it's clearly observable a different variation in intensity for ZPL2 and ZPL1, so that the ratio ZPL2/ZPL1 increases proportionally with the temperature and grows to a value higher than 1 already at 40 K. Besides, in the 40 K spectrum it's possible to observe the growth of a third hot line at 13144 cm^{-1} (1.631 eV) (ZPL3) that seems to split in two components whose half-width, larger than the ones of ZPL1 and ZPL2, allows to distinguish among them by only using two-Voigt profile fitting curves. The observation of fours fine structure components of the $^4T_1(G)$ emission term in the luminescence spectrum allows to determine the nature of the crystal field of the environment of the Fe^{3+} ions in the matrix by discriminating the coordination symmetry of the lattice position. Hence the initial state of the emission degenerate at least in four components. The upper states are separated by 48 cm^{-1} from the lowest excited state.

If we look at the variations in the four ZPL components proportionally to the increase of temperature, three different processes can be pointed out. First of all, the intensity of the ZP lines decreases with the rising temperature, in conjunction with the enhancement of the phononic transition represented in the sideband, along with a broadening of the ZP lines and a shift towards lower energy. The temperature redshift observed in the ZP lines indicates the dominant role of electron-phonon interactions by comparison with thermal expansion of the lattice, which would have determined a blue-shift[12, 13].

The rise in temperature causes a decrease in the lifetime of the excited state of ZP transition, thus broadening the ZP lines, whose FWHM is inversely proportional to the aforementioned lifetime. Since the ZPL features both a Gaussian and a Lorentzian term, caused respectively by physical processes of random or equiprobable occurrence for each atom, the broadening of the lines must be considered as a Voigt-type process where the relative weight of the two components hints to the physical phenomena happening for each ZP line. It's clear to see a variation in the dependence of each ZP line on temperature in terms of intensity and peak shift: in particular, the lowest energy peak features a higher dependence on temperature in terms of intensity and peak shift. The practical consequence of the simultaneous broadening and shifting of the peaks is that the main peaks overlap around 80 K of temperature, thus preventing from physically deconvolving them for higher temperatures. The dependence on temperature of the coupling with optical phonons is also present, although its overall role is drastically reduced in respect to the ZP lines.

2.2.1 Results and discussions

The garnet crystals offer two sites for the transition ions, the octahedral a-site (of local C_{3i} symmetry) and the tetrahedral d-site (S_4), the preference for substitution being determined by the mismatch of ionic radii of the dopant and host cation and on the electronic structure of the former. The d-sites show a better packing around the dodecahedral c-site (D_2 symmetry) occupied by the rare-earth ions and the minimal d-c distance is shorter than the octahedral a-c distance [10-14]. The lowest spectral term of the ground electronic configuration $3d^5$ of Fe^{3+} is a spin sextet ^6S while the excited states are spin quartets or doublets. This leads to the prohibition of transitions between the ground and excited states, however the spin-orbit mixing of the sextet and quartet spin states increases the probability for sextet to quartet transitions: the corresponding levels are split by the cubic component of the crystal field according to the rules $^6S \rightarrow {}^6A_1$, $^4P \rightarrow {}^4T_1$, $^4D \rightarrow {}^4E+{}^4T_2$, $^4F \rightarrow {}^4A_2 + {}^4T_1+{}^4T_2$, $^4G \rightarrow {}^4A_1+{}^4E+{}^4T_1+{}^4T_2$ and the Tanabe-

Sugano diagram, or the position of the crystal field levels as function of the crystal field strength, is similar for octahedral and tetrahedral coordination [15].

The crystal-field strength Dq is generally at least twice greater for octahedrally coordinated ions in respect to tetrahedrally coordinated ions and, therefore, the $^4T_{1g}(^4G)$ and $^4T_{2g}(^4G)$ states will occur at lower energies than the $^4T_1(^4G)$ and $^4T_2(^4G)$ levels. In opposition with tetrahedral sites, transitions to octahedral states should also be distinguishable on intensity grounds since the octahedral (or 3) symmetry causes transitions between $^6A_{1g}(^6S)$ and any of the 4G manifold to be parity forbidden. The lack of inversion at the tetrahedral site allows static mixing of higher energy, high intensity, odd parity transitions into the ground state. Consequently, transitions between the $^6A_1(^6S)$ ground state and the quartet excited states, being only spin forbidden, should exhibit higher intensity than those between $^6A_{1g}(^6S)$ to the excited quartet levels. Thus in case of the isolated Fe^{3+} centers in diluted garnets the optical spectra will be dominated by the tetrahedral centers.

Figure 2.2.3 shows the crystal-field states of a $3d^5$ electron configuration in a tetrahedral environment as it applies to the Fe^{3+} ion YAG crystal. The $^6A_1$ ground state of Fe^{3+} ($L = 0$, $S = \frac{5}{2}$) is split into two states (Γ_8 and Γ_7) which are separated by less than 1 cm^{-1} (Not resolved) [16]. The ^4G first excited state splits by the T_d crystal field into four sublevels, where the lowest state is a $^4T_1$ level. In Figure 2.2.3 the higher excited states of the Fe^{3+} ion in a tetrahedral crystal field are also represented schematically. Additional spin-orbit coupling furtherly splits the $^4T_1$ state into four sublevels Γ_6, Γ_8, Γ_7, and Γ_8. According to crystal-field theory the states are separated by about 100 cm^{-1}, However, according to Koidl a dynamic Jahn-Teller effect can drastically reduce the pure crystal-field splitting of the $^4T_1$ states[17]. In the static limit the four sublevels coincide in pairs [(Γ_8, T_7) and (Γ_6,Γ_8)]. Several $3d^5$ systems showing this behaviour where the static Jahn-Teller limit is achieved are presented in the literature [18, 19].

Figure 2.2.3 Level Scheme of Fe^{3+} ion in a tetrahedral crystal field starting from the ^4G first excited state. The $^6A_1$ fundamental state is split into two additional states not resolved. The observed ZP transitions (ZPL1, ZPL2, ZPL3 and ZPL4) from the spin orbit coupling four sublevels of the $^4T_1$ were indicated, as well as their spacing from the fundamental transition.

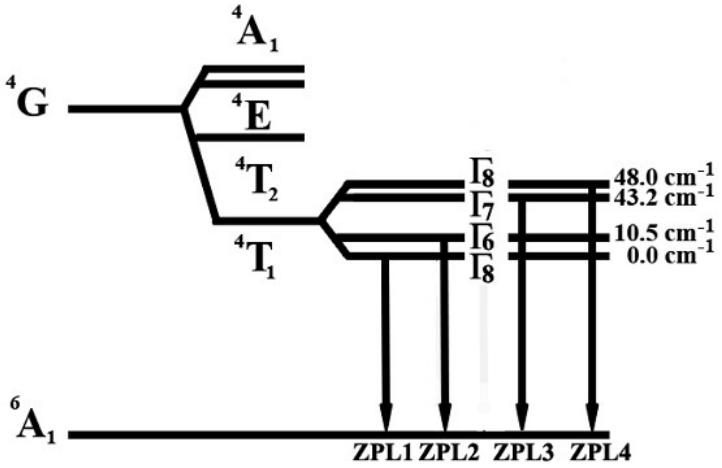

The relatively strong and structured phonon replica and the fine structure of the ZP line reported in figure 2.2.1 and 2.2.2 gives evidence of a Jahn-Teller effect in the 13100 cm^{-1} emission. For the present case, as can be observed in figure 2.2.2, the $^4T_1$ state is split into four states, where the upper excited states are separated by 48.0, 43.2 and 10.5 cm^{-1} from the lowest $^4T_1$ level, respectively (Inset of Figure 2.2.2 and figure 2.2.3). From these experimental results it is possible to affirm that the Jahn-Teller distortion does not reach the static limit for Fe^{3+} ion in YAG crystals.

As previously pointed out in figure 2.2.1, the ZP lines show a strong and structured phonon sideband, which consists on the one hand of broad bands due to coupling to lattice phonons and on the other hand of sharp lines due to coupling to defect-specific vibrational gap modes and vibrational resonant modes. Besides the weak band at 25 cm^{-1} that can be attributed to the coupling to acoustic modes, the peaks observed in the vibronic part of the spectrum can be assigned to the coupling to optical (TO and LO) lattice phonons. The band at 12993.3 cm^{-1} can be assigned to the overlapped contributions from 119 cm^{-1} and 125 cm^{-1} optical modes (TO and LO respectively). Other vibronics that can be assigned to the coupling with optical phonons can be revealed at 12921.1 cm^{-1} and 12884.5 cm^{-1} relative to the TO and LO modes centered at 181 (LO) and 218 cm^{-1} (TO).[20]

The strongest coupling occurs for LO-type modes, and the most intense peak at 12803.7cm^{-1} has a energy distance of 298 cm^{-1} from ZPL1, coincident with the value of the LO modes derived by Hurrell at al..[20] Moreover, according to Papagelis et al.[21] the phonon density of states for garnet structures presents the maximum at about 300 cm^{-1}. For higher frequencies the phonon density drops to zero, which means that following the Debye model it is possible to define the phonon cut-off frequency to 298 cm^{-1}.

In the range between 12430 and 12460 cm^{-1} we observe the coupling of the ZP lines to a series of very sharp phonons. These peaks reveal small half-widths (about 2 cm^{-1}) in respect to the phonon modes and different excitation spectra between them: the band at 12435.1 cm^{-1} is always present in all the excitation spectra explored (6.88-2.40 eV), while the pair at 12462.1 and at 12456.9 cm^{-1} presents very sharp excitation spectra (2.72-2.66 eV) peaked at 2.69 eV in coincidence with the $^6A_1 \rightarrow {}^2T_2$ transition with a temperature dependent behaviour. [22] The first of these peak can be attributed to Iron-defect specific modes, while the twin peaks to Zero phonon recombination from $^2T_2$ to the first excited state $^4T_1$.

Different information on the coupling parameters of iron ions dispersed in the YAG crystal can be achieved from the study of the luminescence spectra in the 13050 – 13200 cm^{-1} spectral range as a function of temperature (figure 2.2.2).

The behaviour of the ZPL, intensity, line width and asymmetric line shape are temperature dependent for systems having both linear and considerable quadratic interaction terms.

In the linear approximation of phonon coupling interactions, at T = 0 K and k = 0, phonons are not involved in the transition and only the n = 0 vibrational state is occupied; the ZPL has the intensity[12]

$$I_{k=0}\left(T_{0K}, E\right) \propto e^{-S}\delta\left(\Delta E - E\right) \qquad (2.2.1)$$

where $\Delta E_{.}$, is the energy of the zero phonon transition.

Besides the Zero phonon line, there are also transitions that correspond to a change in phonon state of the lattice ($k \neq 0$). These multi-phonon transitions will lead to the appearance of the broad phonon sideband, bounded to the ZPL in the low temperature limit through the Huang-Rhys parameter S

$$\frac{I_1}{I_2} \cong e^{-S} \qquad (2.2.2)$$

Where I_1 and I_2 are the integrated Area of the ZPL and multiphonon transition, respectively.

The basic feature at finite temperature of the ZPL and the multiphonon transition can be explained in the framework of the Debye approximation: [7, 13]

$$\frac{I_1}{I_2} = \frac{A_{ZPL}}{A_{ZPL} + A_{MP}} = \exp\left\{ - S\left[1 + 4\left(\frac{T}{T_D} \right)^2 \int_0^{\frac{T_D}{T}} \frac{x}{e^x - 1} dx \right] \right\} \cong \exp\left\{ - S\left[1 + \left(\frac{2\pi^2}{3} \right) \left(\frac{T}{T_D} \right)^2 \right] \right\} \quad (2.2.3)$$

Where T_D indicates the Debye temperature and S, the Huang-Rhys factor, represent the electron phonon strength of the system.

The expression (2.2.3), valid in the limit of $T << T_D$, well reproduces the experimental dependence of the ratio between the integrated area of the ZPL and the whole spectrum of the multi-phonon transitions as a function of temperature (Figure 2.2.4). Considering that the fundamental ZPL transition at 13099.2 cm^{-1} populates by thermal energy all the $^2T_2$ levels, it is worth to note that for ZPL intensity we have considered all the zero phonon transitions. The results of the fitting process (S = 2.1) confirm a medium coupling strength of the Fe ions in YAG crystals and the value of the Debye temperature T = 430 K is agreement with previous results. [7]

The increased spectral resolution of the second round of measurements allows a detailed analysis on the line width of the ZPL lines in order to account for the physical processes contributing to the line shape. The homogeneous width of the ZPL is determined by the relaxation time T_2 of the excited electronic state of the ion and can be estimated as

$$\Gamma = \frac{1}{T_{2\partial}} = \frac{1}{T_1} + \frac{1}{T_2'} \quad (2.2.4)$$

where T_1 is the population relaxation time and T_2' is the pure dephasing time, determined by the fluctuations in the optical transition frequency. The anharmonic decay of the final vibrational state along with the decay of the initial electronic state are responsible for the residual homogeneous ZPL width observed in the limit of $T \rightarrow 0$, which means that a nearly constant inhomogeneous contribution, caused by strain and defects randomly distributed in the host lattice, should be considered in all the temperature range and it should be analytically expressed by a Gaussian curve, while the homogeneous components are represented by Lorentzian profiles. In case both type of broadening processes are present, the line shape becomes the convolution of Lorentzian and Gaussian contributions: on the basis of the aforementioned considerations the total analytical reconstruction of the experimental spectra was performed by means of Voigt profiles: [23]

$$y = \frac{a_0 a_3}{2\pi \sqrt{\pi}\, a_2^2} \int_{-\infty}^{+\infty} \frac{\exp(-t^2)}{\frac{a_3^2}{2a^2} + \left(\frac{x - a_1}{\sqrt{2} a_2} - t \right)} dt \qquad (2.2.5)$$

where a_0 and a_1 are the area and the center of the Voigt curve, while a_2 and a_3 are the weight of the Gaussian and Lorentzian component respectively, corresponding to half width at half maximum of a pure Gaussian and a pure Lorentzian curve. However, it is worth to note that the ZPL1 line (figure 2.2.1 - inset) presents a nearly Lorentzian contour with a small asymmetry towards lower frequencies. These effects were previously noted in other samples with low concentration of dopants ($< 10^{18}$ cm^3) in high quality samples and reflect a very fine detail of the dopant-lattice interaction.[11] Generally these effects are not accounted for in the ZPL models and can be attributed to anharmonic contribution of the vibrations.

Figure 2.2.4 Experimental data of the ratio between the integrated area of the ZPL and the whole emission spectrum as a function of temperature. The solid curve represents the best fit curve according to the expression indicated and valid in the limit of $T \ll T_D$ (expression (3) in the text).

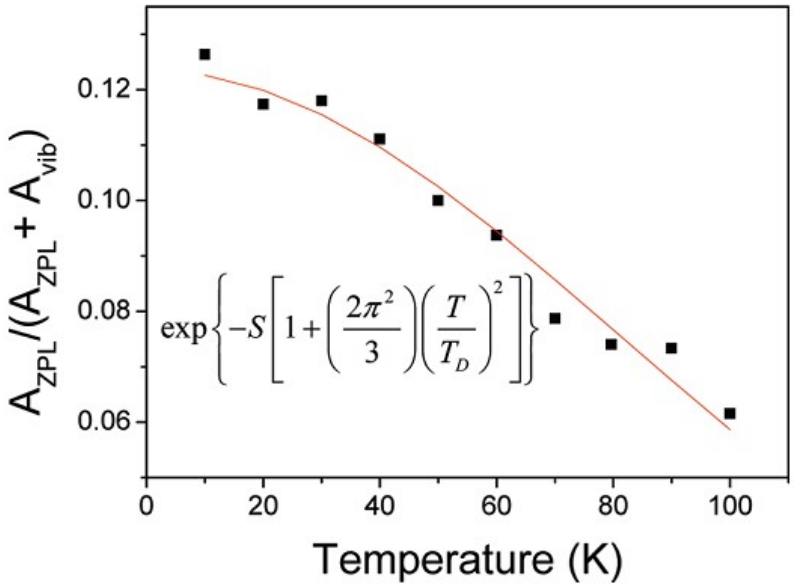

The rise in temperature leads to a broadening of the linewidths caused predominantly by the interactions between electrons and acoustic phonons. Actually, the initial electronic state lifetime is almost constant in the temperature range examined (< 150 K) and therefore the observed dependence was related to dephasing effect in the curves of potential energy for the ground and excited states, resulting from an additional quadratic term in the electron-phonon coupling for each vibronic band.

The expression of the dependence of the line width from the temperature contains mainly the contributions from the natural line width (which is temperature independent), the one-phonon direct process Γ^{D}, the Raman two-phonon process Γ^{R} and the radiative transition Γ^{rad}: [23,24]

$$\Gamma(T) = \Gamma_{0K}^{inh} + \Gamma^{D} + \Gamma^{R} + \Delta\Gamma^{rad} \qquad (2.2.6)$$

However not all these contributions have the same weight as the temperature increases and often they are not detectable in the analysis and can be neglected. The main contribution arises from the Raman two phonon process and, using the Debye model of phonon energies, as temperature increases the interactions between electrons and acoustic phonons result in a linewidth broadening $\Delta\Gamma$, described by: [23,24]

$$\Delta\Gamma^{R}(T) = \frac{k_b T_D}{\hbar}\frac{9}{4}\left(\frac{\omega}{\omega + 1}\right)^{2}\left(\frac{T}{T_D}\right)^{7}\int_{0}^{\frac{T_D}{T}}\frac{x^6 e^x}{\left(e^x - 1\right)^2}dx \qquad (2.2.7)$$

where ω is the quadratic coupling constant and T_D the Debye temperature.

Since the linewidth caused by radiative decay is very narrow, and the probability of direct processes is small at low temperature, it is reasonable to assume that the contribution from the Raman process is the main part of the Lorentzian component of the ZPL. Crystal defects such as dislocations and point defects such as colour centers should be expected in Czochralski single crystals, are

randomly distributed in the crystal and affect the electronic transition.

As previously discussed, and evidenced in figure 2.2.5a**,** only the Lorentzian component needs to be taken into account for the deconvolution process. Although the analysis was conducted in a narrow range of temperatures (between 10 K and 80 K, where the two components are still distinguishable), the fitting curves well reflect the experimental results, revealing a stronger coupling for the high energy component (ZPL2).

The line shift as a function of temperature $\delta\nu$ also depends on the electron-phonon coupling strength and is determined by several contributions, such as one-phonon or Orbach process. Since the peak position of the ZPL is independent of excitation energy, the contribution to the shift from localized modes may be neglected and, similarly to the line broadening case, the main contribution arises from the Raman two phonon process. [23,24]

$$\delta\nu = \frac{k_b T_D}{\hbar}\frac{3}{4\pi}\frac{\omega}{\omega+1}\left(\frac{T}{T_D}\right)^4 \int_0^{\frac{T_D}{T}} \frac{x^3}{e^x - 1}dx \qquad (2.2.8)$$

Figure 2.2.5a and 2.2.5b report the broadening (full width at half maximum) and line shift of the two main ZP lines (ZPL1 and ZPL2) of Fe ions in YAG crystal as a function of temperature in respect to the values measured for the minimum temperature reached. The figures report the best fit of the experimental results using the quadratic coupling constant ω, and the Debye temperature as free parameters in the equations (2.2.7) and (2.2.8). The capability of resolving two components allows the observation of two different trends in the ZP lines with varying temperature. For both fitting curves a value of 450 K of the Debye temperature was found but the ZPL component at higher energy (ZPL2) shows a heavier dependence from temperature, reflected by an higher coupling constant in respect to the value found for the ZPL1 line (-0.79 and -0.90 respectively). On the other hand, a distinct analysis

Figure 2.2.5 **(A)** Lorentzian and Gaussian component width of the two main Zero phonon lines (ZPL1 and ZPL2) as a function of temperature obtained from analytical reconstruction using a Voigt profile.

(B) Line shift of the two main Zero phonon lines (ZP1 and ZP2) as a function of temperature. The solid lines reproduce the best fit results according to the Raman two phonon contribution (expressions (6) and (7)). For the line broadening only the Lorentzian component were taken into account.

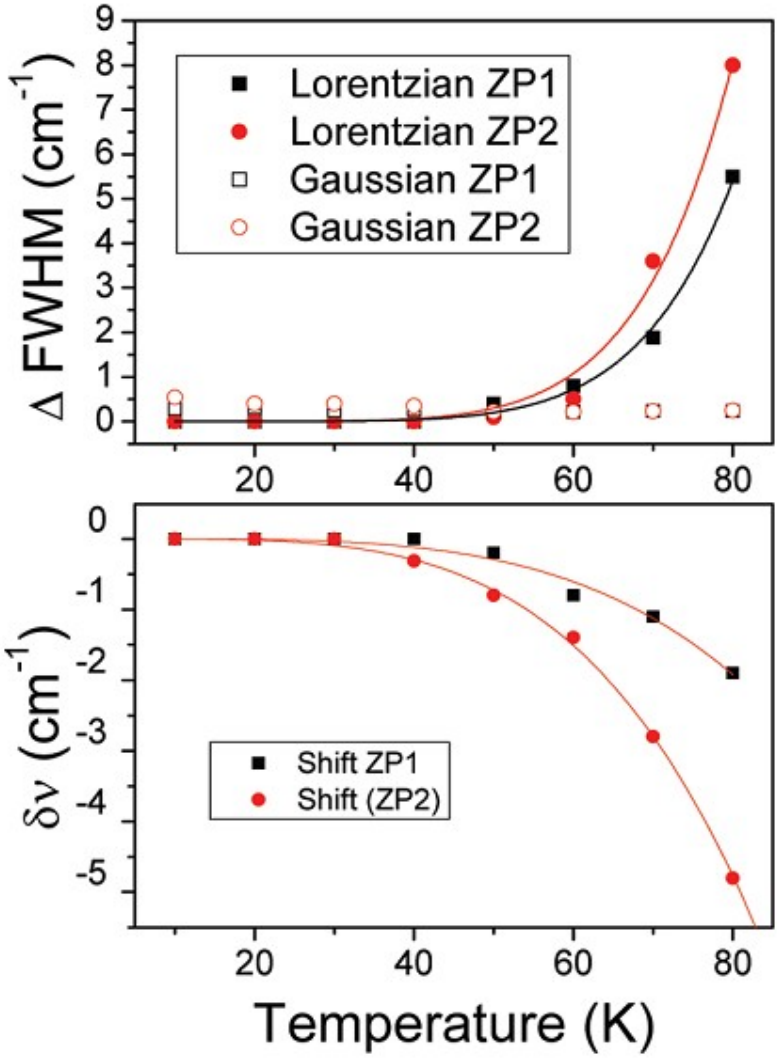

of the two components can be performed only up to 80 K, because the two bands are totally overlapped for higher temperatures and the deconvolution process looses its physical meaning. It is worth to note that the results obtained during these measurements are in agreement with the analysis previously performed on the not resolved spectra, which supplied a value of the coupling constant (-0.85) that seems to average the new results.[7]

The analysis accomplished on the line broadening confirm a stronger coupling for the high energy component. Moreover, the fitting results give a lower value of the coupling constant in respect to the analysis on the line shift (-0.73 and -0.78): this result should probably be addressed to the arbitrariness in the deconvolution process for higher energy spectra, nonetheless the results are sensibly more homogeneous in respect to the previous achievements.

In brief, the identification and study of four Zero Phonon Lines in low temperature high resolution spectra permitted to find out their peculiar characteristics, which pointed towards the presence of the doping Fe^{3+} ion in the tetrahedral site with a dynamic Jahn- Teller effect inherent in the $^4T_1$ excited states

Conclusions

The studies presented in this section permit to hint at the extent of possible approaches devoted to the comprehension of the structural characteristics in doped compounds and their variations in respect to undoped structures. LuYAP, the binary mixed compound of lutetium aluminum perovskite and yttrium aluminum perovskite was studied by transmission EXAFS spectroscopy at the absorption edges of both the elements occupying the same crystal site. These results, paired with the ones obtained by analogous measurements on pure yttrium and lutetium aluminum perovskites, were the key factor that permitted to observe structural variations caused by the yttrium doping of the lutetium aluminum perovskite, namely the decrease of local crystal order caused by the formation of YAP-like and LuAP-like cells. On

the other hand, the analysis of photoluminescence spectra of iron doped yttrium aluminum garnet samples performed in a low temperature range with excitation energies ranging from the band gap energy down to selective excitation of Fe^{3+} ions, permitted to give an answer to a still open matter of research on this particular compound, while offering results of general interest in the field of study of Zero Phonon Lines.

From this perspective, the results obtained by low temperature EXAFS spectroscopy on the absorption edges of lutetium and yttrium in LuYAP and the ones obtained from photoluminescence spectra recorded in a low temperature range with different excitation energies for Fe-YAG can be put together for their usefulness as tools of structural analysis.

REFERENCES

1. P.D. Dernier – Mat. Res. Bull. Vol.6 **1971**, 430-440.
2. J. Suda, O. Kamishima, K. Hamaoka et al. – J. Phys. Soc. JPN 72/6 **2003**, 1418-1422. 7.
3. E. Salje – Phys. Status Solidi A 3 **1974**, 11.
4. Die Dong, Kuang Xiao-Yu, Guo Jian-Jun et al. – Phys. Rev. B 72 **2005**, 073101.
5. S.R. Rotman, C.Warde, H.L. Tuller and J. Haggerty – J. Appl. Phys 66 **1989**, 3207.
6. Y.F. Chen, K.T. Wu, Y.D. Yao, C.H. Peng, K.L. You and W.S. Tse – Microelectr. Engin. 81 **2005**, 329.
7. A. Anedda,C. M. Carbonaro, D. Chiriu, R. Corpino, M. Marceddu, and P. C. Ricci – Phys Rev B. 74 **2006**, 245108.
8. J. P. Hurrell, P.S. Porto, I.F. Ching, S. S. Mitra and R.P. Bauman – Phys Rev B 173 **1968**, 851.
9. Yu. A. Voitukevich, M. V. Korzhik, V.V. Kuzmin, M.G. Livshits, and M.L. Meilman – Opt. Spectrosc. 63 **1987**, 810.
10. V. Lupei, A. Lupei, G. Boulon, A. Brenier, C. Pedrini and M.J. Elejalde – Phys. Rev B 49 **1994**, 7076.
11. O. Sild, K Haller, *Zero Phonon Lines and Spectral Hole Burning in Spectroscopy and photochemistry* (Springer Verlag Berlin Heidelberg) **1988** chap. 3- 4.
12. H. Wang, F.D. Medina, D.D. Liu, and Y.D. Zhous – J. Phys.: Condens. Matter 6 **1994** , 5373.
13. J.L. Skinner, and D. Hsu – Adv. Chem. Phys. 65 **1986**, 1.
14. P.Roschmann – J. Phys. Chem Solids 41 **1980**, 569.
15. S.H. Wemple, S.L, Blank, J.A. Seman and W.A. Biolsi – Phys. Rev B 9 **1974**, 2134.
16. W. H. Koschel, U. Kaufmann, and S. G. Bishop – Solid State Commun. 21 **1977**, 1069.
17. P. Koidl, Phys. Status Solidi B 74 **1976**, 477.
18. A. Hoffman, F.G. Anderson and J. Weber – Phys, Rev. B 41 **1990**, 5806.

19. K. Pressel, G. Bohnert, G. Ruckert A. Dornen and K. Thonke – J. Appl. Phys 71 **1992**, 5703.

20. J. P. Hurrell, P.S. Porto, I.F. ChNG, S. S. Mitra and R.P. Bauman – Phys Rev B 173 **1968**, 851.

21. K. Papagelis, S. Ves – J. Appl. Phys 94 **2003**, 6491.

22. Yu. A. Voitukevich, M. V. Korzhik, V.V. Kuzmin, M.G. Livshits, and M.L. Meilman – Opt. Spectrosc. 63 **1987**, 810.

23. Richard C. Powell, Physics of Solid-State Laser Materials (Springer-Verlag, New York) **1998**, chap. 4-5.

24. A. Ellens, H. Andres, A. Meijerink, and G. Blasse – Phys, Rev. B 55 **1997**, 173.

Section 3

This section presents the results of a different branch of studies, whose focus is not pointed towards looking for variations in the characteristics of a given compound by doping procedures but, on the contrary, looking at the actual characteristics of grown materials due to factors such as growth procedures and conditions or their stability in respect to varying environmental conditions. Performance studies of actual compounds in respect to external factors are a an obvious and necessary step on the way that leads to actual devices, since they permit to define fundamental characteristics such as best growth parameters or conditions of use. The general approach in this kind of procedures is to identify and try to minimize the undesired features that differentiate the grown compound from its ideal counterpart, as their presence is generally perceived as a possible drawback that could work against the expected performance of the final device.

Despite the common starting point of looking for the possible weak points in the grown materials, the general approach used in the present cases leads to opposite results. The comprehension and the analysis of differences between the ideal stoichiometric materials and the actual compounds (according to various parameters) is not devoted in principle to their elimination, but on the contrary to their possible utilization. The strong point of this line of thought is the exploitation of features that are generally overlooked or considered as unwanted outputs and their conversion into useful characteristics for possible applications in new devices.

In particular, three different studies will be presented. The first one shows an alternative to commercial $Lu_{0.2}Y_{1.8}SiO_5$ single crystals scintillating devices, the second concerns the possibility of inducing an abrupt trigger-like anatase-to-amorphous phase conversion on of TiO_2 powders according to the presence of oxygen, while the third suggests $Lu_{0.7}Y_{0.3Al}O_3$ as a possible candidate for optical data

storage (according to the abundance of induced oxygen vacancies). Once again, the techniques of choice and the results obtained by the measurements in each case are analyzed in the general framework of the particular aspects on which each study is focused. More precisely, Raman and photoluminescence spectroscopy were used in the first two cases while thermoluminescence was the technique of choice in the third one. The goals of measurements were to assess possible structural variations between $Lu_{0.2}Y_{1.8}SiO_5$ sol-gel and single crystal samples in first case, to measure the presence and amorphization of anatase phase of TiO_2, by looking at Raman spectra of the crystalline phase and photoluminescence spectra of oxygen vacancy defects in the second, and finally to analyze the abundance of oxygen vacancies in mixed lutetium/yttrium aluminum perovskites grown in oxygen-rich or nitrogen-rich atmospheres. All in all, the final results hint at these materials as possible and promising candidates for various applications, despite the fact that further analyses are still mandatory in order to develop possible application for future commercial devices.

3.1 Comparative analysis of mixed lutetium/yttrium oxyorthosilicate single crystals against sol-gel powders.

Among the crystal oxides, one of the most important is the family of rare earth oxyorthosilicates, RE_2SiO_5 (in the following RESO, RE=rare earth) whose application as scintillators for ionizing radiations is nowadays well established [1]. Within the RESO family, a relevant role is played by Cerium doped Lutetium crystals (Lu_2SiO_5, LSO), Yttrium crystals (Y_2SiO_5, YSO) and their solid solutions ($Lu_{2-x}Y_xSiO_5$, LYSO). Indeed the high stopping power for high energy photons (gamma at 511 KeV) is successfully employed in the Positron Emission Tomography (PET). Moreover the scintillation time of about 40 ns is much lower than other widely used conventional scintillators (i.e. BGO with 300 ns, CsI with 900 ns) [2]. Although the scientific results obtained in the last decades led to various successful high technology applications, these materials are still object of fundamental and applied

research to improve their features and to develop new devices and technologies according to the needs of the manufacturing market [3 ,4]. Indeed, single-crystal-based devices have several drawbacks, mainly due to the growth process, such as high temperature of crystallisation (more than 2000 °C) and relatively high cost associated to the Czochrlaski method. Thus, the development of cheaper and more easily grown materials is still an open field of research and a mandatory request in order to develop a new class of scintillators.

Among the several growth techniques, sol-gel method permits to obtain polycrystals at a considerably lower temperature and the direct preparation of scintillating thin films, particularly valuable in fundamental spectroscopic studies and for high resolution imaging, where the homogeneity of the scintillator coating is required. It is known, for example, that in the mammography field the delivered radiation dose is in the order of few mGy and is detected by thick films of scintillating materials. The sol gel prepared sample can be easily shaped in the form of thick films. We estimated that the X ray penetration depth in our samples is of the order of 600 μm, for a reduction of the incident radiation of about 2 order of magnitude. As a consequence , a 1 mm thick sample of about 50 mg/cm^2 weight can be applied to produce a sol gel based detecting device. Despite the large interest in single crystal scintillators, papers concerning the preparation and properties of sol-gel derived scintillators are few in numbers and recent in time .[4, 5] On this basis, a study on the optical properties of sol-gel derived cerium doped yttrium and lutetium ($Ce:Lu_{1.2}Y_{0.8}SiO_5$, with a Ce concentration of 0.1% in weight) oxyortosilicates can offer useful insights on the possibility of substituting single crystals devices with sol-gel based ones. The comparative analysis between commercial Czochralski- grown single crystals (CZ) and sol gel samples (SG) is conducted by means of low (8 K) and room temperature VUV and visible spectroscopy, steady and time resolved luminescence (PL) and Raman spectroscopy.

3.1.1 **Results and discussions**

The structure of the Re2SiO5 oxyorthosilicate compounds is fairly complicated and a solid solution of two oxyorthosilicates is far from trivial, since at least two different crystal structures can be identified as a function of ionic radius of the trivalent ions Re^{3+}, growing temperature or pressure [6-8]. Both structures have monoclinic symmetry and differ in the oxygen coordination of rare earth cations. One of them consists of isolated (SiO_4) tetrahedra, one oxygen site not silicon-bonded and two crystallographically independent Re^{3+} sites. The extra oxygen atoms are located at the centre of tetrahedra which form a two dimensional network parallel to the (100) plane. The crystal structure belongs to the P21/c space group.[6] In contrast, the other crystal structure of the phases (in general containing Re^{3+} elements with smaller ionic radius) has four Re_2SiO_5 formula units in a B-centred monoclinic unit cell and belongs to the C2/c space group. In this framework, Lu has a ionic radius of 0.848 Å and the crystal Lu_2SiO_5 belongs to the C2/c space group while Yttrium oxyorthosilicate can have both the structures. Y_2SiO_5 crystallizes in the first structure when annealed at temperatures lower than 1190 °C, otherwise it forms structures of the C2/c space group.[9] Recently the phase of the solid solution LYSO monocrystal, Czochrlaski grown, has been proven to belong to the monoclinic C2/c symmetry group [7]. The irreducible point representations of this symmetry group allows 96 Raman active vibrational modes (on a total of 192) where 48 are Ag and 48 Bg [8, 10]. Figure 3.1.1a presents the unpolarized Raman spectra of the pure LYSO CZ samples. The spectrum reproduces different bands in the range from 60 to 1000 cm^{-1}, where some peaks are not resolved and overlapped. In order to identify the symmetry group of the SG samples, its Raman spectrum (see figure 3.1.1 b) was compared to the one of the SG sample. The two spectra are very similar and all the frequency peaks of the vibrational modes coincide, allowing the assignment of sol-gel samples to the C2/c symmetry group (table 3.1.1). The optical properties of the two classes of samples were compared starting from the

Figure 3.1.1 Unpolarized Raman spectra of the Czochralski grown (above, in black) and sol gel grown (below in red) LYSO samples.

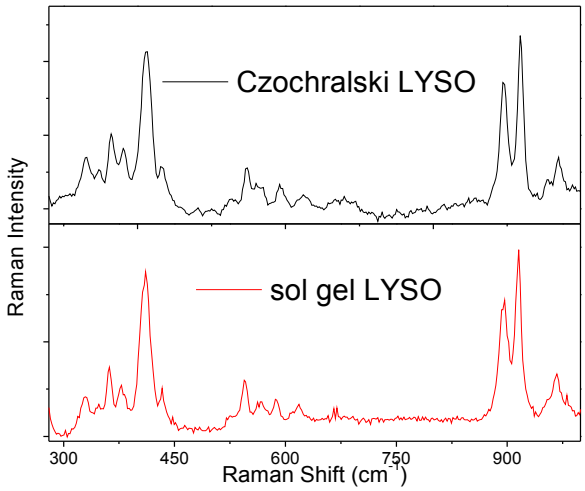

figure 3.1.2 Photoluminescence (PL) and Photoluminescence Excitation (PLE) spectra of the main cerium emission at 400 nm for Czochralski grown (above, in black) and sol gel grown (below in red) LYSO samples.

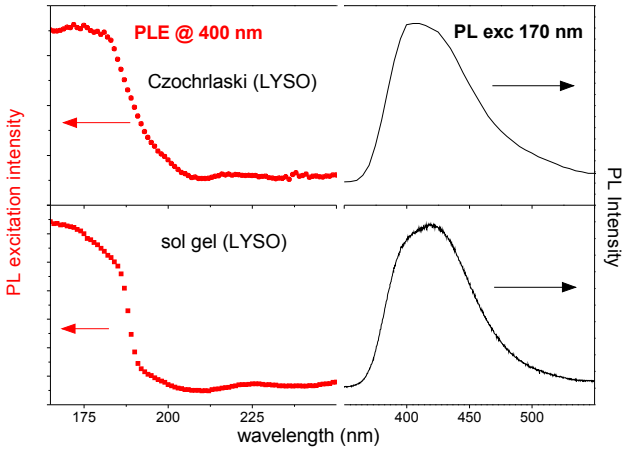

Table 3.1.1 Raman peaks and vibrational modes of LYSO. Asterisks indicate main peaks.

Raman modes	LYSO (300 k) (cm^{-1})
A_g	338, 376, 402*,426, 487, 541*, 617, 889*, 911*, 962
B_g	264, 321, 356*, 408*, 435, 514, 560, 585*, 949

excitation of luminescence spectra (PLE) of the main cerium emission at 400 nm (figure 3.1.2). The two spectra present the same dependence in the high energy range (from 240 to 170 nm), with the predicted edge at 190 nm (6.52 eV) due to the gap of LYSO crystal [11] and the overall luminescence spectra excited with band to band energy (8.2 eV – 150 nm) are due to recombination at the Cerium site. Ce ions can substitute the bulk rare earth elements (Lu and Y in this case) in two inequivalent sites: The RE1 site has six nearest neighbours O atoms plus one extra oxygen with larger bond distance and it is directly excited at 290 and 260 nm [11]. The RE2 site is bounded to only six oxygen atoms because the bond distance of the seventh O atom is greater than 3 Å , so it cannot be considered as bonded to RE and is selectively excited at 320 nm [10, 11]. It is worth to note that the luminescence spectra with high energy excitation is given by the overlapping of the radiative response from the two Cerium sites. In order to better understand the different optical properties of differently grown classes of samples, low temperature (8 K) PL measurements were performed.

The contribution from each site was partially isolated by selective excitation at 295 nm for the Ce1 site and at 320 nm for the Ce2 site. The spectra arising from the 295 nm excitation for the differently grown samples are very similar among each others (figure 3.1.3A) while considerable differences in the two emission spectra excited at 320 nm are observed (figure 3.1.3B). In these spectra the emission from the CZ samples can be assigned solely to the recombination from the Ce2 site, due to negligible spectral overlapping with the photoluminescence spectra from Ce1, while the emission spectrum of the SG sample, excited at 320 nm, shows a considerable contribution from other recombination sites. In order to highlight all the emission components from the SG sample, the PL spectrum excited at 295 nm, previously assigned to selective recombination at Ce1 site, was normalized with respect to the intensity of the PL emission, excited at 320 nm, in correspondence of the peak maximum at 394 nm. Then, it was subsequently subtracted from the latter PL spectrum, obtaining a spectrum that strictly resembles the PL spectrum arising from the CZ sample excited at 320 nm, and previously assigned to the selective

Figure 3.1.3 Photoluminescence (PL) spectra of Czochralski and sol gel grown LYSO samples. Excitation wavelength is 295 nm (Ce1 site) for the spectra in the upper half of the picture and 320 nm (Ce2 site) for the spectra in the lower half.

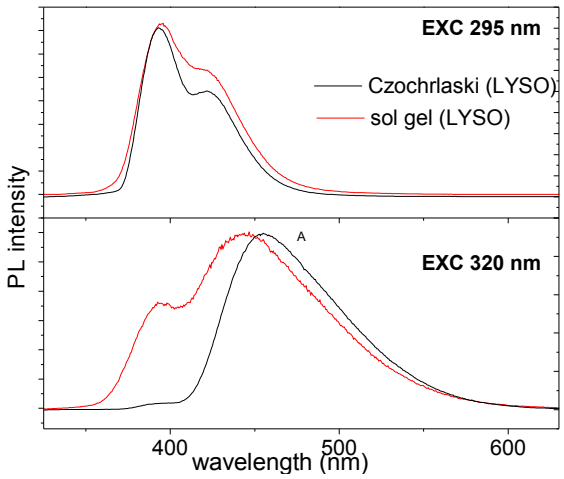

Figure 3.1.4: [above] normalized PL spectra of sol gel grown LYSO samples (in blue, excitation at 295 nm; in red excitation at 320 nm) and spectrum obtained by the subtraction of the former from the latter (in black). [below] Comparison between Czochralski grown PL spectrum and difference PL spectrum obtained above.

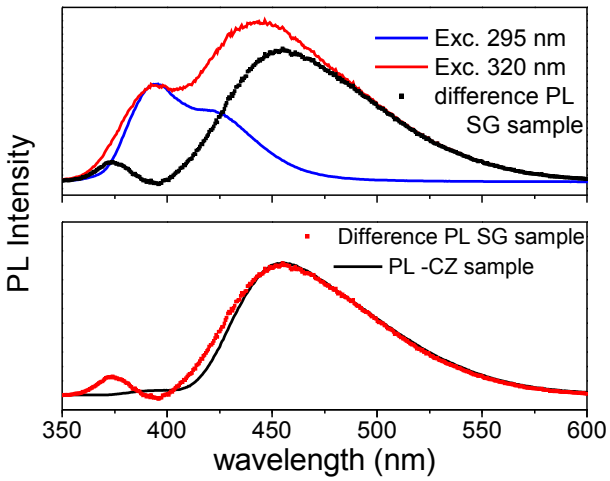

recombination at Ce2 site (figure 3.1.4). Therefore is possible to recognize only two radiative recombination components coming from the two inequivalent Cerium sites, Ce1 and Ce2.

The curve-fitting analysis of the collected spectra can offer a deep insight in the previous assignment. Two Gaussian curves for each site (figure 3.1.5) were used as basis function, since each contribution to the photoluminescence at the Cerium sites arises from the recombinations from the 5d levels to the fundamental doubly-split 4f levels $^2F_{5/2}$ e $^2F_{7/2}$ (see table 3.1.2). From the analytical reconstruction it is also possible to estimate in 2000 cm^{-1} the spin-orbit energy split of the Cerium F-levels in Lutetium Yttrium oxyorthosilicates from the energy differences in the peak of Gaussian components in both the differently grown classes of samples.

The high resemblance of the site selective photoluminescence spectra of the two classes of samples is a further indication of the high similarity of the crystal structure and of the similar behaviour of the cerium dopant inside the LYSO matrix.

In order gather deep understanding of the dynamics of the recombination at the Cerium sites, time resolved measurements were performed. By exciting at 290 nm and 320 nm at 8 K, single exponential time decay was observed for all the measured luminescence. PL lifetimes of 33 ns was measured for Ce1 site of both the classes of samples, while the lifetime constants for Ce2 site were 46 ns and 38 ns, for the CZ and SG sample respectively (figure 3.1.6). The results are summarized in table 3.1.3.

The faster kinetics observed in the polycrystals can be interpreted by taking into account the differences highlighted in PL spectra by the site selective excitation at 320 nm previously discussed. Indeed while the excitation at 320 nm of single crystals induces PL emission mainly from the Ce2 sites, with almost no signal from the Ce1 sites, the same excitation in polycrystals induces a remarkable emission from the Ce1 site, accompanied by a decrease of PL lifetime of the Ce2 sites. The correlation of the Ce1 and

Figure 3.1.5: Curve-fitting analysis of the photoluminescence spectra of sol-gel samples. Two Gaussian curves for each site were used as basis function.

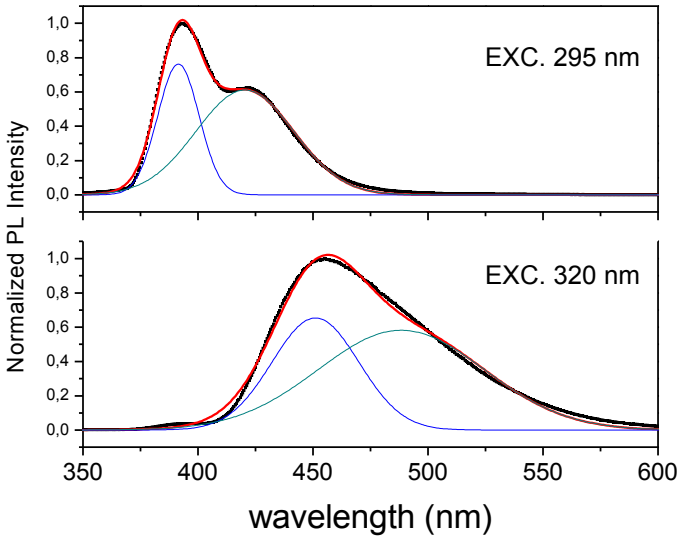

Figure 3.1.6: Time-resolved photoluminescence measurements and fit of Czochralski and sol-gel grown samples (excitation at 320 nm, Ce2 site).

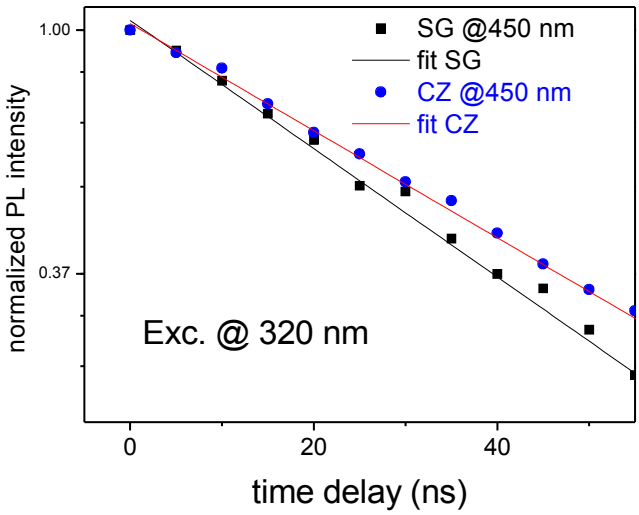

Ce2 sites observed in the polycrystalline samples is indicative of a non radiative cross relaxation mechanism among Cerium ions belonging to different crystalline sites.

In conclusion, the results of the comparative structural and performance analysis suggest that, from a spectroscopic point of view, sol-gel prepared LYSO can be a useful alternative to Czochrlaski grown materials in the detection of ionizing radiations and for scintillating devices in the low energy X ray range.

Table 3.1.2 Results of the fitting by Gaussian curves of photoluminescence spectra of Figure 3.1.5.

295 nm excitation			320 nm excitation	
Curve 1	**Curve 2**		**Curve 1**	**Curve 2**
420	391,5	**X_C (nm)**	488,3	451
42,5	18,0	**FWHM (nm)**	72	37
32	17,2	**AREA**	52,6	30

Table 3.1.3 Photoluminescence lifetimes of Czochralski and sol gel-grown samples with different excitation wavelengths.

Sample	Excitation (nm)	Emission (nm)	τ (ns) 8 K	τ (ns) 290 K
CZ	295	393	33	31
Sol gel	295	393	33	30
CZ	320	460	46	36
Sol gel	320	460	38	32

3.2 Vacuum-triggered anatase-to-amorphous phase conversion of TiO_2 nanopowders.

Nanosized titania (TiO_2) crystals are promising materials for their appreciable characteristics, such as low production cost, non toxicity and high stability against high energy irradiation; subsequently a great deal of effort was devoted to the study of TiO_2 in photocatalysts, dye-sensitized and photovoltaic applications.[12,13]

The most common crystal structures of TiO_2 are anatase, rutile and brookite, the latter being known as high-pressure phase. Anatase converts to rutile at temperatures between 400 and 1200 °C, but different parameters such as grain size, impurities and material processing influence the effective rate of the polymorphic reaction.[12, 14-16] Recently, it was reported that room-temperature phase conversion of anatase to rutile TiO_2 can be achieved by doping the TiO_2 nanoparticles with transition metal ions.[17] These transformations are very important both from a scientific as well as a technological point of view, as they can be useful in fields such as the photochemistry of TiO_2 surfaces, which is deeply correlated with the band gap, the electronic structure and the role of bulk and superficial defects. [18, 19] Evidences of optically assisted phase transformation of TiO_2 nanocrystals from anatase to amorphous are reported. In opposition to other light induced processes (based on temperature effect), in the present case the reason for phase conversion must be ascribed to surface modifications by a proper depletion of adsorbed oxygen on the crystal surface [20, 21]. The phase conversion at room temperature is induced by low intensity visible light excitation and it brings out the key role of oxygen vacancy defects and chamber atmosphere on high surface TiO_2 samples. The analysis of in situ Raman spectra gives immediate proof of the crystallographic structure of the samples and was utilized as a probe to study the effect of visible and intrinsic excitation of bulk TiO_2 as a function of the chamber atmosphere. In order to observe the effects of superficial oxygen depletion on TiO_2 nanopowders, two different excitation energies were used during the experiment: the 1.96 eV light from a He-Ne laser with energy density lower than 0.1 W/cm^2, intended to measure Raman spectra without altering the

sample structure, and the 2.54 eV light of an Ar^+ laser to induce structural changes on the analyzed samples. The latter was also used for luminescence measurements with a power density as low as 0.1 W/cm^2. In order to study the structural change, experiments were performed with different excitation power densities of the 2.54 eV source, starting from 0.1 W/cm^2 and rising with steps of 0.5 W/cm^2. Raman and luminescence spectra were collected after visible excitation.

The effective local temperature was checked from the ratio of the Stokes/anti-Stokes Raman bands of the 144 cm^{-1} peak of the anatase phase for a power density of 10 W/cm^2, which is well beyond the one utilized in the experiment, but no significant increase in the local temperature was observed. No phase change was revealed in the sample structure with red light as the sole excitation source and vacuum conditions well beyond the ones considered in the experiment (about $1.33x10^{-4}$ Pa).

Raman analysis of the as-grown powder in room conditions reveals the typical spectrum of the anatase phase, while the 2.54 eV excitation beam induces a broad and weak luminescence centered around 2 eV, ascribed to the luminescent recombination at the oxygen vacancy sites [22].

3.2.1 Results and discussions

Figure 3.2.1A reports the Raman spectra recorded after 20 seconds of visible light excitation for different excitation power densities (as labeled in figures 3.2.1A and 3.2.1B) with a chamber pressure of 4.66 Pa. Consequently the PL signal intensity (figure 3.2.1B) changes after visible illumination, indicating a structured recombination process. A sudden phase variation is evidenced in the spectrum recorded after excitation with 4 W/cm^2. The absence of the typical Raman anatase peaks reveals a degradation of the initial phase and suggests the formation of an amorphous one. This indication is confirmed by the increase of the PL band previously ascribed to the presence of oxygen vacancy defects [22]. Optical and Raman imaging of the sample after excitation in vacuum conditions are reported in Figure 3.2.2 to better show the local effect of visible light illumination.

Figure 3.2.1: Raman (A) and photoluminescence (B) spectra of TiO_2 nanoparticles after illumination with 2.54 eV laser beam and power density as indicated in legend in vacuum conditions. The spectra were acquired after excitation by a low intensity laser (0.1 W/cm^2) at 1.96 eV and 2.54 eV for Raman and photoluminescence measurements, respectively.

A **B**

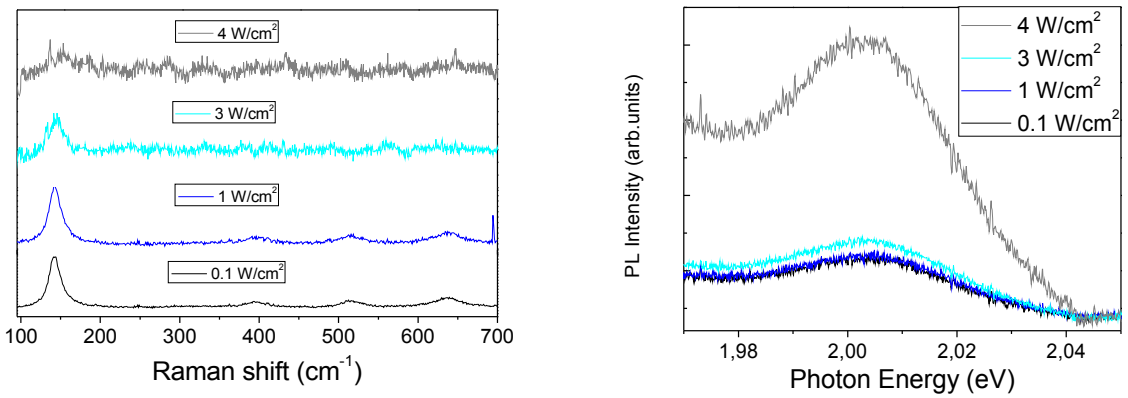

Figure3.2. 2: Optical (LEFT) and Raman (RIGHT) imaging of TiO_2 nanopowders after visible light illumination in vacuum conditions. The varying color between orange and white indicates the local structure of the sample ranging from amorphous (orange) to Anatase (white), with the pale orange region being the one of degraded Anatase.

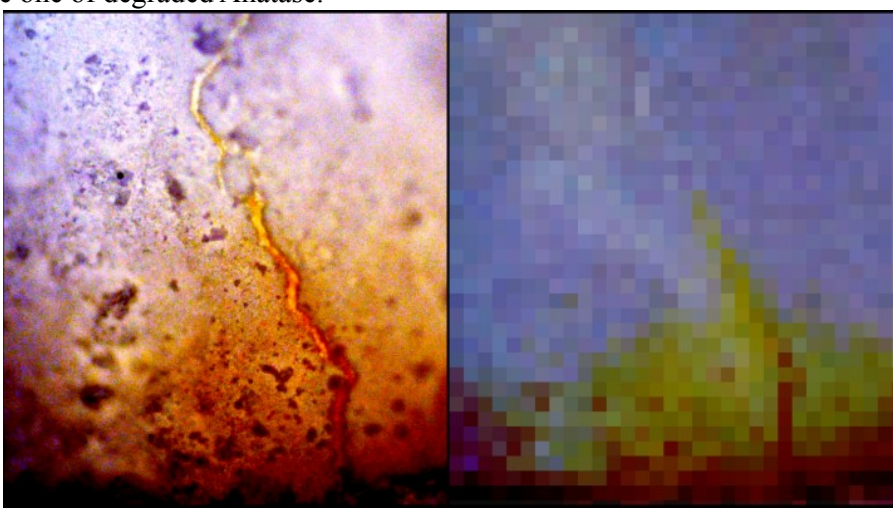

The irradiated zone appears optically orange, while the part of sample kept in dark remains white. Only the irradiated zone of sample presents a Raman spectrum different from anatase phase, while the border of the illuminated region shows a Raman spectrum of deteriorated anatase phase.

It is worth noting that an opposite behavior can be observed in air: Raman peaks of anatase remain unchanged or at least more settled as the power density increases, while the photoluminescence intensity quickly decreases (Figure 3.2.3) with irradiation time. Moreover, the trend observed on anatase Raman peaks as well as the luminescence band is partially compensated by keeping the sample in dark at room conditions for several hours. Similar results were previously observed in TiO_2 nanocrystals with mean diameter of 7.9 nm for excitation at 2.60 eV in air and the PL intensity decay was assigned to light induced change in the surface electronic structure.[22]

As previously shown in Figures 3.2.1 A, B and 3.2.3 evolution in the behavior of anatase nanoparticles after visible light illumination is strongly influenced by the atmosphere in the experimental chamber.

Recent and independent investigations show that, depending on the initial surface conditions and on the oxygen partial pressure in the experimental chamber, crystal excitation with suitable light can increase the net rate of either absorption or desorption of molecular oxygen [22,23]. The increase of surface activity under light excitation can be attributed to the increase of electron and hole centers available for capture and recombination processes at specific vacancy sites.

The excitation energy in the experimental set-up is lower than the optical band gap of the anatase nanosized particles so absorption of visible light should be ascribed to the presence of charged color centers[24]. The nature of these color centers is strictly related to oxygen vacancies generated by a proper choice of growing parameters like temperature and chamber atmosphere or controlled by doping elements [25-27]. According to Serpone, the loss of an O atom in a metal oxide leaves behind an electron pair trapped in V_O giving rise to an F center, while a positively charged F center is equivalent to a single electron associated to the O vacancy [28]:

Figure 3.2.3: Variations in the integrated area of photoluminescence band *vs.* irradiation time of TiO_2 nanoparticles after illumination with 2.54 eV laser beam in air. The insets show the Raman spectra acquired with the minimum and the maximum irradiation times respectively. The spectra were acquired after excitation by a low intensity laser (0.1 W/cm^2) at 1.96 eV (Raman) and 2.54 eV (photoluminescence).

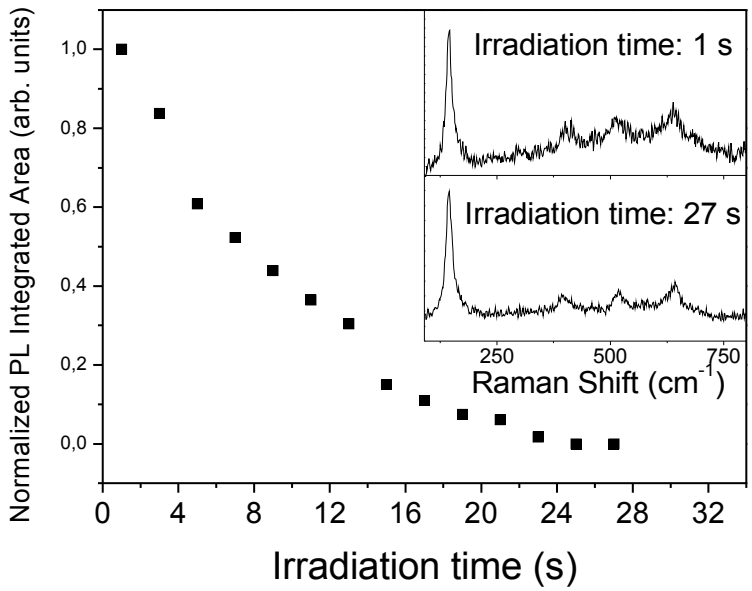

Thus,the color centers associated with oxygen vacancies are neutral F and positive charged F^{+} and F^{+2} centers [29].

$$-O^{2-} - \rightarrow O + V_O + 2e^-$$
$$V_O + 2e^- \rightarrow F$$
$$V_O + e^- \rightarrow F^+$$

The energy scheme of the anatase nanoparticles should follow the diagram of energy levels illustrated in figure 3.2.4, so that the behavior of the sample under intrinsic excitation with different atmospheric conditions can be discussed as follows: in oxygen-rich atmosphere the O_2 molecules act as photoexcited electron scavengers, thus collecting the electrons raised to the conduction band from F-type color centers (figure 3.2.4A). [24 ,30, 31] The O_2 molecules can be adsorbed on the TiO_2 surface at least in two specific sites: from a five-coordinated Ti^{3+} site, generating O^-_2 by one electron transfer from Ti^{3+} to the adsorbed O_2 molecule (figure 3.2.4A, blue Lu balls and white O balls), or a vacancy site, where two Ti^{3+} ions "close" each other with a bridge provided by the captured O_2 molecule, thus forming a diamagnetic peroxide ion O_2^{2-} between the two Ti^{3+} ions (figure 3.2.4A, blue Lu balls and purple O balls). Both sites compensate oxygen vacancies and a continuous visible illumination facilitates O_2 adsorption and compensation of defects present at the TiO_2 surface from the initial conditions. Since the luminescence peak is originated by surface states, the decay in PL intensity is a direct indication of the compensation of surface defects due to adsorption of O_2 molecules during blue illumination and was already observed after band to band excitation.[31] In our opinion, the visible excited luminescence is related to electron-hole recombinations taking place between nearest Ti^{3+} and F+ centers. In accordance with this hypothesis, in a recent theoretical work based on DFT in local density approximation, the model featuring the excess of one electron trapped in Ti^{3+} sites is very close in energy with partially or highly delocalized solutions, where the extra charge is distributed over

Figure 3.2.4: Schemes of energy levels and illustrations showing the reaction of TiO_2 nanoparticles to irradiation in air conditions (A) and vacuum conditions (B). Both the schemes depict the F-type color centers as a black-colored level on the bottom right corner of the scheme, the Titanium atoms as a cyan(3+)/blue(4+) level on the top right corner and the Oxygen ions as a gray level on the left side of the scheme. For clarity purposes only the 5-fold Titanium-coordinated Oxygen is depicted in the scheme. The illustrations depict the final conditions on the surface of TiO_2 nanoparticles in both conditions.

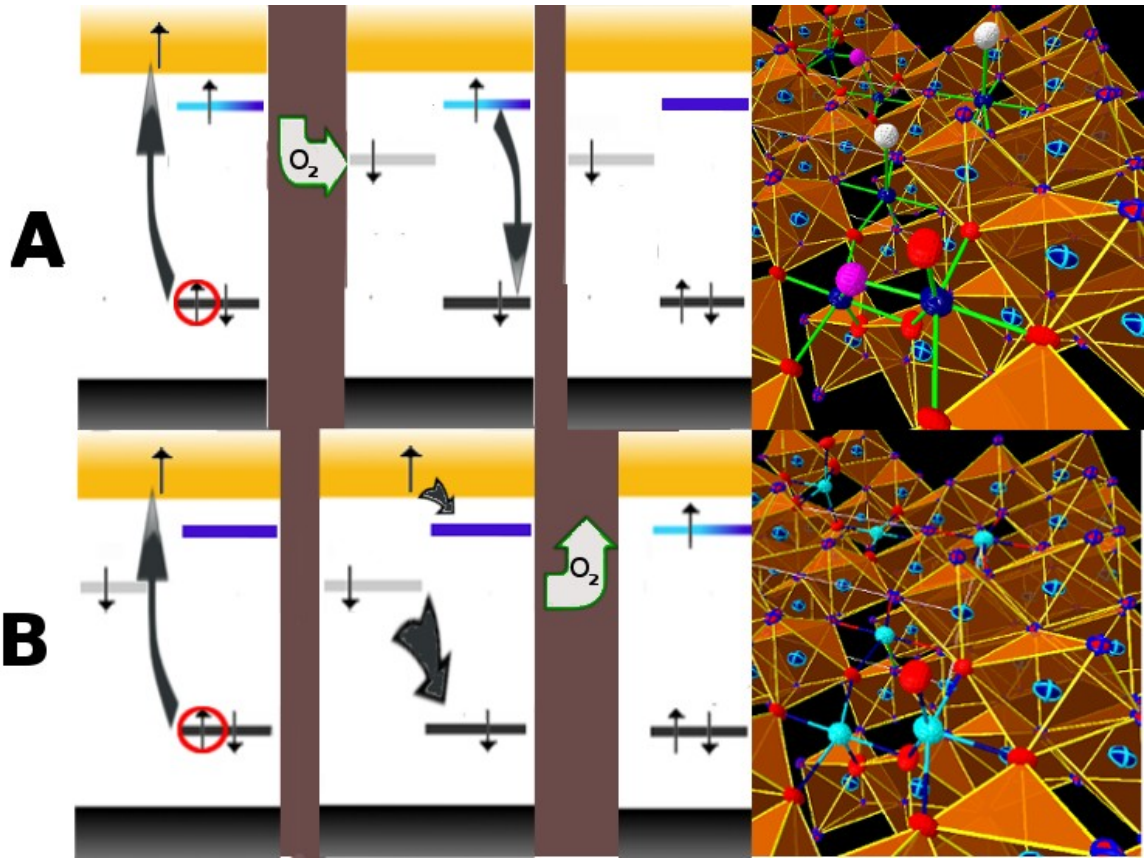

several Ti ions, thus suggesting the important statistic role of temperature and time [32]. This fact may explain the re-activation of PL peaks after keeping the sample in dark conditions for several hours [24].

In vacuum conditions (figure 3.2.4B) the effect of promoting the photo-excited electron to the conduction band is the de-adsorption of O_2 molecules. Starting from the stable situation in which the O_2^- are adsorbed on the Oxygen vacancy site of the TiO_2 surface (in a 5-fold bond or as a bridge between two Ti^{4+}) and from the experimental assumption that no further oxygen molecules are available in the experimental chamber, illumination with visible light causes electrons from the color centers to be excited to the conduction band. The photo-excited electrons in the conduction band will be captured by Ti^{4+} at the surface in correspondence to oxygen vacancy sites, while O_2^- and O_2^{2-} leave their electrons to the F-type color centers, thus allowing the de-adsorption of O_2 molecules. In truth, photo-desorption kinetics of O_2 molecules in ultra high vacuum chamber was studied on TiO_2 rutile samples under extrinsic excitation in recent investigations[30]. The photo-desorption is caused by recombination of electrons trapped in O_2^- molecules with holes in the valence band. Although our experiment is performed with intrinsic excitation, the mechanism remains very similar and brings to the formation of a high superficial density of Ti^{3+}. Actually the well-established reaction scheme, known to occur during UV irradiation in anatase TiO_2, [32]

$$TiO_2 + h\nu \rightarrow TiO_2(h^+ + e^-)$$

is still valid but now the holes are localized in the F+ centers; conduction band electrons can be trapped in Ti^{4+} ions in the bulk or at the surface:

$$Ti^{4+} + e^- \rightarrow Ti^{3+}$$

The kinetics of surface processes involving oxygen exchange can be accounted by the rate equation

$$\frac{d n_{O2}}{dt} = \gamma_A p n_S - \gamma_D n_{O2} m \qquad (3.2.1)$$

where n_{O2} stands for density of adsorbed O_2 molecules, m and n_S for densities of trapping hole and

electron centers, respectively, p for the gas pressure, γ_A and γ_D for probability factors of O_2 capture and electron-hole recombination, respectively. In eq. (3.2.1) we indicate the total air pressure instead of the oxygen partial pressure. This can be admitted in our case where different air pressure conditions with fixed molar composition are considered. Densities of centers change with time and are dependent on the intensity of exciting light. The sign of the right member in eq. (3.2.1) establishes how surface attains its stationary state: desorption requires that

$$p < \frac{\gamma_D n_{O2} m}{\gamma_A n_S} \tag{3.2.2}$$

If the desorption rate largely dominates the surface processes, and by assuming that $\gamma_D m$ maintains a stationary value, we have $n_{O2} : \exp(-\gamma_D m t)$. Since the density of hole trapped centers far from saturation depends on light intensity as m $m : \sqrt{I}$, in the case of slow processes $\Delta n_{O2} : -\sqrt{I}\,\Delta t$.[23]

Experiments insights hint that surface depletion of adsorbed oxygen accompanied by formation of Ti^{+3} centers causes the anatase structure to become unstable and to collapse to an amorphous state. The phase degradation was previously observed after ball milling, high pressure (up to 24 GPa) and high doping treatment. [15,16,33]

It is worth to note that the threshold power density varies as a function of the experimental chamber pressure. As the pressure decreases, the power density required to induce amorphization decreases as well.

Figure 3.2.5 shows a graph of chamber pressure *vs.* power density reporting the conditions corresponding to the achievement of phase change. The procedure for each point is the same illustrated in figure 3.2.1, where, starting from the lowest power density of the 2.54 eV line (0.1 W/cm^2) and rising with steps of 0.5 W/cm^2, the sample was illuminated for 20 s and Raman spectra were recorded (in dark condition) using the low power He-Ne line after each excitation. The point indicates the

condition where the anatase phase cannot be further distinguished.

The process illustrated above can be used to give a kinetic and thermodynamic model that fits with experimental point of figure 3.2.5. Actually electron-hole processes could account for releasing of adsorbed oxygen against a partial compensation by absorption on surface electronic centers; the latter being originated from trapping of conduction band electrons at the surface defects. This process continues until the stationary state is reached. For a given temperature, any stationary state achieved by following the previously described procedure can be uniquely represented by a point in the plane (I,P).

Roughly, a thermodynamic investigation of oxygen exchange at the stationary state can be addressed by taking into account of configurational entropy on crystal surface, say Sc, dependent on oxygen coverage and of free energy contribution, say g(I,T), dependent only on light intensity and on temperature. Thus, the isothermal process of oxygen exchange from pressure P_1 to pressure P_2 can be described by [34]

$$g(I_2,T) - g(I_1,T) + T\Delta S_c = RT \ln \frac{P_2}{P_1} \qquad (3.2.3)$$

We focus our interest in the curve bordering the stability domain of the anatase phase. Here, at any given pressure, oxygen coverage compensating the superficial vacancies reaches its minimum quantity as the intensity crosses the threshold above which amorphization of the crystal phase becomes thermodynamically advantageous. As the external pressure decreases, the light intensity required to reach the threshold state decreases as well due to the diminished rate of oxygen interactions with crystal surface. However, at the lower end of the bordering curve, where molecular interactions become negligible, the threshold state is reached at intensity I_0 that allows electron-hole processes to involve the remaining adsorbed oxygen molecules having higher charge states. In eq. (3.2.3) we could account for these different oxygen states by including an "over-pressure" κ in such a way that P is replaced by

P+ κ. Actually, we should expect that any point of the bordering curve has a different threshold oxygen coverage. Nevertheless, it is reasonable to discard the change of configurational entropy along that curve. On these grounds, eq. (3.2.3) can be modified as

$$g(I,T) - g(I_0,T) = RT \ln\left(\frac{P}{\kappa} + 1\right) \tag{3.2.4}$$

Really, the terms appearing in the left hand of eq. (3.2.4) are phenomenological representations of non-equilibrium states dominated by counter-balanced kinetic processes involving oxygen exchange. Thermodynamics suggests that any small change with respect to a stationary state is repelled due to an increase in entropy production. [35] For this reason it is natural to assume $g(I,T) \propto m$ where m stands for the density of hole centers. Thus, a change dn of oxygen coverage leads to a change $g(I,T)\,dn \propto m\,dn$ of the "surface energy" which is proportional to the change of the (bimolecular) electron-hole recombination rate.

Finally, by taking into account the assumption that far from saturation $m \propto \sqrt{I}$,[23] we can rewrite eq. (3.2.4) as

$$I = \left[\frac{RT}{\beta} \ln\left(\frac{P}{\kappa} + 1\right) + \sqrt{I_0}\right]^2 \tag{3.2.5}$$

where β stands for a suitable factor to be determined.

Figure 3.2.5 reports the best curve fit for the experimental points, where the limit of the power density (I_0) at high vacuum condition is about 2.33 W/cm^2 and the over pressure κ is 0.8548 Pa.

Figure 3.2.5: Chamber pressure *vs.* power density graph showing the conditions of achieved amorphization of TiO_2 nanoparticles irradiated in vacuum conditions and the best fitting curve for the chosen kinetic and thermodynamic model (also shown).

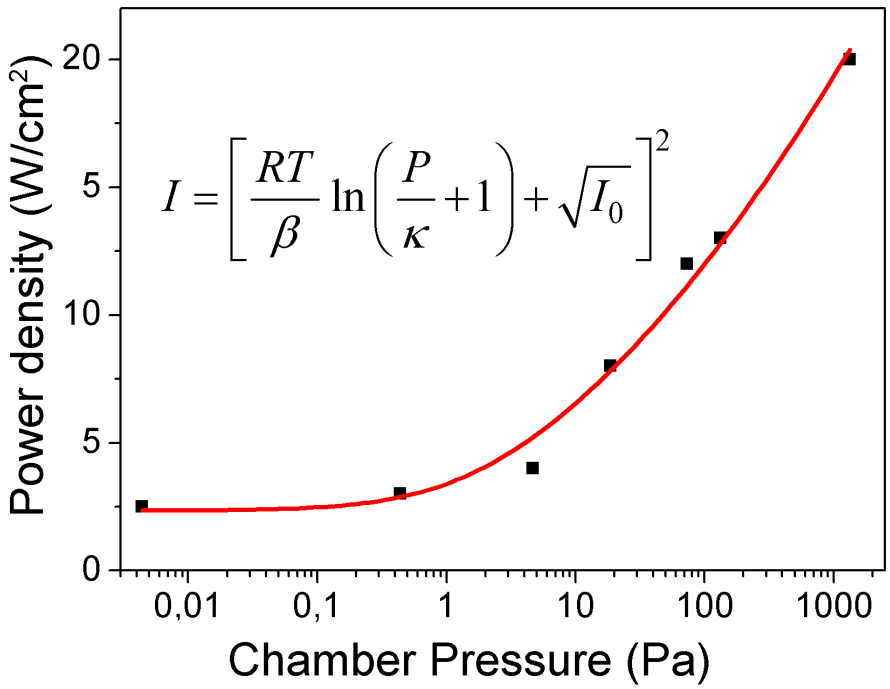

To sum up, a proper choice of the incident radiation power density and of the oxygen partial pressure in the experimental room effectively allows a local and specific control over anatase-to-amorphous phase conversion of TiO_2 nanoparticles thanks to the key role of surface oxygen defects. While the possibility of tailoring such defects opens new possibilities in the development of applications based on TiO_2 nanoparticles, the abundance or lack of oxygen can also be exploited during the actual growth of compounds, despite the obvious consideration that variations in the experimental conditions in the latter case will result in differences in the structural peculiarities of the final compound rather than on phase conversion procedures.

3.3 Optical recording of informations on mixed lutetium/yttrium aluminum perovskite single crystals

The study of conversion processes characterized by a foreseeable and manageable optical response is of interest for basic research in high gap oxides in order to improve the optical emission efficiency, trapping and de-trapping mechanism of the excited electrical charges in the light-crystalline matrix interaction. However, in this sense trapping mechanism is generally regarded as an unwanted result instead of a good opportunity for optically written information to be kept in a safe. Excitation and de-excitation studies of oxides and their solid solutions as a function of different cations and stoichiometry is still an interesting field for the fundamental research, as the presence of doping and codoping RE ions in the matrices can create activator and/or co-activator centers for additional energy transfer paths.

The analysis of the optical properties of a high gap oxide such as mixed lutetium/yttrium aluminum perovskite, doped or co-doped with RE elements ($Ce:Er:Lu_{0.7}Y_{0.3}AlO_3$) in the light of previous considerations is therefore necessary in order to engineer its optical properties for non conventional

applications. In particular, trapping effects can be thought as mechanisms capable of storing information optically written on the crystal matrix with X, UV radiation, despite their reduction in optical emission efficiency. The expected results, therefore, can reach a twofold goal: an improvement of the scintillating efficiency for classical applications or a new starting point for unconventional applications in the field of the optical storage. However both targets assume the knowledge, the control and the tuning of the intrinsic/extrinsic optical properties on which radiation-material interaction is based.

3.3.1 Basic Model

The knowledge of energy level distribution for the fundamental and excited levels of RE dopants inside the forbidden band of host matrix is crucial for engineering and developing new devices. Thus, the application of an empirical model capable of achieving this task is the first priority lacking, up to now any “a priori” theoretical model. With this background, some remarks on both RE properties and some experimental results are the starting points of such a model.

First, it's valuable to note that the excitation energy for RE electrons going from the 4f lowest state to the 5d lowest state follows the bonding energy of electrons for an increasing population of the non excited 4f level [36]; a lower value can be found in presence of one (La^{2+}, Ce^{3+}) or eight electrons (Gd^{2+}, Tb^{3+}), while a half or a fully occupied 4f level (Eu^{2+}, Gd^{3+} and Yb^{2+}, Lu^{3+} respectively) shows a higher excitation energy. On the other hand, the energy gap between the top of the matrix's valence band and the fundamental state of the doping RE 4f levels is also linked to the bonding energy, although the dependence between energy and number of occupying electrons is opposite.

The aforementioned considerations, coupled with a valuable number of examples from the literature, form the basics of models based on the bonding energy and the variations in atomic radius for different REs: despite the position of the 5d levels being directly affected by the crystalline field

effects (in fact the same RE shows widely different values depending on the compound), a simple yet precise model has been developed by Dorenbos and successfully applied, in order to relate the position of f and d levels for different REs with the same crystalline site of a given compound [37 -39].

The excitation energy E(Ln) of a RE electron going from a stable $4f_n$ state to a less energetic $4f_{n-1}5d$ state in the free ion case varies in a non regular way compared to the increase of n; it has been experimentally shown that such variation is independent of the oxidation state and can be expressed as:

$$E(Ln) = [E_{cs}(Ln^*)-E_{cs}(Ln)+ [E4f^{n-1}(Ln^*) – E4f^n)Ln)] + E5d(Ln^*) \quad (3.3.1)$$

where the asterisk points the RE excited $4f^{n-1}5d$ states.

The first term in square brackets is the difference in total energy experienced by the electrons of the full shells during the f → d excitation, while the second one, depending on the variation in total energy of the 4f electrons due to the excitation, should be positive and depends heavily on the ionization energy of the $4f^n$ electrons. The last term E5d(Ln*) indicates the bonding energy of the 5d levels after the excitation.

Relation 3.3.1 still holds for REs in a specific crystalline matrix, when an additional term, almost independent of the chemical element but cogently relied the matrix, is added. Once the A matrix is determined, the energy variation E (Ln_1, Ln_2,A) between 3+ RE ions is given by:

$$E(Ln_1)-E(Ln_2) = [E_{5d}(Ln_1^*)-E_{5d}(Ln_2^*)] + [\Delta E_{4f}(Ln_1) - \Delta E_{4f}(Ln_2)] + [\Delta E_{cs}(Ln_1) - \Delta E_{cs}(Ln_2)] \quad (3.3.2)$$

where, similarly to the free ion case, the ionization energy variation [ΔE4f(Ln_1) - ΔE4f(Ln_2)] is predominant. In addition, taking into account the crystal fields of different A_1 and A_2 matrices with the same dopant (Ln), we obtain:

$$E(A_1)–E(A_2) = [\Delta E_{5d}(A_1) - \Delta E_{5d}(A_2)] + [\Delta E_{4f}(A_1) - \Delta E_{4f}(A_2)] + [\Delta E_{cs}(A_1) - \Delta E_{cs}(A_2)] . \quad (3.3.3)$$

In this case, the ionization energy variation gives a small contribution since it is slightly dependent of the matrix: 4f electron are shielded by the $5s^2$ e $5p^6$ full shells and are almost independent of the crystalline order.

On the contrary, for the same RE in different compounds the most important contribution to the energy difference involves the outer shell electrons i.e. 5s and 5p electrons respect to 5d electrons.

Generally, it is possible to state that the energy variation $\Delta(Ln,A)$ of the $4f^{n-1}5d$ levels for RE ions in the A matrix is almost constant compared to the one of free atom [37, 38]. Therefore it is possible to predict the energy of f → d transitions in different compounds once the transition of a single RE in the same matrix is known. By referring to such transitions for a specific Ln element (e.g. Ce) the energy can be obtained from (3.3.2) and (3.3.3):

$$E(Ln, A) = E_{Ce,free} - \Delta(Ln,A) + \Delta E_{Ln,Ce} \qquad (3.3.4)$$

where the $\Delta E_{Ln,Ce}$ is the energy difference between the f → d transition for a generic Ln^{3+} RE and the first allowed dipole transition of the Ce^{3+} ion. This term also can be considered related to the compound but, almost, independent from RE ions. Experimental results show that , for the same crystallographic matrix, $\Delta E_{Ln,Ce}$ is constant within 9 meV and no dependence on the compound and on its RE doping were reported [38].

A similar discussion can be carried out on the fundamental 4f levels of the bivalent ion in the same matrix. The first step is defining the charge transfer band as the transition from the top of the valence band to the fundamental 4f state of the bivalent ion; secondly, one should assume constant the contraction of the levels due to the RE doping the matrix. Now it is possible to obtain the scheme of the 4f levels for the Ln^{2+} ion from the charge transfer band of a RE of choice, [40]:

$$E_{Vf}(n+1,2+,A) = E_{CT}(N,3+,A) + \Delta E(Ln,n) \qquad (3.3.5)$$

where E_{Vf} (n+1,2+,A), the energy of the transition from the top of the valence band to the 4f level for the 2+ ion with n+1 electrons, is the sum in energy of the charge transfer band for a generic ion (identified as "N" in eq. 3.3.5) in the A compound, with the variation in energy of one of the 3+ Rare Earth ion featuring n electrons in the 4f state. Bearing in mind that neither the crystal field effect on the RE 5d levels, nor the spin-orbit effect on the 4f levels were considered, it is possible at this point to summarize a general representation of the energy position of electronic levels for RE^{3+} RE^{2+} ions for the compound of our interest.

Figure 3.3.1 shows the scheme for the position of the 4f and 5d energy levels of REs in the LuYAP matrix, where the 4f level of Ce^{3+} has been positioned at 2 eV from the valence band inside the forbidden band [41], the energy for the 4f→ 5d transition has been assumed 3.5 eV and a charge transfer band for Eu^{2+} of 5.02 eV [42]. The scheme hints the fact that in case the matrix is doped by Ce^{3+} ions and by a chemical element whose fundamental level of the 2+ ion falls into the prohibited band, the resulting material is a potential candidate for data storage applications. Exciting such material with sufficient energy to form a hole in the valence band and an electron in the conduction band (e.g. X rays, γ rays, etc), the aforementioned hole will likely be trapped in the Ce^{3+} site, thus becoming Ce^{4+}; similarly the electron will be trapped in the co-dopant site if the latter has become a bivalent ion with the fundamental level inside the prohibited band. Subsequent excitations suited to involve the 4f level of the 2+ ion will act as a reading function of the stored information; the electron thus obtained from the bivalent trap will recombine in the Cerium site according to the 5d-4f levels emission.

According to the model calculations for the LuYAP matrix, elements such as Er, Eu, Sm, Tm and Yb are good candidates as stable trapping centers for excited electrons in the conduction band, while chemical elements such as Ho, Dy, Nd and Pr are not suitable to be long term traps because their fundamental level as bivalent ion is in the proximity of the conduction band, so that a low thermal contribution is sufficient to drastically increase the natural fading.

Figure 3.3.1 Energy level scheme of the divalent and trivalent lanthanides in LuYAP matrix. Round spots indicate 4f levels for 3+ ions and square spots indicate 4f levels for 2+ ions, while the red line indicates 5d levels for 3+ ions.

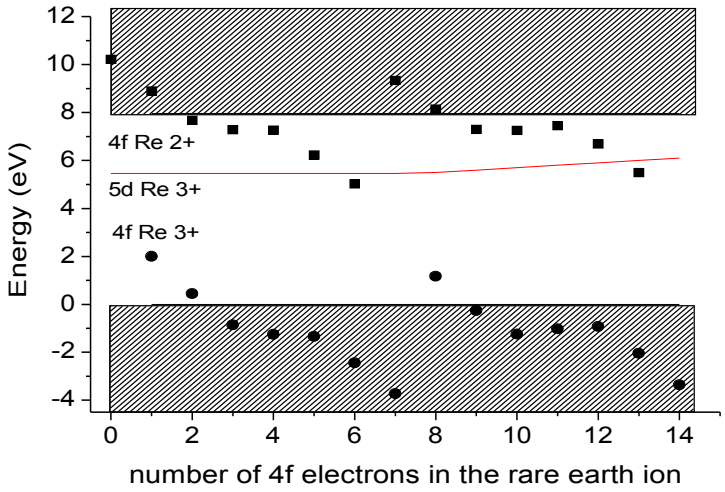

Figure 3.3.2 Thermoluminescence spectra of Ce doped and Er Ce codoped LuYAP samples. Radiolumines

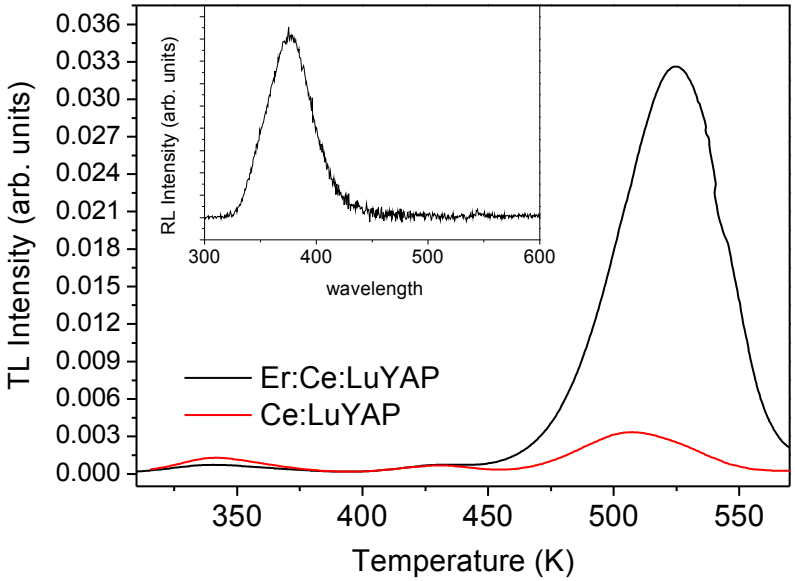

3.3.2 Results and discussions

Figure 3.3.2 shows the thermoluminescence (TL) spectra of Ce:LuYAP sample with and without Er^{3+} codoping. The role of Er as trapping center is shown by the main peak around 525 K while the radioluminescence spectrum (inset) shows solely the Ce contribution.

The model will give at the first glance, the role of the co-dopant; Er^{3+}; however this assumption cannot rule out different trapping mechanism not related to RE ions but, instead, to stoichiometric matrix defects like oxygen vacancies.

In this case, the choice of a particular growing procedure is discriminating In particular, growth atmosphere, temperature and thermal treatments can, selectively, influence the origin and the concentration of the trapping centers. Perovskite crystals seem to be a useful candidate for a controlled crystal matrix due to the reproducibility of the trap distribution during the growth process.

The role of oxygen vacancies as trapping centers was first hypothesized through a comparison of TL curves registered before and after annealing processes [43]. Figure 3.3.3 shows TL emission of a LuYAP sample grown in nitrogen atmosphere after x-ray irradiation at room temperature (500 mGy) and kept in dark condition for five minutes before the measurements. In accordance with the literature, the curve features three principal peaks at 350, 430 and 530 K

Analogous measurements were carried out for LuYAP samples grown in oxygen-rich atmosphere (Figure 3.3.3); the intensity of the TL emission shows a significant intensity decrease since a lower concentration of oxygen vacancy trap sites is expected.

By applying the Generalized Order of Kinetic model of thermoluminescence (GOK) to the TL experimental curve, we assumed that the thermal response can be described by the superposition of three components, i.e.[44, 45]:

$$I(T) = \sum_{j=1}^{3} A_j \cdot S_j \exp\left(-\frac{E_j}{kT}\right)\left[1 + \frac{\left(b_j - 1\right) S_j}{\beta}\int_{T_1}^{T_2} \exp\left(-\frac{E_j}{kT}\right) dT\right]^{-\frac{b_j}{b_j - 1}} \qquad (3.3.6)$$

where A is a constant related to the trap concentration, E is the trap depth (i.e. the energy needed to release the trapped charge), k is the Boltzmann's constant , b and S are phenomenological parameters related to the trapping kinetics and frequency factor respectively, and β is the sample heating rate (0.25 K/s). The results are shown in Table 3.3.I.

Actually, considering that the TL area is proportional to the concentration of trap sites, a simple integration gives about a factor of ten as the estimation of the trap concentration ratio between the nitrogen-grown and oxygen-grown samples.

Moreover, from Figure 3.3.3 and from the results of the fitting process it seems that although the parameters of the TL peaks remain unchanged, the intensity ratio between them depends from the growth process. In particular the peaks at lower temperature show a drastic decrease in intensity, revealing a different distribution of the oxygen vacancies.

In order to understand the effect of a subsequent illumination on the trapped carriers, TL measurements were performed in the previous conditions and illuminating the samples for two minutes with the 632 nm line of an He-Ne laser after the X-rays exposure (Figure 3.3.4). The TL emission was drastically reduced with different efficiency for the traps sites in particular the low temperature peak is almost absent.

A tentative explanation suggest that the electrons excited by X ray radiation into conduction band, are trapped by the 2+ oxygen vacancy center while a Ce^{4+} ion is left behind. The electron captured by an oxygen vacancy can be optically released by red illumination to a Ce^{4+} ion leading to a Ce^{3+} ion for the excitation state and yielding 5d 4f luminescence at about 380 nm.

This very sharp re-emission (or up-conversion) is generated by the rapid emptying of the electron traps paired with the recombination at the cerium site and it is strictly connected to previous exposition. Considering the releasing time of the traps at room temperature (table 3.3.I) and the very highly

Figure 3.3.3 Thermoluminescence spectra of LuYAP samples grown in nitrogen rich (above) and oxygen rich (below) ambient.

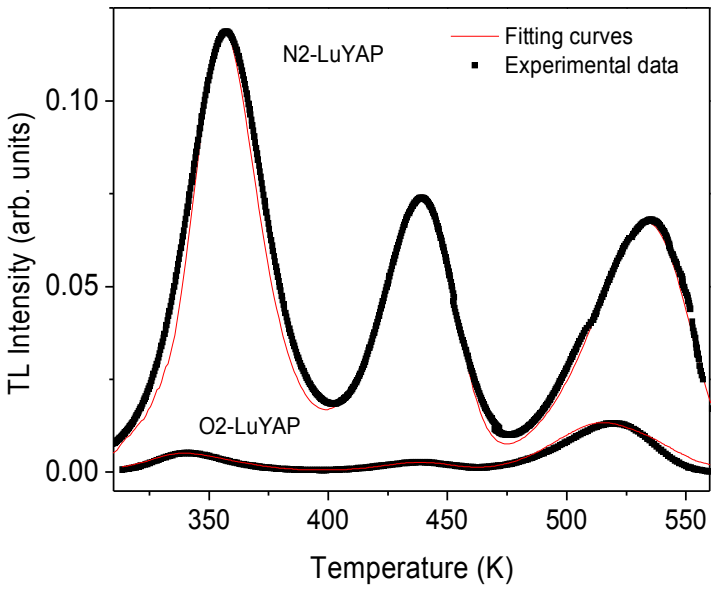

Figure 3.3.4 Thermoluminescence spectra of LuYAP samples grown in nitrogen atmosphere before and after 632 nm light illumination.

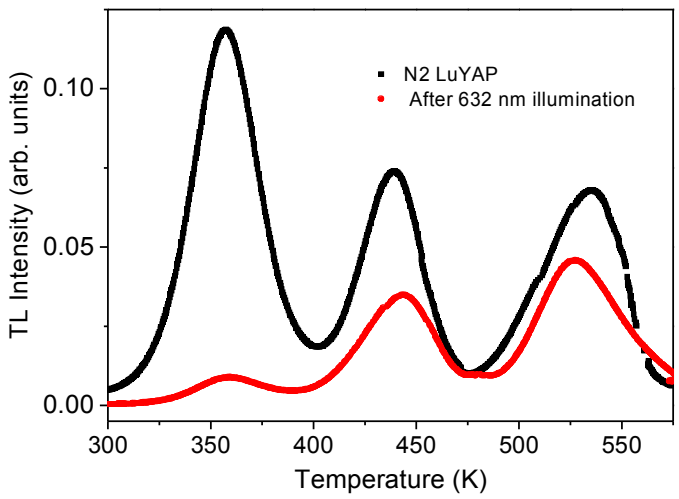

efficient upconversion radiative emission, the material can be easily suggested as a transparent display for a x-ray digital panel with a red light as “reading light”.

Obviously red light illumination is also able to erase the “data” previously stored or to “drain” the electron traps: the erasing efficiency is a function of duration and power density illumination.

Further measurements are a mandatory task in order to develop actual devices, but the results obtained thus far hint at this method of storing information (photons) as a step towards a multitude of hybrid, optoelectronic devices to be used in ‘quantum information’ processing, communication networks and signal processors, and could lead to developments in the research field of combined meta-materials.

Table 3.3.1 Thermoluminesce parameters from the fitting procedure described in equation 3.31 and shown in Figure 3.3.3.

	N_2 LUYAP	**O_2 LuYAP**
A1	18	0,8
b1	2,25	2,25
S1	1,5 x 10^{15} s^{-1}	1,5 x 10^{15} s^{-1}
E1	1,17 eV	1,17 eV
A2	11,5	0,37
b2	1,2	1,2
S2	9,2 x 10^{11} s^{-1}	9,2 x 10^{11} s^{-1}
E2	1,19 eV	1,18 eV
A3	13,9	2,7
b3	1,1	1,3
S3	1,2 x 10^{10} s^{-1}	3 x 10^{10} s^{-1}
E3	1,25 eV	1,25 eV

CONCLUSIONS

This section presented three studies on different materials, united by the use of a different point of view in respect to the ones of previous sections. In spite of looking at the structural characteristics of the compound itself or at the structural variations caused by doping processes, in the present cases the main focus was pointed towards finding the actual characteristics of the grown materials for their possible applications in new devices.

The results of the comparative analysis between sol-gel and Czochralski grown LYSO crystals demonstrated that the former can be in principle considered an alternative to single crystals for applications like detection of ionizing radiations or for scintillating devices in the low energy X ray range. On top of that, a "structural" variation was found from the comparison of photoluminescence spectra in the doping by cerium atoms: while the Czochralski grown samples present a predominant doping on just one of the possible sites, sol-gel grown samples feature a difference in the cerium doping of the two allowed sites. The study of externally induced crystal-to-amorphous phase conversion in TiO_2 nanoparticles demonstrated an interesting characteristics that, given the number of applications of this compound, could be exploited in many different fields. In particular, the anatase-to-amorphous phase conversion of TiO_2 nanoparticles can be controlled specifically by a proper choice of the incident radiation power density and of the oxygen partial pressure in the experimental room in a locally narrow e temporally fast way by acting on the surface oxygen defects. The possibility of inducing variations in a compound by controlling the atmosphere during the growth process was the focal point of the third study, which aimed at analyzing and controlling oxygen vacancies formed during the Czochralski growth of doped LuYAP single crystals. The presence of vacancies acting as electronic traps is commonly seen as a drawback in terms of scintillation performance but it can be also

considered as a possibility for electronic storage, thus offering a new starting point for the development of optical storage devices: variations in the abundance of oxygen vacancies in differently-grown doped LuYAP single crystals were measured and the possibility of of their tailoring for possible applications as optical storage devices was verified. To sum up, the change in perspective presented in the aforementioned studies suggests that the exploitation of measurement tools usually devoted to structural analyses on a more performance-wise note can lead to new insights on already known materials, remarking features of interest for the development of new devices.

REFERENCES

1. J.K. Lee, R.E. Muenchausen, J.S. Lee, Q.X. Jia, M. Nastasi, J.A. Valdez, B.L. Bennett and D.W. Cooke – Appl. Phys Lett 89 **2006**, 101905.
2. B. Hautefille, K. Lebbou, C. Dujardin, J.M. Fourmigue, L. L. Grosvalet, O. Tillement, C. Pedrini – J. of Crystal Growth 289 **2006**, 172.
3. L.S. Qin,Y.T. Wu, H.S. Shi, W.X. Chai, K.Y. Shu, G.H. Ren, X.F. Chen – IEEE Transactions on Nuclear Science 56 **2009**, 2979.
4. P. Yun, Y. Shi, D. Zhou and J. Xie – Journal of Rare Earths 27 **2009**, 801.
5. J. Felsche, Structure and bonding, 13 **1973**, 99.
6. D. Chiriu, N. Faedda, A. Geddo Lehmann, P.C. Ricci, A. Anedda, S. Desgreniers, and E. Fortin – Phys. Rev. B76 **2007**, 054112.
7. P. C. Ricci, D. Chiriu, C. M. Carbonaro, S. Desgreniers , E. Fortin , A. Anedda – J. Raman Spectroscopy Vol. 39 **2008**, 1268.
8. C. Cannas, A. Musinu, G. Piccaluga, C. Deidda, F. Serra, M.Bazzoni, S. Enzo – Journal of Solid State Chemistry 178 **2005**, 1526.
9. A. Ellens, H. Andres, A. Meijerink, G. Blasse Phys. Rev. B 55 **1997**, 173.
10. P.C. Ricci, C.M. Carbonaro, D. Chiriu, R. Corpino, N.Faedda, Ma.Marceddu, A.Anedda – Materials Science and Engineering: B, 146 **2008**, 2.
11. A. J.Wojtowicz, W. Drozdowski, D. Wisniewski, J. Lefaucheur, Z. Galazka, Z. Gou, T. Lukasiewicz, J. Kisielewski – Optical Materials, 28 **2006**, 85.
12. X. Chen and S.S. Mao Chem. Rev. 107 **2007**, 2891.
13. F. Milanesi, G. Cappelletti, R. Annunziata, C.L. Bianchi, D. Meroni, S.Ardizzone – J. Phys. Chem.C 114 **2010**, 8287–8293.
14. N.T. Nolan, M.K. Seery and S.C. Pillai – J. Phys. Chem. *C* 113 **2009**, 16151.

15. H. Rath, P. Dash, T. Som, P.V. Satyam, U.P. Sing, P. K. Kulriya, D. Kanjilal, D. K. Avasthi and N.C. Mishra – J. Appl. Phys. 105 **2009**, 074311.

16. X. Pan, X. Ma – J. Solid State Chem. 1777 **2004**, 4098.

17. H.Y. Lee, W.L. Lan, T.Y. Tseng, D. Hsu, Y.M Chang and J.G. Lin Nanotechnology 20 **2009**, 315702.

18. J. Shi, J. Chen, Z. Feng, T. Chen, Y. Lian, X. Wang and C. Li – J. Phys. Chem. C 111 **2007**, 693.

19. S. Begin-Collin, A. Gadalla, G. Le Caer, O. Humbert, F. Thomas, O. Barres, F. Villieras, L. Toma, G. Bertrand O. Zahraa, M. Gallart, B. Honerlage, P. Gilliot – J. Phys. Chem. C 113 **2009**, 16589.

20. H.L Ma, J.Y. Yang, Y. Dai, Y.B. Zhang, B. Lu, G.H. Ma – Appl. Surface Science 253 **2007**, 7497.

21. P.A.M. Rodrigues, P.Y. Yu, G. Tamulaitis, S.H. Risbud – J. Appl. Phys 80 **1996**, 5963.

22. W. F. Zhang, M. S. Zhang, Z. Yin – Phys. Stat. Sol. (a) 179 **2000**, 319.

23. J.T.Yates Jr. – Surface Science 603 **2009**, 1605.

24. K. Komaguchi,T. Maruoka, H. Nakano, I. Imae,Y. Ooyama,Y. Harima – J. Phys. Chem.C 114 **2010**, 1240 .

25. A.V. Emeline, V.N. Kuznetsov, V.K. Rybchuk, N. Serpone – Int. J. Photoenergy **2008**,1–19.

26. T. Seika, T. Yagisawa, N. Kamiya – J.Phys.Soc.Jpn. 73 **2004**, 703–710.

27. F. Spadavecchia, G. Capelletti,S. Ardizzone,C.L. Bianchi, S. Cappelli, C. Oliva, P. Scardi, M. Leoni, P. Fermo – Appl. Catal.,B 96 **2010**,314–322.

28. N. Serpone – J. Phys.Chem.B 110 **2006**, 24287–24293.

29. T. Lu, S. Wu, L. Lin, W. Zheng – Physica B **2001**, 304,147.

30. H. Lindstrom, H. Rensmo, S. Sodergren, A. Solbrand, S. Lindquist – J. Phys. Chem. 100 **1996**, 3084.

31. C. Di Valentin, G. Pacchioni, A. Selloni – J. Phys. Chem. C 113 **2009**, 20543.

32. M.P. De Lara-Castells, J.L. Krause, J. Chem. Phys. 115 **2001**, 4798.

33. Z. Wang, S. K. Saxena Solid State Comm. 118 **2001**, 75.

34. C. P. Flynn, Point Defects and Diffusion (Clarendon Press, Oxford) **1972** chap. 2.

35. G. Nicolis and I. Prigogine – Self-Organization in Non-equilibrium System (John Wiley and Sons, Inc. New York, London, Sydney, Toronto) **1977** chap. 3.

36. C. K. Jorgensen – Mol. Phys. 5 **1962**,271.

37. P. Dorenbos – Phys. Rev. B 65 **2002**, 235110.

38. P. Dorenbos – J. Phys.: Condens. Matter 15 **2003**,8417.

39. E. van der Kolk, P. Dorenbos, C.W. E. van Eijk, S. A. Basun, G. F. Imbusch and W. M. Yen – Phys. Rev. B 71 **2005**,165120.

40. P. Dorenbos – J.Lumin. 111 **2005**, 89.

41. C. Pedrini,D. Bouttet and C. Dujardin – Proceedings of the International Conference on Inorganic Scintillators and their Applications(SCINT95),Delft **1996**, 103.

42. Y.Wang, X.Guo, T. Endo,Y. Murakami and M. Ushirozawa – J. Solid State Chem. 177 **2004**, 2242.

43. A. Vedda, M. Martini, F. Meinardi, J. Chval, M. Dusek, J. A. Mares, E. Mihokova and M. Nikl – Phys. Rev. B 61 **2000**,8081.

44. J. McKeever – Thermoluminescence of Solids (Cambridge University Press,Cambridge) **1985**.

45. L. Ninisto and M. Leskela – Handbook on the Physics and Chemistry Rare Earth, edited by K.A. Gschneider Jr. and Eyring L.(Elsevier Science Publisher, NewYork) **1987**.

CONCLUSIONS

The presented results outline a general approach to material science that begins from purely structural considerations and leads up to the proposal of possible applications for developing new devices. This general outlook can be narrowed in order to summarize and point out the specific results obtained in each study.

The starting point was given by structural characterization of RE aluminum perovskite crystals in order to assess the effective formation of the expected structure and, in second instance, to fill the existing gap between applicative and structural studies. The importance of a good balance between so diverse approaches can be summed up by keeping in mind that a detailed structural knowledge, that allows to reasonably foresee the results of engineering processes, represents the basis for possible new developments (either as new materials or as new applications of already known compounds).

Following this approach, perovskite compounds featuring various chemical elements in the same crystalline site were at first analyzed by Raman spectroscopy: experimental results pointed out the actual formation of the expected structures and, on a more general note, remarked variations in the vibrational modes among the perovskite compounds in relation to the presence of different chemical elements.

Follow-up analyses were carried out in dependence to the results of interest for each material and to the ones still missing in literature.

In the case of LuAP, which had not been fully characterized yet from a structural point of view despite its relative oldness and its applications either by itself or as a basis for the LuYAP mixed compound, the main target was to complete the structural characterization by collecting experimental data still missing . On the other hand, the case of YbAP was quite the opposite, since its absolute novelty meant the complete lack of any data in literature. Analyses were, consequently, devoted to find the most

interesting characteristics suitable for scintillator applications, where Yb-based compounds are being proposed as an alternative to Ce-doped ones.

EXAFS spectroscopy was, therefore, used to obtain structural information on the local characteristics of LuAP and on their variations with temperature, while photoluminescence measurements were performed on YbAP in order to obtain radiative time decays as a function of temperature. These analyses offered a deeper insight on $LuAlO_3$ and the first experimental results on a brand new material such as $YbAlO_3$, whose characteristics indicate a promising candidate for fast scintillation purposes.

After the structural characterization of the crystalline matrix, a further step was to study its variations influenced by doping elements. The extent of possible approaches is broad depending on the specific points of interest and on the peculiarities of each doping procedure, but it's possible to hint at useful measurement techniques in order to get informations both on a general and a more local note.

In particular, LuYAP, the binary mixed compound of lutetium aluminum perovskite and yttrium aluminum perovskite, was studied by transmission EXAFS spectroscopy at the absorption edges of both the elements occupying the same crystal site. These results, paired with the ones obtained by analogous measurements on pure yttrium and lutetium aluminum perovskites, were the key factor to observe structural variations induced on the lutetium aluminum perovskite. Such variations can be ascribed to a decrease of local crystal order caused by the formation of distorted cells around yttrium sites, highlighting an intermediate crystallographic order between LuAP and YAP. Local characteristics of the crystal such as the spatial distribution of yttrium over lutetium affect the volume of cells around yttrium atoms bringing on possible distortions in their structure as suggested by Raman spectroscopy.

On the other hand, the analysis of photoluminescence spectra of iron-doped yttrium aluminum garnet samples performed at low temperatures with excitation energies ranging from the band gap energy down to selective excitation of Fe^{3+} ions permitted to give an answer to a still open topic of research, as well as to get results on issues of general interest in the field of study of Zero Phonon Lines.

The results obtained at low temperatures by very different techniques such as EXAFS spectroscopy on the absorption edges of lutetium and yttrium in LuYAP and photoluminescence spectroscopy recorded with different excitation energies for Fe-YAG can be effectively put together for their usefulness as tools of structural analysis. Thanks to their capability of discerning specific structural features of doped materials, these techniques suggested new insights on two opposite cases of doping, namely a heavy yttrium doping (around 30%) and a very light one (few ppm).

However, the study of structural characteristics in actual compounds can be also conducted using a different point of view, capable of suggesting new possible industrial applications. This choice doesn't imply that structural analysis cannot lead to interesting and useful insights in basic research but, at the same time, that undesired features may play an important role in the device performance: thus their presence and their effects should be analyzed and, if possible, exploited rather than ignored or minimized. This approach takes advantage of features which are commonly seen as useless or detrimental of the performance of actual compounds and turn them into useful characteristics for new applications.

On the grounds of this concept three studies on different materials, were presented. The results of the comparative analysis between sol-gel and Czochralski grown LYSO crystals demonstrated that the former can be, in principle, considered an alternative to single crystals for applications like detection of ionizing radiations or for scintillating devices in the small X ray energy range. On top of that, photoluminescence spectra of sol-gel and Czochralski grown Ce-doped LYSO samples showed a significant “structural” variation: while in the Czochralski grown samples Ce^{3+} ions occupy preferentially only one of the two possible crystallographic sites, in the sol-gel grown samples cerium doping occurs in both the allowed sites.

The study of externally induced crystal-to-amorphous phase conversion in TiO_2 nanoparticles demonstrated an interesting characteristics that, given the number of applications of this compound,

could be exploited in many different fields. In particular, the anatase-to-amorphous phase conversion of TiO_2 nanoparticles can be finely controlled by a proper choice of the incident radiation power density and of the oxygen partial pressure in the experimental chamber, since the effect acting on the surface oxygen defects was found to be spatially narrow and temporally fast.

The possibility of inducing variations in a compound by controlling the atmosphere during the growing process was the focal point of the third study, which aimed at analyzing and controlling oxygen vacancies formed during the Czochralski growth of doped LuYAP single crystals. The presence of vacancies acting as electronic traps is commonly seen as a drawback in terms of scintillation performance but it can be also considered as a "tank" for electron storage, thus acting as a new starting point for the development of optical storage devices. Variations in the abundance of oxygen vacancies in differently-grown doped LuYAP single crystals were measured and the possibility of their tailoring for possible applications as optical storage devices was verified.

All in all, the results obtained by spectroscopic studies on different compounds showed the effective possibilities of conducting consistent researches for very diverse analytical purposes, ranging from fundamental structural analyses, either basic or more specifically application-oriented, hinting at new insights by remarking features of interest for the development of new devices.